THE MORPHOLOGY AND COULOMBIC EFFICIENCY OF LITHIUM METAL ANODES

A Dissertation
Presented to
The Academic Faculty

by

Johanna Karolina Stark Goodman

In Partial Fulfillment
of the Requirements for the Degree
Doctor in Philosophy in the
Chemical & Biomolecular Engineering

Georgia Institute of Technology

May, 2014

THE MORPHOLOGY AND COULOMBIC EFFICIENCY OF LITHIUM METAL ANODES

Approved by:

Dr. Paul A. Kohl, Advisor
School of Chemical and Biomolecular Engineering
Georgia Institute of Technology

Dr. Thomas F. Fuller
School of Chemical and Biomolecular Engineering
Georgia Institute of Technology

Dr. Pradeep K. Agrawal
School of Chemical and Biomolecular Engineering
Georgia Institute of Technology

Dr. J. Carson Meredith
School of Chemical and Biomolecular Engineering
Georgia Institute of Technology

Dr. Faisal Alamgir
School of Material Science and Engineering
Georgia Institute of Technology

Date Approved: 12/5/2013

In dedication to my loving husband and wonderful parents

ACKNOWLEDGEMENTS

I would like to first thank my advisor, Prof. Paul Kohl, for his advice and support during my time at Georgia Tech. When I first joined his group as an undergraduate research assistant, I found that I enjoyed doing research and it was this experience that inspired me to continue to graduate school. I would also like to thank Prof. Tom Fuller, Prof. Carsen Meredith, Prof. Pradeep Agrawal, and Prof. Faisal Alamgir for participating in my thesis committee and contributing to my work through helpful discussions.

I would like to give special thanks to current and past group members for making my time at Georgia Tech such a wonderful experience. I would like to thank Hyea Kim, Florencia Rusli, Vidhya Chakrapani and Zhongsheng Wen for sharing ideas and discussions, as well as glovebox space. In particular, thank you to Hyea for being my mentor during my undergraduate research and again during my graduate career. Thank you to Jared Schwartz and John Ahlfield for being great officemates, and Sarah Kim and Brennen Mueller for making ours' the cool side of the office.

Thank you to my parents for raising me to be the person I am today and cheering for me during graduate school and throughout my life. And finally, thank you to my husband David, for encouraging me to challenge myself, always being there to catch me when I stumble, and being the smile in my life.

TABLE OF CONTENTS

LIST OF TABLES

LIST OF FIGURES

LIST OF SYMBOLS AND ABBREVIATIONS

ρ	density (g/cm^3)
A	nucleation rate (nuclei/s)
C	coulomb
C_d	double layer capacitance
CV	cyclic voltammogram
CVD	chemical vapor deposition
DEC	diethyl carbonate
DMC	dimethyl carbonate
DSC	differential scanning calorimetry
EC	ethylene carbonate
EDL	electrical double layer
EDX	energy dispersive x-ray spectroscopy
EIS	electrochemical impedance spectroscopy
EMC	ethyl methyl carbonate
EMI-$AlCl_4$	ethyl-methyl-imidazolium chloroaluminate
F	Faraday's constant (96,485 C/mol)

FSI^-	bis(fluorosulfonyl)imide
i	current
ICP-ES	inductively coupled plasma emission spectroscopy
IL	ionic liquids
k	deposition rate (mol/(cm^{2}s))
$LiPF_6$	lithium hexafluorophosphate
M	molecular weight (g/mol)
MCMB	meso-carbon micro beads
n	equivalents per mol
N	number of nuclei at a given time
N_0	total number of nuclei
N_{1114}-TFSI	trimethylbutylammonium bis(triflouromethanesulfonyl)imide
NHE	natural hydrogen electrode
PVDF	poly vinylidene fluoride
R_Ω	electrolyte resistance
R_{ct}	charge transfer resistance
SBR	styrene-butadiene rubber

SEM	scanning electron microscope
SEI	solid electrolyte interface
SIMS	secondary ion mass spectroscopy
t	time (s)
TEM	transmission electron microscopy
$TFSI^-$	bis(trifluoromethansulfonyl)imide
ToF-SIMS	time of flight secondary ion mass spectroscopy
TGA	thermogravimetric analysis
UDP	under-potential deposition
VC	vinylene carbonate
Z_w	Warburg impedance

SUMMARY

The lithium-ion battery was first commercialized in 1990 by Sony. Lithium ion batteries provided a higher gravimetric and volumetric energy density than previously used nickel-metal hydride or nickel-cadmium batteries and thus quickly dominated as the battery of choice for mobile applications. Since the original lithium-ion battery was commercialized, the electrodes and electrolyte have remained fundamentally unchanged and energy density improvements have come from minimizing the battery's packaging, rather than from improvements to the active materials. Future improvements must come from re-thinking the electrodes themselves. Lithium metal anodes are being considered as the next generation high capacity anodes for lithium batteries. With a capacity over ten times higher than current graphite anodes, such a shift has the potentially to significantly increase the overall energy density of a cell. There are two main issues facing the implementation of lithium metal anodes: 1) dendrite growth and 2) reactivity between lithium and the electrolyte.

When lithium metal is electrodeposited from an electrolyte, as it would be during battery charging, the deposited metal forms sharp needles, called dendrites. These dendrites are a significant safety concern because they can grow across the separator, potentially short circuiting the battery and causing thermal runaway. In this work, lithium was co-deposited with sodium to yield a non-dendritic deposited. This was accomplished by selecting two ionic liquids that could reduce and re-oxidize both lithium and sodium individually. Be selecting potentials at which both metals deposited, sodium physically blocked the dendritic sites inherent in lithium metal.

A nucleation study was conducted to observe the electrodeposits at short times. It was found that the organic electrolyte composed of ethylene carbonate and dimethyl carbonate initially produced a granular deposit that eventually lead to extruded dendrites. The ionic liquid electrolyte produced dendrites immediately upon nucleation. Additionally, the number of active growing dendrites decreased over time leading to two size distributions. This is due to the competition between surface film formation and continued growth on freshly deposited lithium metal. Co-depositing lithium with sodium resulted in a granular deposit immediately upon nucleation, indicating that the co-deposit is not a retroactive solution to dendrite growth. The local deposition rate k, proportional to the local current density, was solved for by taking into account the geometry of dendritic and non-dendritic growth. The rate of formation of the SEI layer and its subsequent effects were evaluated based on the trends found from the calculated deposition rate.

In addition to sodium, other alkali earth metals were tested as potential co-deposits with lithium. A reduction and oxidation could not be achieved from ionic liquid for potassium, thus no co-deposit was possible. Redox reactions were observed with rubidium and cesium but at potentials more negative than lithium. The potential window of the ionic liquid electrolyte did not extend negative enough to fully support the reduction, thus a non-dendritic co-deposit was not possible. Alkaline earth metals were also tested for their effect on the lithium deposit morphology. None of these metals were expected to form co-deposits as the two-electron transfer required to form the metals does not occur in our electrolyte. While no co-deposit was formed, the alkaline earth metal changed lithium’s deposit morphology by adsorbing to the substrate surface. Cyclic voltammograms of lithium/alkaline earth electrolytes were characterized by higher over-potentials and lower overall current density. These mixed electrolytes produce

granular, non-dendritic lithium deposits without the co-deposition of the alkaline earth metals. This is likely due to hindered lithium transport to the surface, which mitigates the accelerated growth that leads to dendrites. Two methods for suppressing dendritic growth were demonstrated in this work: first, the co-deposition of lithium with another metal to physically block dendritic growth, and second, an adsorption that hinders the transport of lithium ions to the surface, thus preventing the fast growth that would normally result in dendrites.

The second hurdle for lithium metal anodes is the instability between the electrolyte and lithium metal. Lithiated graphite, the charged anode in lithium-ion batteries, also suffers from this problem but the electrolyte is chosen so that the reactant products form a stable solid electrolyte interface (SEI) that protects the anode from further reaction during subsequent cycling. In the lithium metal system, such a SEI layer is conceptually more difficult because of the large volume change associated with depositing and stripping all lithium metal on each cycle. Formation of a better SEI layer on lithium metal was attempted through the addition of organic additives. Vinylene carbonate greatly improved the coulombic efficiency of lithium metal plating and stripping. The effect of gases, such as oxygen, nitrogen and carbon dioxide, on the SEI layer was also investigated. It was found that the presence of nitrogen and oxygen improved the coulombic efficiency by facilitating a thinner SEI layer. Though improvements in the coulombic efficiency were observed through changes in the atmosphere and organic additives, these improvements did not lead to sufficient coulombic efficiencies for battery applications.

This work presents attempts at improving the lithium metal anode both by increasing the coulombic efficiency of the redox process and by eliminating dendrite growth. The coulombic efficiency improvements through the bubbling of gases and adding organic

additives resulted in thinner and more protective SEI layers but work remains to increase these values more. Dendritic growth, which makes the lithium anode too dangerous as an anode, was completely eliminated by two methods: 1) co-deposition and 2) adsorption of a foreign metal. Both methods could potentially be applied to different electrolytes, making them promising methods for preventing dendritic growth in future lithium metal anodes.

1. Project Motivation

As consumer mobile devices shrink in size, the volume and weight of the batteries that power them have become important limiting metrics. While transistors have continued to shrink in size, the capacity of lithium-ion batteries first commercialized by Sony in 1991 has only seen incremental improvements[5,6]. The graphite anode, with a capacity of 329 mAh/g and long stable cycling profile, made the lithium-ion battery a success. The solid electrolyte interface (SEI), a Li^+ permeable layer that protects the electrode from side reactions, successfully forms in a number of electrolytes and counteracts the detrimental reactions between the electrolyte and reactive lithiated graphite. Since its discovery and optimization, progress has stalled on moving to higher energy density electrodes. Improvements in energy density have come from making the thinning the separator and minimizing the packaging, not from improving the capacity of the individual electrodes.

The two most studied high capacity lithium anodes are the silicon and Li-metal anodes with capacities of 2011 mAh/g and 3861 mAh/g, respectively (see Appendix 1). In both cases, volume change is a major issue. Lithium and lithiated silicon react with the electrolyte in a way similar to lithiated graphite, thus an SEI layer is needed. Volume change in graphite is limited to 12% thus the SEI can remain on the surface of the electrode once formed[7,8]. In silicon, the volume change has been measured at 320%, thus the ability of the SEI to protect the lithiated silicon cycle to cycle is compromised[8,9]. For a Lithium metal anode, volume change is accompanied by high surface area dendrite growth. When lithium is electrodeposited, the metal does not form a smooth, compact coating. Rather, long needles (i.e. dendrites) populate the surface. This

morphology is problematic because it yields a reactive high surface area that is passivated repeatedly. In addition, dendrites can break off leading to loss of active material, or grow through the separator causing a short circuit and overheating. The primary objectives for realizing a lithium metal anode are thus to change the morphology of the deposited lithium metal to eliminate dendritic growth, and to sufficiently passivate the lithium metal to enable steady cycling.

2. Background

2.1 Lithium-ion batteries

The lithium-ion battery is the current commercial battery used in most portable electronic devices. It consists of a metal oxide cathode, organic or polymer electrolyte, and graphite anode as shown in Figure 2.1. The graphite anode stores lithium ions in the batteries' charged state, while the cathode is the sink for lithium ions removed from the anode during discharge. The electrolyte, usually soaked into a porous separator, provides an ion pathway between the two electrodes, forcing electrons to travel through the external circuit. The reactions in a lithium-ion battery can be captured by Equations 2.1 – 2.3, where Equation 2.1 represents the anode, Equation 2.2 represents the cathode, and Equation 2.3 represents the overall cell reaction.

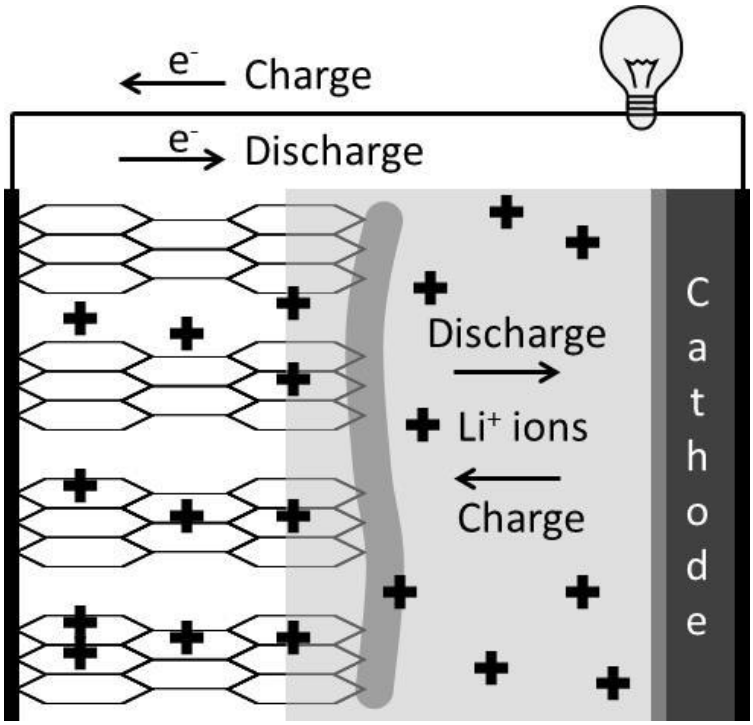

Figure 2.1: Cell schematic of a lithium-ion cell.

$$6C + Li^+ \leftrightarrow Li_xC_6 + (1-x)Li^+ \quad \text{Anode} \quad (2.1)$$

$$LiMO_2 \leftrightarrow Li_{(1-x)}MO_2 + xLi^+ \quad \text{Cathode} \quad (2.2)$$

$$6C + LiMO_2 \leftrightarrow Li_xC_6 + Li_{(1-x)}MO_2 \quad \text{Cell} \approx 3.7\ \text{V} \quad (2.3)$$

The baseline electrolyte used in most research is a 1:1 volume mixture of ethylene carbonate (EC) and dimethyl carbonate (DMC) whose structures are shown in Figure 2.2 and 2.3. To provide Li^+ conductivity, lithium hexafluorophosphate ($LiPF_6$) is added to make a 1M electrolyte. This organic electrolyte has a window large enough to accommodate the intercalation/de-intercalation of graphite and the metal oxide cathodes[10].

Graphite comes in several different forms: as natural and synthetic flakes, meso-carbon micro beads (MCMB), and graphite fibers[11]. A slurry of the graphite particles and binder, such as styrene-butadiene rubber (SBR) or poly (vinylidene fluoride) (PVDF), is cast on a copper current collector to fabricate the anode. When charged, lithium ions are stored between the graphite sheets, with one lithium ion being held on the top and bottom by a 6 carbon ring. This stoichiometry gives a capacity of 329 mAh/g. In practice, capacities of 310 mAh/g have been reached[12]. Lithium intercalation into graphite occurs at 0.05 V vs. Li/Li^+. Because of the graphite charging potential's proximity to lithium reduction, tight voltage control is required to keep lithium from depositing on the graphite surface.

Lithium cobalt oxide ($LiCoO_2$) is a commonly used cathode in lithium-ion batteries. Lithium is held in a layered structure, allowing for 2D diffusion of lithium ions in and out of the structure. Only half of the lithium can be electrochemically removed, yielding a capacity of 140 mAh/g[5,6]. A capacity of 130 mAh/g can be maintained for the life of the battery[13]. Lithium manganese oxide ($LiMnO_2$) alone shows a capacity of 105 mAh/g but by partially substituting manganese with chromium ($LiMn_{0.5}Cr_{0.5}O_2$) the capacity is improved to 190 mAh/g[14]. The Cr substitution prevents in situ transformation from a layered structure to a lower capacity spinel phase. Lithium iron phosphate ($LiFePO_4$) possess as capacity of 165 mAh/g and is thus also a serious candidate to replace lithium cobalt oxide[5].

Improvements to this battery as a whole have also come from the connections and packaging of the device, rather than from changes in the chemistry. Thinner and stronger separators, as well as thicker individual electrodes increase the specific capacity. Lighter and thinner metals used in the packaging of batteries also improved overall energy density. With the capacities of individual electrodes near their theoretical

maximums, the path to further improvements lies in changing the electrodes themselves, rather than improving the existing system.

2.2 Solid Electrolyte Interface (SEI) Layer

Pure lithium metal and lithiated graphite react with the electrolyte resulting in the consumption of active material and irreversible capacity loss. In solutions of linear carbonates and ethers, only modest amount of the intercalated lithium can be recovered on each cycle because of lithium active material is consumed or the graphite is exfoliated by intercalation of the solvent itself[15]. Lithium-ion batteries owe their performance to the solid electrolyte interface (SEI) layer, a Li^+ conducting layer formed by the decomposition of cyclic carbonates. During the charging cycle of a graphite anode, irreversible features can be observed at 0.5 - 1.0 V vs. Li/Li^+. These features are attributed to the passivation of the anode surface resulting in the SEI layer. This layer, if formed well, is permeable to lithium ions but protects the anode from further reaction with the electrolyte. Formation of this layer is critical because anode stability in the charged state represents long shelf life. The composition of this layer varies depending on the anode and electrolyte used but generally contains lithium alkoxides along with lithium fluoride (LiF), and lithium carbonate[16,17].

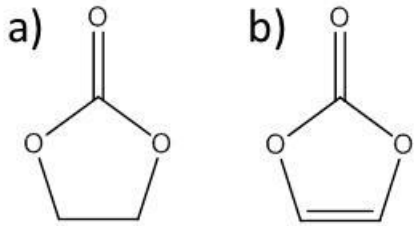

Figure 2.2: a) Ethylene carbonate (EC) and b) vinylene carbonate (VC) are a part of almost every electrolyte because their reduction products form an excellent protective SEI.

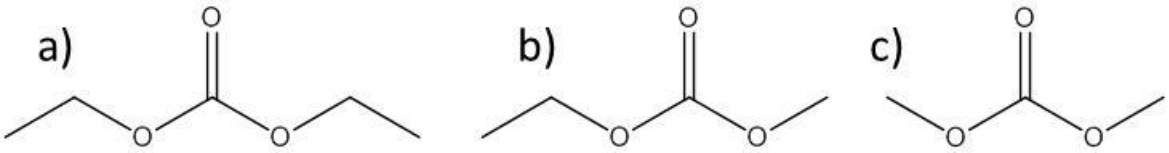

Figure 2.3: a) Diethyl carbonate (DEC), b) ethyl methyl carbonate (EMC), and c) dimethyl carbonate (DMC) are often used as co-solvents to make the organic electrolyte used in Li-ion batteries.

Ethylene carbonate (EC, Figure 2.2a) is a main solvent in the organic electrolyte because it is responsible for forming the SEI layer. This cyclic carbonate is solid at room temperature, and is thus used with a co-solvent with linear carbonate such as diethyl carbonate (DEC), ethyl methyl carbonate (EMC), or dimethyl carbonate (DMC) shown in Figure 2.3. Following a ring-opening reaction at 0.9 V vs. Li/Li^+, EC decomposes to form several high molecular weight surface species as shown in Equations 2.4 and 2.5. These provide a protective surface film and halts electrode/electrolyte side reactions[12,15,18–22]. Once this film is formed, the graphite anode can continue to operate for 1000s of cycles. In electrochemical studies, a feature around 0.9 V vs. Li/Li^+ can be identified as the reduction of ethylene carbonate. This feature appears prominently in the first cycle but disappears in subsequent cycles resulting in the high reversibility of the graphite anode.

$$2\,EC + 2\,e^- + 2\,Li^+ \rightarrow LiCH_2CH_2OCO_2Li \quad (2.4)$$

$$2\,EC + 2\,e^- + 2\,Li^+ \rightarrow (CH_2OCO_2Li)_2 + C_2H_4 \quad (2.5)$$

While EC is by far the most utilized SEI forming additive, vinylene carbonate (VC, Figure 2b) has been shown to have similar effects[23,24]. Vinylene carbonate results in a lower irreversible capacity in graphite on the first cycle, even when used in conjunction with EC. Vinylene carbonate can react in a similar manner as EC, as shown in Equations 2.6 and 2.7. It is also suspected that VC forms oligomeric and polymeric species, which are not triggered by the electrochemical intercalation, and thus do not factor into the irreversible capacity loss[23,24].

$$2\,VC + 2\,e^- + 2\,Li^+ \rightarrow LiO_2COC = COCO_2Li + C_2H_2 \quad (2.6)$$

$$2\,VC + 2\,e^- + 2\,Li^+ \rightarrow LiO_2C = C - C = CO_2Li + 2\,CO \quad (2.7)$$

Many reactions that occur on lithiated graphite, also occur on lithium, including the reduction of ethylene carbonate and vinylene carbonate into their surface species[18,25]. Despite similar surface species, lithium metal anodes cycle poorly compared to their graphite counterparts. This is likely due to the volume change associated with depositing and stripping lithium metal. In the graphite case, the SEI forms and continues to adhere to the graphite, being reused on each cycle. In the lithium metal anode case, the SEI

must be stretched during the charging cycle to accommodate the additional lithium. During the discharge cycle, lithium is re-oxidized and the SEI is left with nothing to adhere to. The issue of volume change complicates the notion of an SEI in lithium metal batteries.

2.2 Lithium Metal Anodes and Dendrite Growth

The graphite anode uses six carbons to store a single lithium atom. To improve the energy density of the lithium battery, lithium could be stored in its metallic form without any supporting structure. This potential lithium metal anode has a specific capacity of 3861 mAh/g, significantly higher than the 329 mAh/g afforded by the graphite anode. Lithium would be electrodeposited on a substrate during the charging process, and stripped away during discharge as shown in Figure 2.4 and Equation 2.8. This anode half reaction takes place at -3.04 V vs. NHE, just 0.05 V negative of lithium intercalation into graphite.

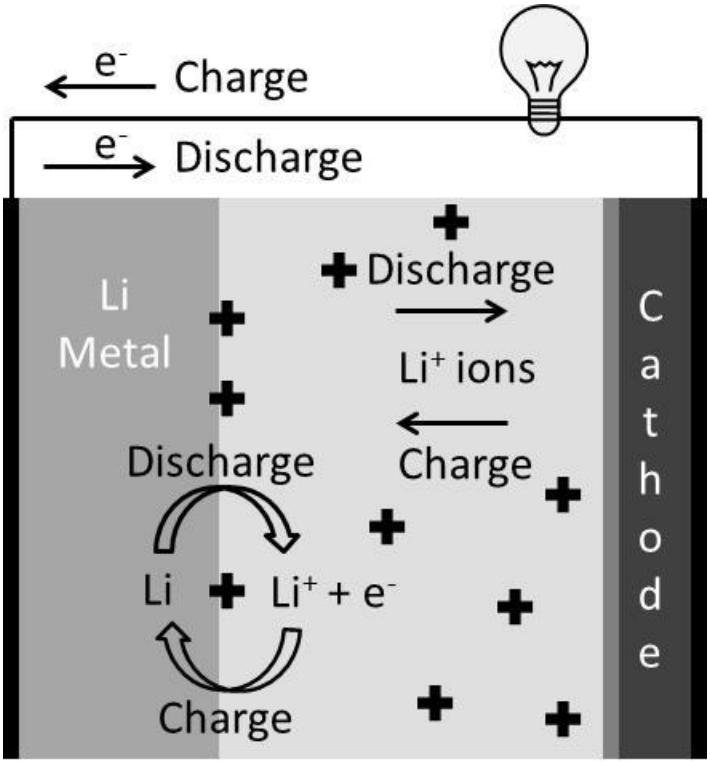

Figure 2.4: Schematic of a Li-metal anode battery.

$$Li \leftrightarrow Li^{+} + e^{-} \qquad \text{-3.04 V vs. NHE} \qquad (2.8)$$

Charging of the lithium metal anode is achieved by electrodepositing lithium metal on a substrate. Electrodeposition of lithium metal does not yield a smooth surface, rather lithium metal forms long whisker-like structures known as dendrites that have been observed by multiple groups both in-situ and ex-situ[26–31]. Figure 2.5 shows examples of several dendritic morphologies from a variety of electrolytes. Dendrite appearance varies depending on current density and electrolyte used but their formation occurs in almost every electrolyte, hinting that this is a property of lithium metal itself, rather than an effect of the electrolyte.

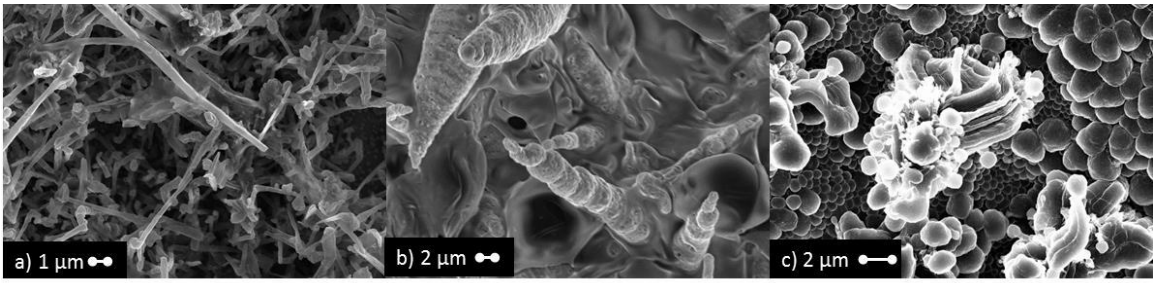

Figure 2.5: SEM images of dendrites from several different electrolytes

These structures present a hazard to battery operation because they can grow through the separator and short-circuit the battery. This not only destroys the battery but can overheat the battery due to rapid discharge, leading to vaporization of the electrolyte. The high surface area of dendrites is problematic because lithium batteries operate on the principle that an SEI can be formed to protect the surface, and can be re-used on subsequent cycles. Passivating the dendrite surface requires too much charge and active material, and the SEI is lost on each cycle as lithium is stripped away. Lastly, dendrites suffer from poor adhesion to the substrate, thus lithium active material can be lost to delamination. If the lithium dendrite is oxidized at the base before the tip, the lithium metal in the dendrite is lost, leading to further inefficiencies.

Dendrites are observed with several different characteristics: constant diameter (Figure 2.5a), cone shaped (Figure 2.5b), and bulb headed (Figure 2.5c). Given that the entire dendrite surface is in contact with the electrolyte, the electrochemical growth rate at the tip of the dendrite must be significantly higher than on the sidewalls. We hypothesize that dendrite growth is caused by an accelerated growth on a certain crystallographic face. In the case of the constant diameter dendrites (Figure 2.5a) this facet is at the flat tip. The screw-like dendrites shown in Figure 3b can also be explained by crystallographic growth via a dislocation at the center. Dendrites themselves have

been identified as single lithium crystals by two groups using in situ transmission electron microscopy (TEM) techniques[32,33]. No ex-situ studies have observed the crystallinity of dendrites.

An additional mode of dendrite growth, by extrusion or base growth, has been experimentally observed[34,35]. In this case, the dendrite is not formed by material electrodepositing on the tip, but by material being extruded from the bulk deposit. Yamaki et al. predict a bulbous shape to arise from the unbalance between creep strength and surface tension[34]. This morphology was observed and is shown in Figure 2.5c. Tin is also known to form dendrites by this extrusion mechanism as shown by Howard et al.[1], where whiskers are formed by metal migrating along the substrate-metal interface and grain boundaries. For tin, electroplating causes compressive stresses that are relieved through whisker extrusion. In lithium, this compressive stress could be built up under the SEI layer with similar results.

Lithium dendrite suppression has been achieved by physically confining the lithium metal behind a solid electrolyte[36], however, the large volume change associated with cycling a lithium metal battery could make the solid-state approach problematic as materials could crack or delaminate. Heavily fluorinated electrolytes[37–39] and the LiAsF6/dioxolane electrolyte[40,41] have also lead to non-dendritic lithium deposits. A study in organic propylene carbonate/dimethyl carbonate (PC/DMC) showed non-dendritic lithium deposition by addition of rubidium and cesium hexafluorophosphate to the electrolyte[42]. This was explained by an electrostatic shield mechanism where the adsorbed rubidium or cesium ions on the dendrite repel the lithium ions from the region of the dendrite. A low concentration of rubidium or cesium ions was required so that the deposition potential for rubidium or cesium was shifted to values negative of the lithium

deposition potential. The method does not allow for non-dendritic plating above a certain current/potential where cesium or rubidium reduce, thus limiting the charging current.

The SEI on a lithium metal anode is more difficult to form and maintain than the SEI on a graphite anode. On graphite, the SEI can adhere to the graphite structure and protect the pathways to the planes between carbon layers. A lithium metal anode presents a more dynamic surface that changes upon each cycle. The uneven electroplating of lithium metal calls into question the possibility of a reusable SEI. Many studies exist to document the surface species on lithium metal in contact with various solvents and salts, but simply generating a certain species on the surface does not necessarily lead to a good SEI and stable cycling. The layer must prevent further reaction with the electrolyte and maintain the same thickness through many cycles. Electrolyte species that react to form soluble or porous products with lithium are thus not suitable for lithium metal batteries.

2.3 Whisker Growth in Other Systems

Lithium is a difficult system to study because of the air-sensitive nature of the metal. Meaningful mechanistic work on the crystallinity and mode of dendrite growth has only been done with in-situ techniques. These techniques require much preparation and instrumental expertise, thus it is useful to gain insight from other well established systems.

Tin-lead alloys are used in microelectronic applications rather than elemental tin to prevent the spontaneous formation of dendrites. Safety concerns exist with pure tin metal because it will spontaneously form whiskers up to millimeters in length, long enough to bridge gaps between different components. It has been determined that tin

whiskers form to relieve compressive stress in the metal, thus studies on this particular whisker growth center around preparing a tin coating, applying a known compressive stress, and observing the resulting whisker growth. Howard et al. conducted one such experiment where tin was electroplated on a stainless steel substrate and clamped at 0 - 12 MPa pressures[1]. Subsequent observation and cross-sectioning revealed that whiskers originated from the substrate/tin interface and were extruded out through the bulk tin (Figure 2.6a and 2.6b. Metal in the whisker likely diffused along the interface and long the grain boundaries. For a given pressure, the number of whiskers leveled off over time, indicating that the whisker growth halts when the compressive stress is relieved[1].

Silver also forms dendrites when electrodeposited but unlike tin, these are formed directly from deposition, not from the release of compressive stress. Silver dendrites display multiple branches as shown in Figure 2.6c. Silver and copper deposit at similar potentials from ammonia solutions, and thus can be co-deposited electrochemically[43]. The ratio of silver and copper ions in solutions can be used to tailor the composition of the co-deposit. A non-dendritic, granular morphology can be achieved with a silver content below a certain level. A second method that mitigates silver dendrites from silver/copper solutions is the addition of aminopolycarboxylate ligands (EDTA and HEDTA) which can form complexes with silver and copper ions, as well as adsorb on the substrate surface. The addition of such ligands inhibits silver reduction and thus lowers the silver content of the electrodeposit, resulting a granular, non-dendritic deposit[43].

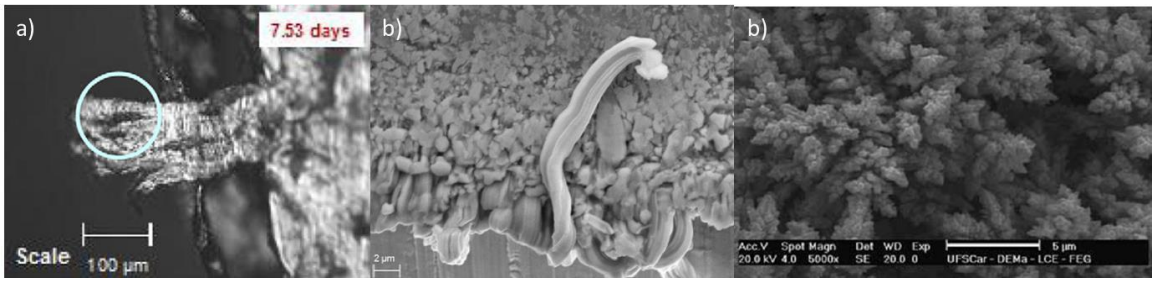

Figure 2.6: Tin whisker observed (a) in situ after 7.53 days under 12 MPa (b) and ex situ in an SEM[1]. Highly branched silver dendrites resulting from electrodeposition (c).

Dislocation based growth has been observed in potassium and lead sulfide (PbS) nanowires synthesized via chemical vapor deposition (CVD). PbS nanowires can be grown using a CVD with $PbCl_2$ and sulfur as precursors. The resulting christmas tree-like structures have a constant diameter trunk and perpendicular branches as in Figure 2.7. Bierman et al. conducted TEM and growth rate analysis showed significantly higher growth rate on the trunk than the branches. This was attributed to a dislocation found at the center of the trunk. Bierman et al. proposed that this central dislocation resulted in accelerated growth at the tip of the nanowire. In order to fully explain the significantly faster growth rate, material had to not only come from the vapor phase, but also from surface diffusion along the length of the trunk. That is, material would adsorb on the sides of the trunk and diffuse along it until reached a suitable place to join the lattice at the tip dislocation[2,3].

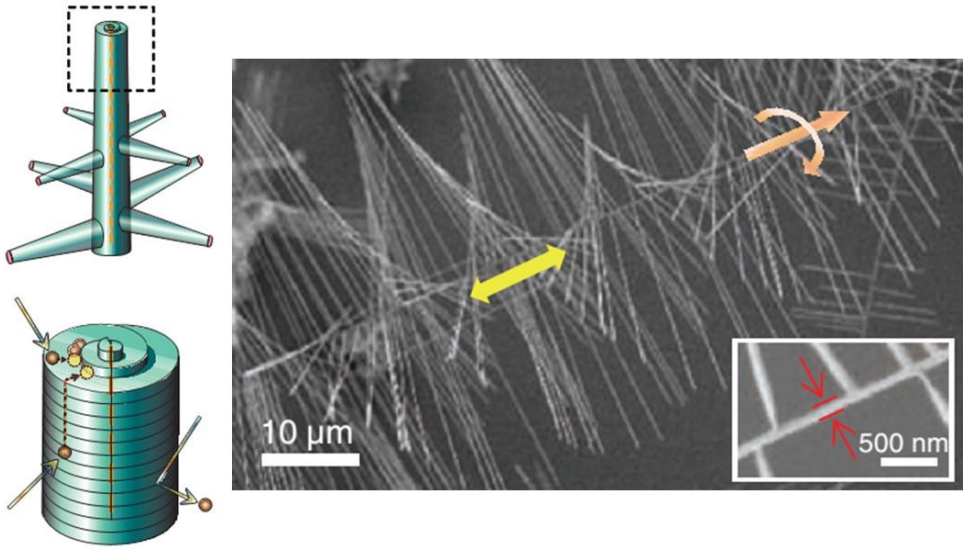

Figure 2.7: Schematic and SEM image of PbS nanowire trees grown by CVD. The dislocation at the center, as well as diffusion along the length of the wire results in constant diameter nanowires[2,3].

A similar mechanism was proposed by Dittmar et al. for the growth of single crystal potassium whiskers condensed from super supersaturated potassium steam[44]. The whisker length increased too quickly for direct condensation at the tip only, thus adsorption and subsequent diffusion was proposed to explain the accelerated growth. The diffusion coefficient along the length of the whisker necessary to account for the tip growth was calculated[45–47].

The two mechanisms observed for needle-like growth are extrusion, as in tin, and crystallographic dislocation driven growth, as in PbS and potassium. In these cases, the whiskers were identified as crystalline, suggesting that such a driving force is necessary for the directional growth observed.

2.3 Ionic Liquids as Electrolytes

The organic electrolyte used in lithium ion batteries is responsible for the swelling and/or ignition in the case of battery failure. Its flammability adds to the hazard during a short circuit or overheating event. Ionic liquids (IL) are presented as next generation electrolytes that circumvent these safety hazards. Room temperature ionic liquids are salts with melting points below ambient temperature. These liquids have no vapor pressure, ensuring that they will not swell the battery or form vapors should the battery fail. Thermogravimetric analysis (TGA) and differential scanning calorimetry (DSC) shows thermal stability of IL's to be 350-450°C, but UV/vis spectra show structural changes as low as 150°C that may limit high-temperature operation[48,49]. Ionic liquids are not flammable adding an additional layer of safety in case of a battery malfunction[50].

Room temperature ILs typically consist of an asymmetric organic cation and an inorganic anion. Figure 2.8 shows several examples of possible cations such as pyrrolidinium, piperdinium, imidazolium, and aliphatic quaternary ammonium. Lower melting points, which result in lower viscosity and higher conductivity, are achieved by picking cations with asymmetric side-chains[51]. While there is some synergistic effect between cation and anion, the cation choice largely determines the anodic stability of the IL, which is a primary concern when considering an electrolyte for a lithium metal battery. Generally, imidazolium ILs are only stable to -1.7 V vs. NHE[49,52,53], making them questionable as electrolytes for lithium batteries, which operate at -3.04 V vs. NHE. The remaining cations shown in Figure 2.8 show anodic stability negative of -3.0 V, making them candidates for lithium battery electrolytes.

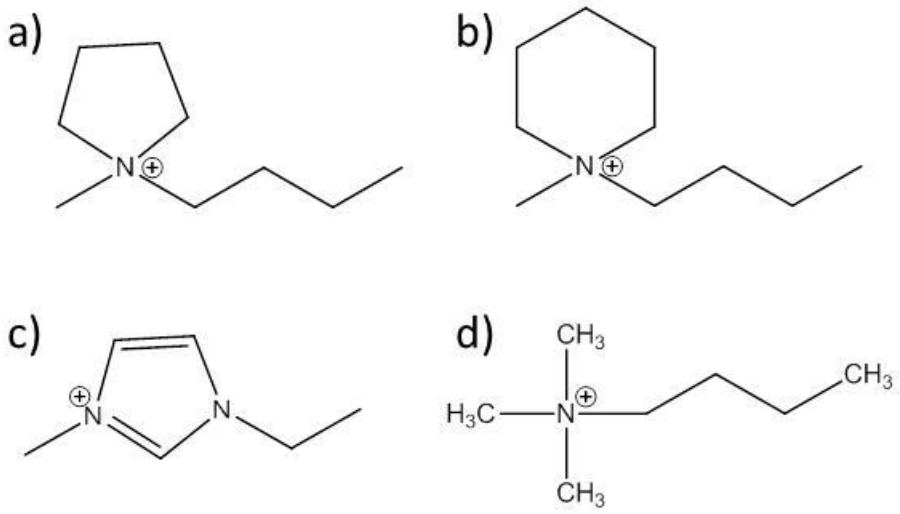

Figure 2.8: Examples of possible anions for room temperature ionic liquids: a) pyrrolidinium, b) piperdinium, c) imidazolium, and d) aliphatic quaternary ammonium (used in this work).

The inorganic anion determines the cathodic stability of the IL and, in the case of lithium electrolytes, is often fluorinated to promote hydrophobicity and SEI formation. Anions such as chloroaluminate ($AlCl_4^-$), hexafluorophosphate (PF_6^-), tetrafluoroborate (BF_4^-), bis(fluorosulfonyl)imide (FSI^-) and bis(trifluoromethansulfonyl)imide ($TFSI^-$) have been tested for battery applications and are shown in Figure 2.9.

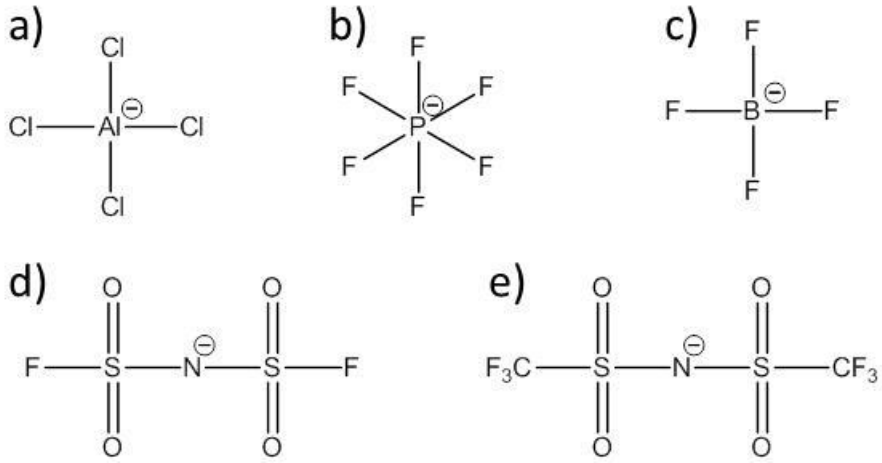

Figure 2.9: Examples of possible anions for room temperature ionic liquids: a) chloroaluminate ($AlCl_4^-$), b) hexafluorophosphate (PF_6^-), c) tetrafluoroborate (BF_4^-), d) bis(fluorosulfonyl)imide (FSI^-), and e) bis(trifluoromethansulfonyl)imide (used in this work).

Ionic liquid electrolytes have been tested with commercial graphite anodes with some success, however a robust SEI layer required for the graphite does not form with ionic liquid only. A cyclic voltammograms (CV) of graphite in neat ionic liquid shows that the cation itself intercalates into the graphite structure, reducing capacity available for lithium ion storage[54]. This can be mitigated by adding organic SEI forming additives that are responsible for stabilizing lithiated graphite in traditional organic electrolytes, such as EC or VC. This mimics the SEI in organic electrolytes and can lead to stable cycling. By minimizing the amount of organic additive the non-flammable properties of the IL can be maintained[54,55]. The FSI^- anion has shown compatibility with graphite anodes without addition of organic additives[56,57]. A comparison of the SEI layer formed with FSI^- and $TFSI^-$ has not been done but based on impedance data, Ishikawa et al. believe the double layer formed by FSI^- results in Li^+ directly on the surface rather than the IL cation. This is possible because FSI^- does not bind Li^+ as strongly as $TFSI^-$. The greater freedom of Li^+ results in less cation decomposition upon cycling[58].

3. Materials and Experimental Methods

Metallic lithium is sensitive to oxygen and moisture, easily forming lithium oxide (Li_2O) and lithium hydroxide (LiOH). Under a nitrogen atmosphere, lithium can also form lithium nitride (Li_3N) making a well-controlled atmosphere imperative. All work was conducted in a Vacuum Atmospheres glovebox under argon. A dew point meter in the glovebox continually measured the water content, which was maintained at less than 0.04 ppm. This extremely dry atmosphere allowed for the preparation and operation of open lithium metal cells

3.1 Organic Solvents, Ionic Liquids, and Salts

Three different electrolytes were used in the course of this study: (1) the traditional organic EC:DMC electrolyte, (2) an imidazolium chloroaluminate Ionic liquid, and (3) an aliphatic ammonium TFSI ionic liquid.

The traditional organic electrolyte was mixed from a 1:1 volume ratio of ethylene carbonate (EC, anhydrous, 99%, Sigma-Aldrich) and dimethyl carbonate (DMC, anhydrous, ≥99%, Sigma-Aldrich) without further purification. Lithium hexafluorophosphate (≥99.99%, Aldrich) was added to make a 1 M Li^+ electrolyte.

The imidazolium chloroaluminate ionic liquid was synthesized from ethyl-methyl-imidazolium chloride (EMI^+Cl^-, 97%, Acros) and aluminum chloride ($AlCl_3$, anhydrous, Fluka). Ethyl-methyl-imidazolium chloroaluminate (EMI-$AlCl_4$) was synthesized by buffering an acidic melt of EMI^+Cl^- and $AlCl_3$ with either lithium chloride (99%, Baker) or sodium chloride depending on the desired electrolyte.

$$EMI^+Cl^- + AlCl_{3(excess)} \rightarrow EMI^+ + AlCl_4^- \quad (3.1)$$

$$AlCl_4^- + AlCl_3 \rightarrow Al_2Cl_7^- \quad (3.2)$$

$$Al_2Cl_7^- + MCl \rightarrow M^+ + 2AlCl_4^- \quad (3.3)$$

The initial melt was made by slowly mixing the EMI^+Cl^- and $AlCl_3$ in a 55:45 molar ratio until only a clear liquid remained (Equations 3.1, 3.2). This liquid was dried under vacuum for 8 h before adding 100% excess of the metal chloride to ensure a completely buffered melt (Equation 3.3). In order for this melt to plate and re-dissolve lithium and sodium, ~0.5 wt% of $SOCl_2$ was added to each melt to facilitate metal ion reduction[51,59–61].

The ionic liquid used as a basis for the $TFSI^-$ electrolytes was trimethylbutylammonium bis(triflouromethanesulfonyl)imide (N_{1114}-TFSI, 99%, Iolitec). Salts with the matching $TFSI^-$ anion were purchased of synthesized according to Equation 3.4-3.5. Lithium bis(trifluoromethanesulfonyl)imide (Li-TFSI) was purchased from Wako. Barium bis(trifluoromethanesulfonyl)imide (Ba-$TFSI_2$), magnesium bis(trifluoromethanesulfonyl)imide (Mg-$TFSI_2$), and calcium bis(trifluoromethanesulfonyl)imide (Ca-$TFSI_2$) were purchased from Sigma Aldrich. The sodium, potassium, rubidium, and cesium salts were synthesized by reaction of the metal hydroxide with a stoichiometric amount of trifluoromethanesulfonimide (H-TFSI, Wako) and then adjusting to neutral pH (Equation 3.4). The solution was gently heated to remove water and then dried under vacuum for 12 h. Strontium bis(trifluoromethanesulfonyl)imide (Sr-$TFSI_2$) was synthesized in a similar manner, Equation 3.5.

$$MOH + HTFSI \rightarrow MTFSI + H_2O \quad (3.4)$$

$$M(OH)_2 + 2\,HTFSI \rightarrow MTFSI_2 + 2\,H_2O \quad (3.5)$$

Electrolytes were made by dissolving the appropriate amount of metal-TFSI salt in N_{1114}-TFSI ionic liquid.

3.2 Instrumentation and Experimental Set-up

A three electrode cell was used to conduct electrochemical experiments in the imidazolium chloroaluminate ionic liquid. The working electrode was a 0.5 mm diameter tungsten wire and the counter electrode was a 1 mm diameter tungsten wire. Both were encased in borosilicate glass and polished before each use. The reference electrode was an aluminum wire (Fluka) immersed in a 40:60 mol ratio EMI^+Cl^-:$AlCl_3$ melt in a fritted glass tube. The electrochemical couple is between the acidic chloroaluminate species and the metallic aluminum, as described by Equation 3.6.

$$4\,Al_2Cl_7^- + 3e^- \leftrightarrow Al + 7AlCl_4^- \qquad E=0.0\ V \quad (3.6)$$

A simplified two-electrode cell was used to carry out experiments in the organic electrolyte and N_{1114}-TFSI ionic liquid electrolyte. The chloroaluminate reference electrode described in Equation 3.6 was not compatible with the organic electrolyte or TFSI-based ionic liquid, thus a piece of lithium foil was used as both the counter and

reference electrode in these systems. Stainless steel type 316 foil was used as a working electrode.

A Perkin Elmer Parstat 2263 with PowerSuite software was used to carry out most simple electrochemical experiments such a chronopotentiometry and chronoampeometry. Cyclic voltammograms (CV) were conducted with the appropriate set up at a potential scan rate of 0.01 V/s. Longer cycling experiments were performed on an Arbin Instruments BT-2000 battery tester by programming the appropriate charge and discharge currents with the MITS Pro software, which supports normal potentiostat/galvanostat methods as well as more detailed cycling regimes.

A Zeiss Ultra 60 scanning electron microscope (SEM) was used for imaging samples. SEM samples were prepared in the two- or three-electrode cells as required, and subsequently washed with anhydrous DMC to remove the viscous ionic liquid. This step was necessary because the ionic liquid does not evaporate and would obscure the sample if not removed. This same procedure was followed when using organic electrolyte to maintain consistency and prevent salts and EC from crystalizing on the sample as DMC evaporates. Samples were mounted on the chuck in the glovebox, and the chuck was subsequently transferred in an air-tight container to the instrument, where it was loaded quickly. An operating voltage of 5 eV and 20 µm aperture were used to observe samples. Elemental analysis was done with energy dispersive x-ray spectroscopy (EDX) using Oxford Instruments X-Sight column and INCA software. An operating potential of 8-10 eV and 60 µm apertures were used to generate element maps and sample compositions. EDX can identify elements as light as carbon, so lithium could not be directly observed by EDX. In addition, the intense bombardment often melted lithium samples under the beam, complicating some analyses.

A second method used to analyze the elemental composition of a sample was time of flight secondary ion mass spectroscopy (ToF-SIMS, SIMS). Samples were prepared as for SEM or EDX and mounted onto the stage in the glovebox. The stage was transferred to the instrument in an air tight container and quickly transferred to the instrument. Samples were analyzed in an ION-TOF5 SIMS using Bi^+ as the primary ion. Depth profiling was done by sputtering the samples using 500 keV Cs^+ over a 500 x 500 µm area. The analysis area was 150 x 150 µm within the larger sputtered area. SIMS works by pulsing Bi^+ at the sample surface. The heavy Bi^+ ions knock atoms loose from the sample surface and ionize some of them. These secondary ions are then analyzed and a spectrum is recorded. Depending on the frequency of the ion bursts and analysis, the instrument can be run in burst mode (prioritize elemental information) or bunch mode (prioritize spatial information). In burst mode, the high mass resolution means that peaks in close proximity can be distinguished. For example, around mass 14, Li_2^+ (13.882), N^+ (14.0067), and CH_2^+ (14.0269), can all be clearly distinguished in burst mode, Figure 3.1. Burst mode does not provide very good spatial resolution, so bunch mode is used for imaging. Features as small as 1 µm can be observed, however, mass resolution is significantly reduced. Ions at similar atomic mass can no longer be distinguished, which can complicate generation of an ion image if the desired peaks are close to each other.

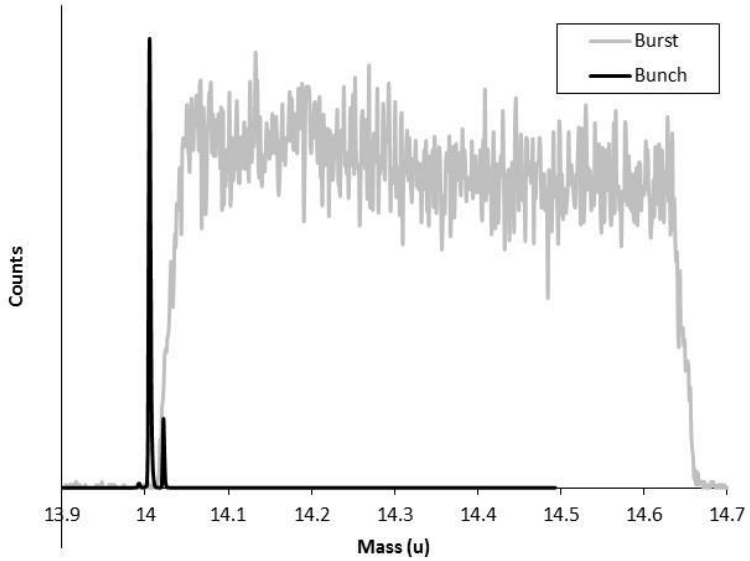

Figure 3.1: Count profile Comparison between SIMS burst and bunch modes. Peaks observed are Li_2^+ (13.882), N^+ (14.0067), and CH_2^+ (14.0269).

3.3 Cycling Methods and Coulombic Efficiency Calculations

The coulombic efficiency of a redox process can be determined by several different experiments. Because of the parasitic reactions that occur to form the SEI in lithium batteries, each experiment gives a slightly different coulombic efficiency and it is important to understand how to interpret this number. In this work, the coulombic efficiency is calculated from CV, full cycles, and shallow cycles.

Cyclic voltammetry scans a potential range and reverses the scan at a given switching potential while recording the current. Current peaks at given potentials indicate an electrochemical process. A process can be identified as reversible if a matching peak centered around a specific potential in opposite sign currents are identified, such as the reduction and re-oxidation of lithium. By integrating under the reduction and re-oxidation peaks, the charge passed for each process in coulombs (C) can be calculated. A

coulombic efficiency can then be determined by dividing the charge associated with the re-oxidation by the charge associated with reduction (Figure 3.2). When looking at the anode reaction of a lithium battery, a single first cycle will include not only battery charging (lithium intercalation or lithium plating) and discharging (lithium de-intercalation or lithium stripping) but also the formation of the SEI layer and other one-time surface modification. This results in the calculation of a lower coulombic efficiency than what would be expected from an actual battery.

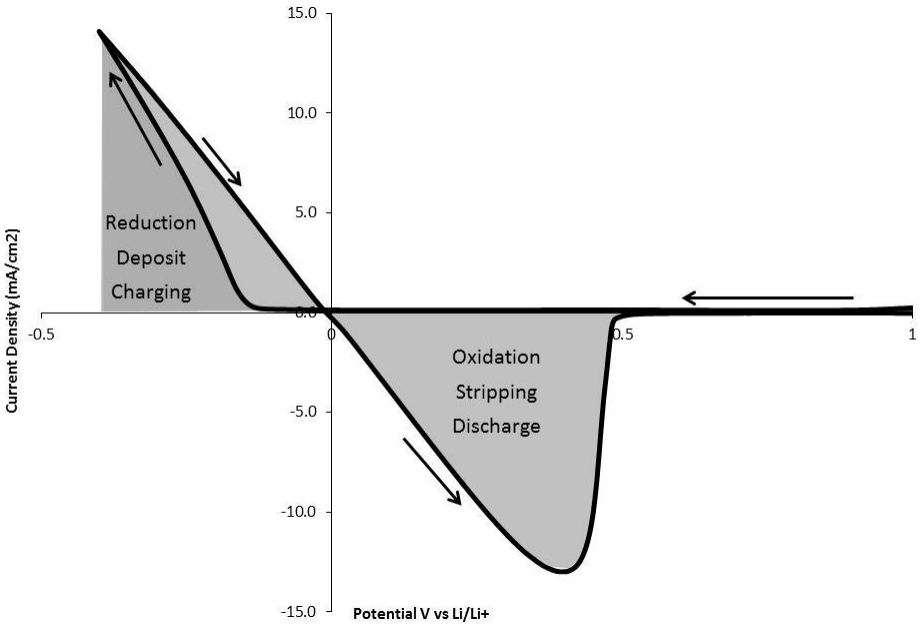

Figure 3.2: Schematic of a typical CV of a lithium electrolyte demonstrating the coulombic efficiency calculation.

Another method used to calculate the efficiency is by full charge and discharge. This method applies a constant current to the cell for a given amount of time to simulate the charging cycle. The current is then reversed and applied until a certain cut-off potential is reached. The process is repeated as many times as desired, as shown in Figure 3.3. The total charge passed during each cycle can be calculated along with an efficiency for

that cycle. This is the most common method used to characterize cycling and coulombic efficiency behavior. Lithium-ion batteries tested with this regimen begin with several low efficiency cycles that are representative of SEI formation on the graphite anode, before going into steady cycling. For a lithium metal anode, this type of full charge/discharge is not ideal because it involves stripping away all deposited lithium, leaving behind only the substrate and SEI layer. The formed SEI layer thus has nothing left to adhere to and is lost upon each cycle, lowering the coulombic efficiency recorded.

To maintain an SEI layer from cycle to cycle, a shallow cycling regime can be employed. In this regime, an excess of lithium is reduced on a substrate, but only a small amount of it is subsequently cycled. Because the coulombic efficiency of each cycle is not 100% the excess lithium will slowly be consumed and an overall coulombic efficiency can be calculated. First, excess metal (1 C/cm^2) was deposited on the stainless steel at 0.1 mA/cm^2. Then, 10% of the initial lithium capacity was cycled at 0.1 mA/cm^2 on each cycle until the lithium was exhausted during the oxidation part of the cycle. That is, 0.1 C/cm^2 of lithium was deposited and then 0.1 C/cm^2 of lithium was oxidized during each cycle. The potential was recorded during the constant current reduction and oxidation portions of the cycle, as shown in Figure 3.3. When there was no longer adequate lithium metal for the oxidation step, the potential rose sharply and the experiment is terminated. The number of cycles was recorded and the total charge for deposition and oxidation was used to give an average coulombic efficiency for the lithium deposition and stripping process. Thus, the SEI can adhere to a familiar surface and be maintained from cycle to cycle, resulting in the highest coulombic efficiency calculated. Given that a full battery would operate with excess lithium, this is also the most accurate cycling regime to ascertain real life performance.

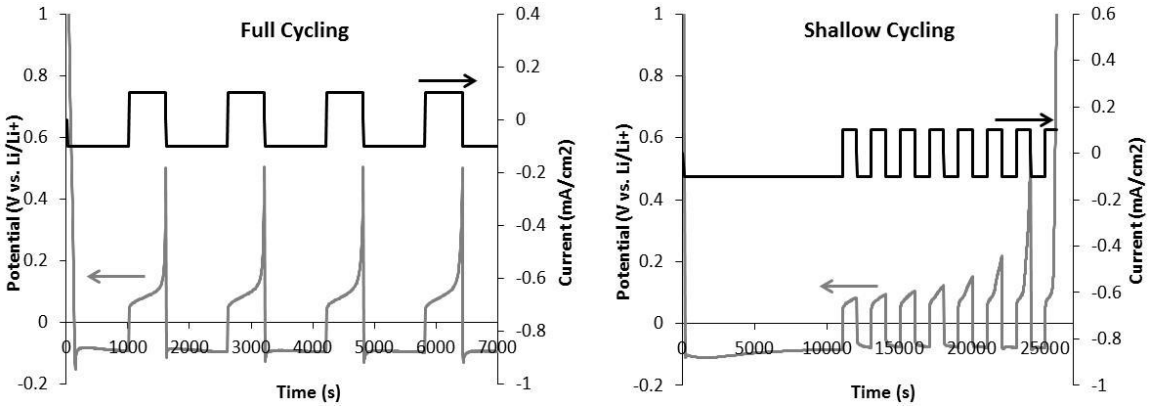

Figure 3.3: Schematic demonstrating full (left) and shallow (right) cycling. Full Cycling allows for a coulombic efficiency to be calculated each cycle while shallow cycling can only give an overall efficiency.

4. Dendrite-Free Electrodeposition and Re-oxidation of Li/Na Co-deposit

4.1 Objective

In this chapter, the effect of co-depositing lithium metal with a small amount of sodium in order to suppress dendritic growth was investigated. Figure 3.1a-b shows dendrites that appear to have a crystalline character and accelerated growth rate in specific areas. By co-depositing lithium with another alkali metal, that rate could be altered and dendritic growth could be prevented. Specifically co-deposition could physically block these high growth rate sites leading to a smaller deposit rate. In a similar case, silver can be co-deposited with copper to form a granular deposit. By carefully controlling the silver content and current density, a non-dendritic metal deposit with excellent conductivity can be achieved[43].

Such a co-deposit requires that the both metals be deposited from the same electrolyte and that they have redox potentials close to each other so that co-deposition can occur. Sodium was chosen because its reduction potential is -2.714 V vs. NHE compared to lithium, which is -3.04 V vs. NHE. Sodium is difficult to deposit electrochemically and cannot be deposited from the EC/DMC organic electrolyte. Ionic liquids however, have been shown to suitable for sodium deposition[60,62]. Lithium deposition experiments have been carried out in ionic liquid electrolytes[54,60,63,64], however, the electrochemical co-deposition of lithium and sodium has not been reported.

Although the non-dendritic growth of lithium addresses some of the safety issues, the electrochemical instability of lithium in contact with the electrolyte causes self-discharge

and capacity loss through reaction of the metal with the electrolyte. The formation of a stable, solid electrolyte interface (SEI) is necessary for graphite-based anodes to achieve stable performance and low self-discharge. SEI formation by itself is not an effective strategy for full dendrite elimination or high coulombic efficiency because of the high surface area and volume changes of the deposit. If the SEI layer were formed over a dendrite, it would leave a high surface area, empty shell upon reoxidation of the metal. In this study, an efficient SEI layer is formed on the non-dendritic lithium-sodium co-deposit.

4.2 Experimental

The initial electrolyte selection was driven by the need to electrodeposit sodium and lithium from the same electrolyte at high coulombic efficiency. EMI-$AlCl_4$ has already been shown as a suitable electrolyte for the deposition of both metals[65,66]. More recent studies have focused on TFSI-based ionic liquids where it was shown that these too are suitable for depositing both lithium and sodium[62,67]. For our work, we chose an aliphatic ammonium, trimethylbutylammoniun TFSI (N_{1114}-TFSI). Preparation of the EMI-$AlCl_4$ and N_{1114}-TFSI ionic liquid is detailed in chapter 3.

Inductively coupled plasma emission spectroscopy (ICP-ES) was used to determine the composition of deposits at different conditions. Samples were prepared by passing 0.2 coulombs (C) of a given potential. Samples were then washed in DMC to remove the viscous electrolyte and dissolved in a matrix of 5 vol% HCl and 2.5 vol% HNO_3 in deionized water. The sample solutions were passed through a 45µm syringe filter before analysis. The ICP-ES was calibrated with 100 ppm standards diluted with the same deionized water and then used to analyze the dissolved samples.

4.3 Results and Discussion

Cyclic voltammograms (CV) on tungsten, Figure 4.1, demonstrate electrochemical reduction of the both lithium and sodium subsequent re-oxidation of the metal on the positive-going potential sweep. It is interesting to note that the reduction potential for Li^+ and Na^+ in EMI-$AlCl_4$ are each more positive than their standard potentials. Li^+ reduction starts -2.15 V and Na^+ at -2.45 V vs. Al/Al(III), compared to their standard potentials of -3.01 V and -2.68 V vs. Al/Al(III) (-3.04 V and -2.71 V vs. NHE) for lithium and sodium, respectively[68]. This is most likely due to an interaction with the chloroaluminate anion, as no such shift occurs in imidazolium-TFSI ionic liquids[69]. In EMI-$AlCl_4$, sodium is reduced at a more negative potential than lithium but the oxidation peak, having a shallower onset, extends more positive of the lithium peak. Sodium redox reactions straddle those of lithium over the potential scale.

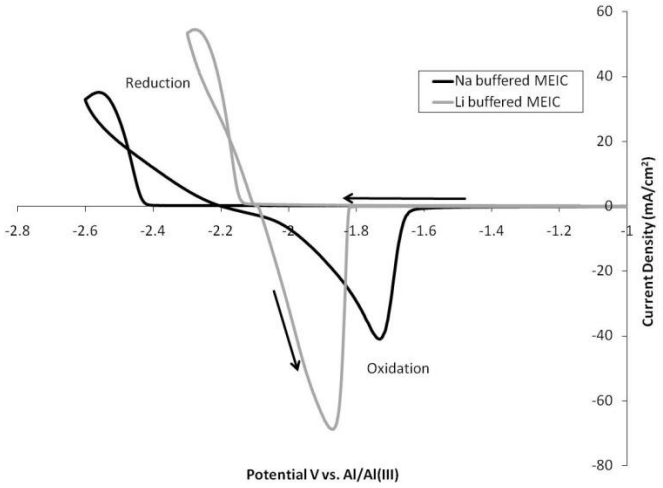

Figure 4.1: CV of Lithium and Sodium buffered EMI-$AlCl_4$ melts at 100mV/s.

The coulombic efficiency for deposition and re-oxidation of the metal can be calculated from the voltammograms as detailed in chapter 3. From Figure 4.1 the coulombic efficiency was 90% for lithium and 82% for sodium. For lithium, the loss of efficiency is likely due to the reaction of the electrolyte with the metal and the inefficiency of re-oxidizing dendrites, as described above. Sodium also reacts with the electrolyte and the loss of efficiency here may be greater than that of lithium since its reduction occurs at more negative potentials. Studies of the SEI on lithium in EMI-$AlCl_4$ electrolytes have found that the surface layer formed in this melt on lithium and sodium metals is not entirely stable. Parasitic reactions are thought to occur because of $AlCl_4$ and residual $Al_2Cl_7^-$ in the electrolyte[52,70,71]. Dark films were observed after extended exposure to the ionic liquid for both metals, but their composition was not studied in detail.

An unbuffered acidic EMI-$AlCl_4$ electrolyte can be reduced at -2.2 V on a tungsten electrode. The addition of $SOCl_2$ to the ionic liquid increases the stable potential range to -2.4 V, which coincides with the sodium reduction potential. There is a 200 mV overpotential and hysteresis for the reduction and reoxidation of sodium ions when deposited on a tungsten surface. The hysteresis and overpotential on the initial CV scan on tungsten has been attributed to the difficulty in nucleating sodium metal on a foreign surface (i.e. tungsten) possibly confounded by the presence of chloride or chloroaluminate species. Sodium oxidation also shows a low exchange current upon oxidation compared to lithium. The oxidation of sodium began at a potential negative of lithium, however, the mass-transfer limited oxidation peak did not occur until potentials positive of lithium.

Since ionic liquid electrolytes capable of depositing both sodium and lithium metal are available, the focus of this study shifted to the possible co-deposition of lithium and

sodium, and the potential to suppress dendrite growth. A 1:1 volume ratio of Li buffered EMI-$AlCl_4$ and Na buffered EMI-$AlCl_4$ ionic liquids were mixed and the behavior studied using cyclic voltammetry. Figure 4.2 shows the CVs for the 50%Li/50%Na electrolyte when scanned to several switching potentials. When the switching potential was -2.3 V, only a single oxidation peak was observed. This CV has many features in common with the CV from the pure lithium ionic liquid, Figure 4.1. The reduction current was characterized by an onset potential of -2.15 V followed by a sharply defined, single oxidation peak. When the switching potential was made more negative (i.e. -2.5 V and -2.7 V), a second oxidation peak appeared at -1.7 V upon scan reversal. This second peak matched closely to that seen for the pure sodium containing ionic liquid, Figure 4.1, in potential and in slope.

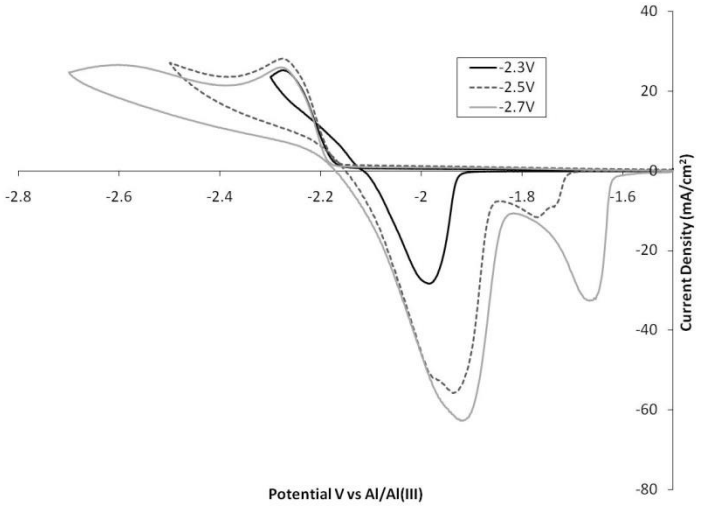

Figure 4.2: CV of 50%Li/50%Na EMI-$AlCl_4$ electrolyte at 100mV/s with different switching potentials.

That is, the combined Li/Na ionic liquid produced a CV which was the linear sum of the two separate ionic liquids. The peak at -1.7 V did not appear in the scan reversed at

-2.3 V because sodium would not have deposited at this potential. Sodium did deposit in the scans reversed at -2.5 V and -2.7 V and because of the sloped onset of sodium oxidation, Figure 4.1, the peak for the sodium oxidation process did not occur until -1.7 V. The shift in reduction potentials does suggest a role for chloride or chloroaluminate intermediates on the surface which can disrupt redox reactions.

To identify the composition of the two peaks in Figure 4.2, inductively coupled plasma emission spectroscopy (ICP-ES) was carried out on the solid deposits formed at constant potential. ICP-ES cannot distinguish between elements in the metallic (deposited) phase and the ionic (SEI) phase. This resulted in significant error because the electrolyte, containing both lithium and sodium, reacted with the metallic surface to incorporate both metals, even if only one was deposited. A control sample (Sample #1) was used to quantify this surface reaction. The ICP results are shown in Table 3.1.

Table 3.1: ICP-ES results showing elemental analysis of deposits from EMI-$AlCl_4$.

Sample	Li (ppm)	Na (ppm)	Li (mol%)	Na (mol%)
(1) Li buffered, contaminated	22.1	2.24	90.8	9.2
(2) 50%Li/50%Na dep at -2.2V	13.9	1.67	89.3	10.7
(3) 50%Li/50%Na dep at -2.6V	5.46	22	19.9	80.1

Lithium was deposited from a lithium buffered EMI-$AlCl_4$ ionic liquid to establish a baseline. The lithium deposit was then dipped in a sodium buffered ionic liquid to simulate contact with the mixed electrolyte (sample #1). The sample was rinsed with DMC to remove as much electrolyte as possible. This process introduced a 10% error in the elemental analysis. The analysis showed only 90.8% lithium and 9.2% sodium. The second and third samples shown in Table 1 were deposited from a 50%Li/50%Na EMI-

$AlCl_4$ ionic liquid at different potentials. At -2.2 V (sample #2), only the single oxidation peak, associated with lithium, was observed in the CV. The deposit was essentially all lithium, within experimental error of the control sample, #1. At -2.6 V (sample #3), the CV clearly shows two oxidation peaks with one each associated with lithium and sodium. The elemental analysis shows that at this potential, the deposit is 80% sodium. Thus, we conclude the oxidation peak at -1.7 V is sodium, while the oxidation peak at -2.0 V is mostly due to lithium.

To further understand this double peak, the deposit morphology was analyzed by examining metal topography at several different potentials. SEM images of these deposits from a 90%Li/10%Na EMI-$AlCl_4$ ionic liquid are shown in Figure 4.3. For comparison, SEM images of deposits from a lithium-only EMI-$AlCl_4$ ionic liquid are shown in Figure 4.4.

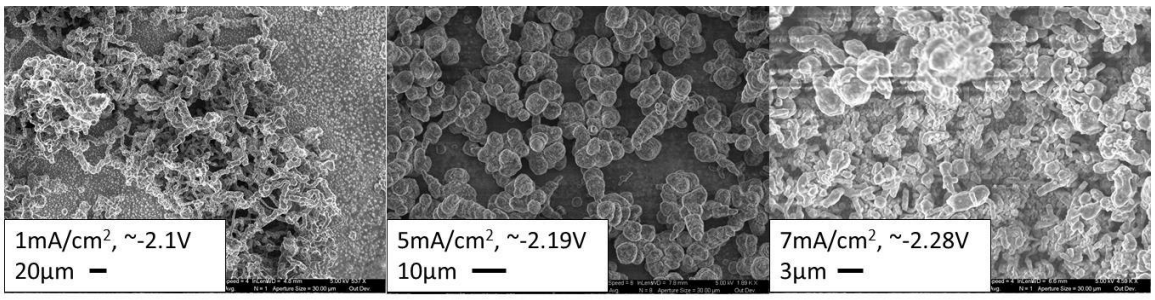

Figure 4.3: SEM images of deposits from a 90%Li/10%Na buffered EMI-$AlCl_4$ melt. Metal was deposited at the current shown until a charge of 5 C/cm^2 was reached.

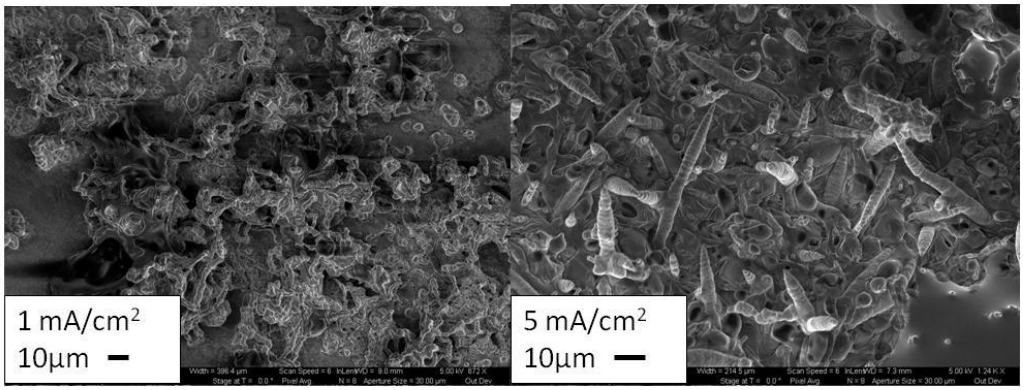

Figure 4.4: SEM images of typical deposits from a lithium buffered EMI-$AlCl_4$ ionic liquid.

The low current deposits (e.g. 1 mA/cm^2) produced from the pure lithium and 90%Li/10%Na EMI-$AlCl_4$ ionic liquids looked the same in structure. Curl-shaped dendrites formed moss-like structures on the substrate surface. At higher current density however, the deposit changed significantly. At 5 mA/cm^2 and 7 mA/cm^2, the lithium deposit formed straight, sharp needles (Figure 4.4). Deposits produced from the 90%Li/10%Na EMI-$AlCl_4$ ionic liquid showed only small, stunted, dendrites at 5 mA/cm^2. At higher current, 7 mA/cm^2, elongated structures were visible, but no sharp, needle-shaped dendrites could be found.

Based on the potentials recorded in the chronopotentiometry experiments, the disappearance of dendrites coincides with the appearance of the second oxidation peak in the CV, as shown in Figure 4.2. ICP results indicate that the appearance of the second peak coincides with an increase in sodium in the deposit. Thus it is likely that the co-deposition of sodium with the lithium hinders dendritic growth.

The suppression of dendritic growth could increase the coulombic efficiency for the deposition and reoxidation of the metal because of the lowered surface area that must

be passivated. Figure 4.5 shows the coulombic efficiency as calculated from the CV experiments as a function of switching potential from the Li buffered, Na buffered, and 50%Li/50%Na EMI-$AlCl_4$ ionic liquids.

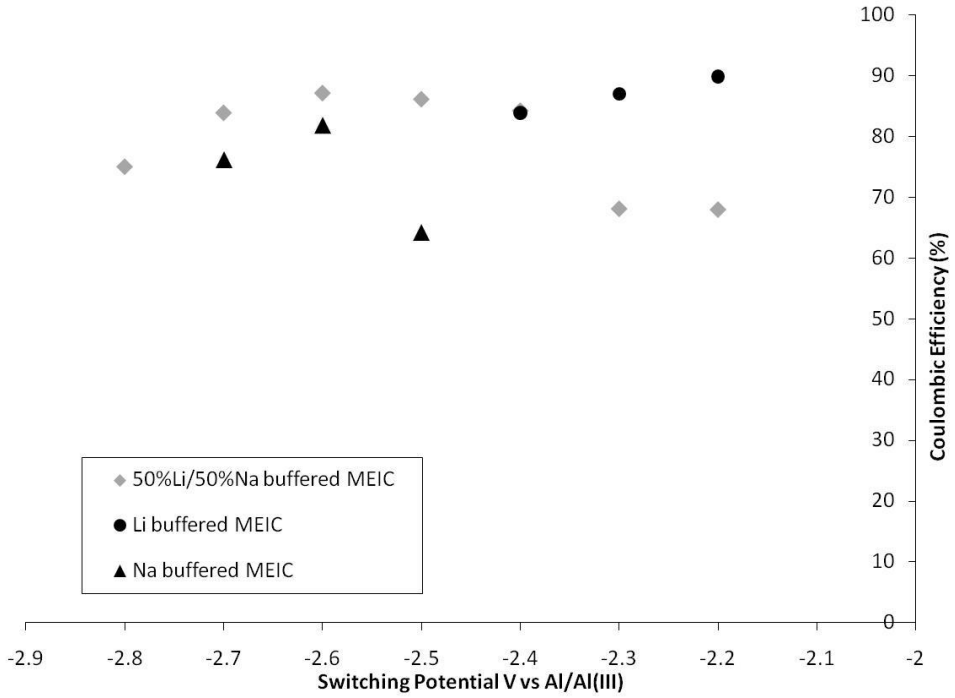

Figure 4.5: Coulombic efficiencies calculated from CV at different switching potentials.

The maximum coulombic efficiency obtained for lithium deposition/dissolution was 90% for a switching potential of -2.2 V. Scanning to more negative potentials lowers the efficiency because the EMI^+ reduction occurs within this potential range and a fraction of the charge could go toward the reduction of the electrolyte. At negative potentials outside the electrolyte stability window, electrolyte reduction was observed as gas bubbling from the substrate surface indication that the reduction of the EMI^+ results in gaseous products. For sodium, the highest efficiency was 82% at a switching potential of -2.6 V. At a switching potential of -2.5 V, a small reduction peak was recorded, but the

background current was not negligible causing the efficiency to drop. Again, going to more negative potentials lowered the efficiency because of electrolyte reduction.

Figure 4.5 also shows the coulombic efficiency for a 50%Li/50%Na ionic liquid. The maximum efficiency for this electrolyte, 87%, was achieved at a switching potential of -2.6 V. This efficiency is, unfortunately, not higher than that of the lithium-only though an optimum does occur at a potential that includes some sodium. It is likely that there is some benefit to the morphology change associated with co-depositing sodium, but because sodium also then lowers the efficiency compared to lithium, it appears that only a small amount is beneficial. The better electrolyte performance of the lithium/sodium electrolyte at a given potential than the sodium-only electrolyte, indicates that the higher coulombic efficiency of lithium, and better morphology of the deposit are having a positive effect.

Although dendritic growth was successfully suppressed in the EMI-$AlCl_4$ system, the change in morphology did not lead to a large increase in efficiency or cycle life. Use of cyclic carbonate SEI formers, such as EC and VC, was investigated; however, the chloroaluminate anion acts as a catalyst to polymerize cyclic carbonates[72]. No increase in coulombic efficiency was achieved using such carbonate additives. This makes the EMI-$AlCl_4$ ionic liquid unsuitable for efficient lithium cycling, as would be required for application in a lithium-metal anode battery.

Trimethylbutylammoniun TFSI (N_{1114}-TFSI) based ionic liquids have been shown to have better tolerance for water and oxygen contamination compared to their chloroaluminate counterparts. The shift in sodium and lithium reduction potentials described above in chloroaluminate ionic liquids does not occur to the same extent. This results in a more negative reduction potential which would lead to a higher voltage

battery. N_{1114}-TFSI has previously been shown to support lithium and sodium reduction and re-oxidation[62,67]. Electrochemical experiments were performed at a type 304 stainless steel working electrode because this substrate yielded better reversibility in the TFSI system. Figure 4.6 shows the CV behavior of 1 M Li N_{1114}-TFSI, 0.3 M Na N_{1114}-TFSI, and 1 M Li/0.1 M Na N_{1114}-TFSI. The low solubility of NaTFSI in N_{1114}-TFSI did not allow for testing at higher sodium concentrations.

The coulombic efficiency was calculated by integration of the reduction and oxidation processes from the CV scans. The coulombic efficiency was 55% for 1M Li N_{1114}-TFSI and 54% for 0.3M Na N_{1114}-TFSI. The reduction potentials for the two metal ions are -2.85 V for sodium and -2.75 V for lithium, which are more negative compared to EMI-$AlCl_4$, but close to the theoretical redox potentials. Co-deposition was studied using a mixed ionic liquid containing 1M Li/0.1M Na in N_{1114}-TFSI. The efficiency from the CV experiments in Figure 4.6 was 57%, which is slightly higher than that of the 1M Li N_{1114}-TFSI electrolyte. Contrary to the chloroaluminate ionic liquid, this mixture exhibited only a single oxidation peak, rather discrete peaks of the two metals.

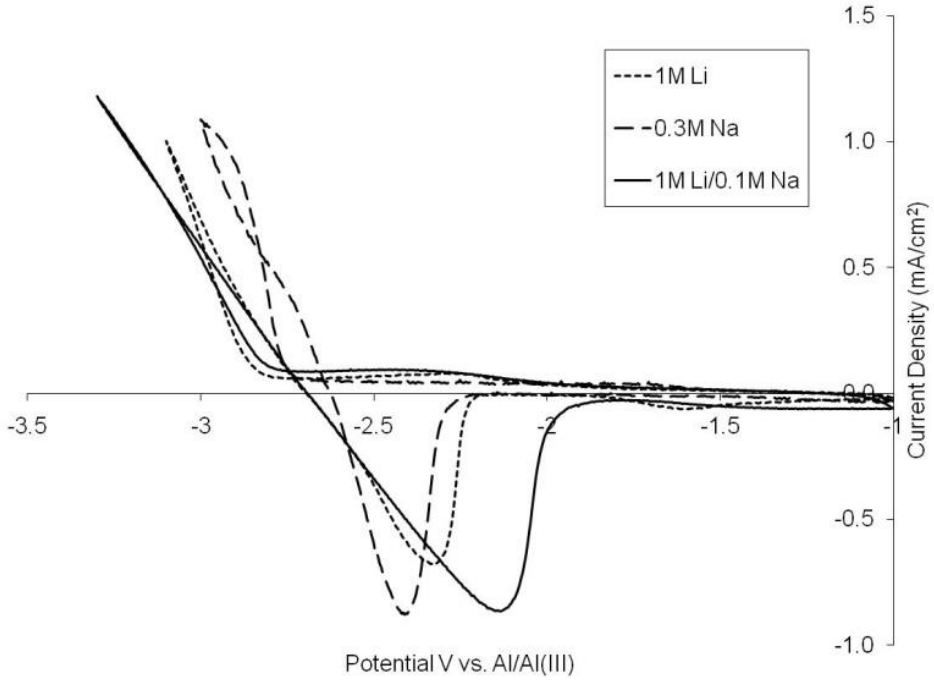

Figure 4.6: CV of 1M Li, 0.3M Na, and 1M Li/0.1M Na in N_{1114}-TFSI. Coulombic efficiencies were 55% for lithium, 50% for sodium, and 57% for the mixture. The scan rate was 10 mV/s.

Figure 4.7 shows deposit morphology from each ionic liquid. The lithium-only deposit shows long dendrites that are 1-2 µm diameter as well as some granular character, which was not observed in the EMI-$AlCl_4$. The 0.3 M Na deposit was very fine grained and shows no dendritic growth. The deposit shows some signs of pits and cavities forming as a result of the electrodeposition process, and is thus not completely smooth. The 1 M Li/0.1 M Na electrolyte, however, shows a granular, uniform film without dendrites. The addition of a small amount of sodium had the same non-dendritic effect shown with EMI-$AlCl_4$ earlier.

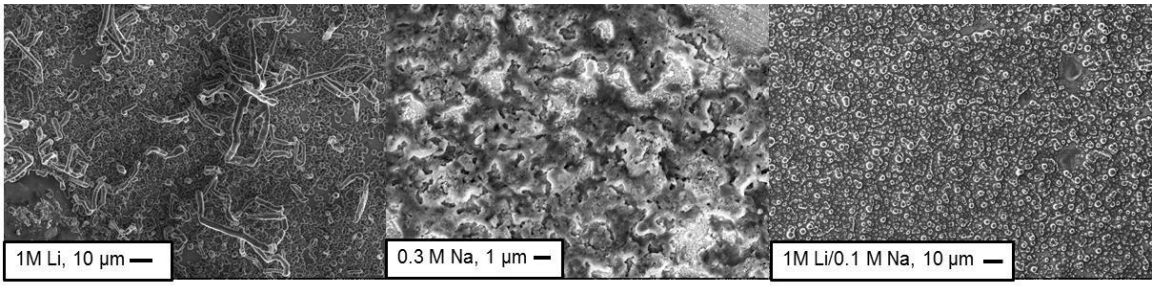

Figure 4.7: SEM images of deposit from a 1 M Li, 0.3 M Na and a 1 M Li/0.1 M Na electrolyte. A constant current of 0.1mA/cm^2 was applied for 1000s for 0.1C/cm^2.

Chronopotentiometry experiments consisting of full cycles were used to evaluate the redox character of the different electrolytes. Material was deposited for 100 s at 0.1 mA/cm^2 followed by re-oxidation at the same current density (see chapter 3). The coulombic efficiency was calculated from these chronopotentiomery experiments and the results are shown in Figure 4.8. The efficiency of 1 M Li N_{1114}-TFSI ionic liquid increased through the first 10 cycles until a value of 70% was reached and remained relatively constant for more than 100 cycles. No significant change in efficiency was observed with the ionic liquid mixture of 1 M Li/0.1 M Na compared to the 1 M Li in N_{1114}-TFSI. This is also similar to the results from the EMI-$AlCl_4$ electrolyte, where despite the better morphology, no increase in efficiency was observed. In both electrolytes, the coulombic efficiency of sodium was lower than that of lithium, thus the coulombic efficiency of the mixed ionic liquid could again simply be a linear combination of lithium and sodium separately.

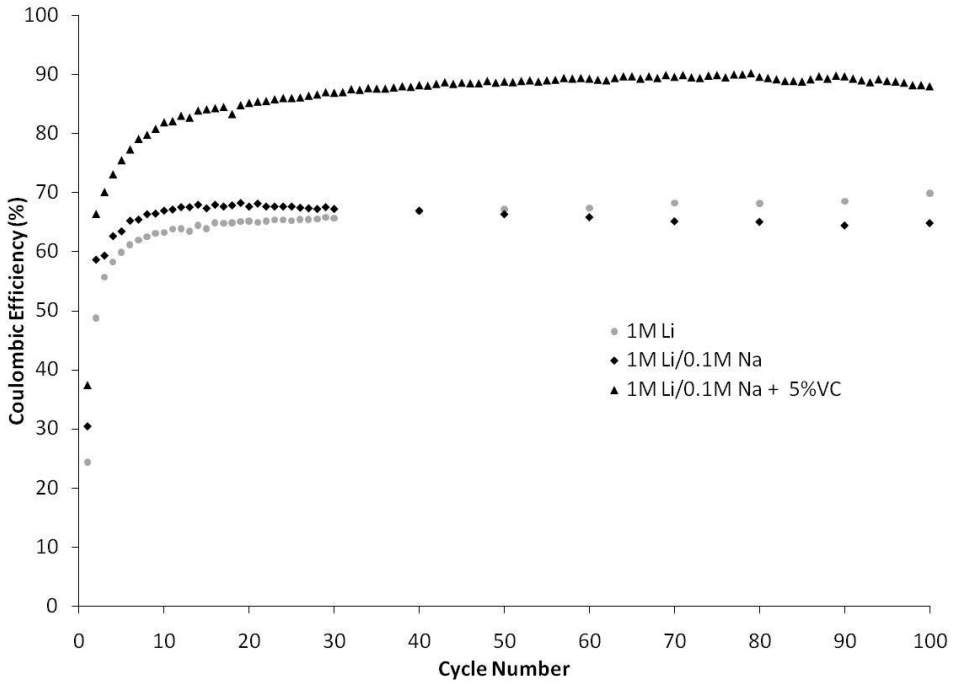

Figure 4.8: Cycling experiments at 0.1 mA/cm^2 for 100 s in N_{1114}-TFSI.

The continued loss of efficiency, despite morphology improvement, could be because of sustained reaction between the metal deposits and the electrolytes, which can be attributed to the lack of an adequate SEI layer. Vinylene carbonate (VC) was evaluated as an SEI forming additive. In these experiments, 5 wt% VC was added to a 1 M Li/0.1 M Na N_{1114}-TFSI electrolyte. CV and chronopotentiometry experiments were carried out as described before. The coulombic efficiency calculated from CV experiments was 60%, which is higher than the 1M Li or 1M Li/0.1M Na ionic liquids without VC. The cycling performance also greatly improved. The coulombic efficiency calculated from chronopotentiometry reached 85% within 30 cycles and reached a steady value of 90% through 100 cycles (Figure 4.8). The improvement in cycling behavior is credited to a lower reaction rate between the deposit and the electrolyte. Vinylene carbonate can react with the deposit over multiple cycles to form a stable film that prevents further reaction.

4.4 Summary

Two ionic liquids, EMI-$AlCl_4$ and N_{1114}-TFSI, have been studied as electrolytes for lithium metal batteries. Both have a large electrochemical stability window to support lithium deposition and dissolution, making them candidates for lithium battery applications. The approach to mitigating the dendrite growth, which currently prevents lithium metal anodes from becoming commercially viable, was to add a small amount of sodium to the lithium electrolyte. A non-dendritic co-deposit was achieved by both ionic liquid electrolytes. Since sodium is non-dendritic in nature, the non-dendritic co-deposit likely results from a physical blocking of lithium's active dendritic sites.

A second issue with forming a successful lithium metal anode is that lithium reacts with the electrolyte, causing capacity loss and blocking the substrate. This problem was approached with SEI forming additives. These additives can react with the deposited metal to form a stable, protective film that prevents further reaction.

In this work, we have shown that both EMI-$AlCl_4$ and N_{1114}-TFSI support non-dendritic deposits by the addition of a small amount of sodium to a lithium-based ionic liquid. Additives were studied with N_{1114}-TFSI and it was shown that 5% VC added to a 1 M Li/0.1 M Na N_{1114}-TFSI ionic liquid could help build a stable SEI, resulting in a cycling efficiency of 90% over 100 cycles. Despite this increase in coulombic efficiency, a battery application requires a coulombic efficiency of ~99.99% to last 600 cycles, so the need for improvements remain.

5. The Role of Dissolved Gas in Ionic Liquid Electrolytes

5.1 Objective

Because of lithium's reactivity, the formation of a stable SEI is imperative to prevent the irreversible reaction between lithium and the electrolyte. On a graphite anode, the SEI is supported on the graphite surface while the lithium ions intercalate into the bulk. The SEI on the surface of the lithium metal must form directly on the active material, which is more difficult than a host-type anode due to the dissolution of metal surface upon oxidation during cycling. Vinylene carbonate and other additives have been successfully used as SEI forming agents but have not completely solved the lithium anode stability problem.[25,73,74]

In this chapter, dissolved gases were investigated for their role in forming the SEI on the metal surface. Lithium batteries can be assembled in the absence of ambient water vapor (i.e. dry rooms) where the electrolyte is saturated with air[74–77]. Gases dissolve in the electrolyte in small amounts and can thus be used the affect the SEI in controlled ways. This effect has been studied for organic electrolytes such as propylene carbonate[78] and ethylene carbonate/diethyl carbonate[75]. Aurbach et al., also studied the effect of water and oxygen contamination on the SEI in dioxolane and γ-butyrolacetone[17,79]. No such study has been conducted for ionic liquid electrolytes, which interact differently with gases than their organic counterparts. The effect of atmosphere, including oxygen, nitrogen, argon, carbon dioxide and under vacuum are studied here.

Regarding gas solubility, ionic liquids have received attention as a carbon dioxide capture medium. In particular, researchers have investigated imidazolium-based ionic liquids for CO_2 capture because of the high solubility of CO_2. Data comparing CO_2, N_2, and O_2 solubility in ionic liquid have been reported[80–84]. $TFSI^-$, the anion used in the study, was shown to increase gas solubility over ILs with PF_6^- and BF_4^- anions[84]. In battery applications, soluble gases can be used to deliver small amounts of potentially SEI forming reactants. N_2 and O_2 can both react with lithium and be potential components of the SEI. The effect of dissolved gas on the lithium metal SEI and cycling efficiency are investigated in this study.

5.2 Experimental Set-up

In order to study the effect of gases on the lithium redox reaction, a specialized beaker-cell with connections for two electrodes and a gas port was constructed for maintaining the ionic liquid under saturated conditions with each of the gases during the electrochemical cycling experiments (Figure 5.1). The ionic liquid was taken from vacuum line into an argon filled glovebox and transferred into the modified beaker cell for the experiment. The gas port allowed for bubbling of a test gas before starting the electrochemical experiments. During the electrochemical experiments, the head space above the ionic liquid was maintained with the same test gas to avoid contamination from the ambient. A second cell of similar design was used to for the experiments under vacuum. The vacuum cell had ground glass joints and vacuum tight electrical feedthroughs. The cell was leak tested with a helium lead detector before use.

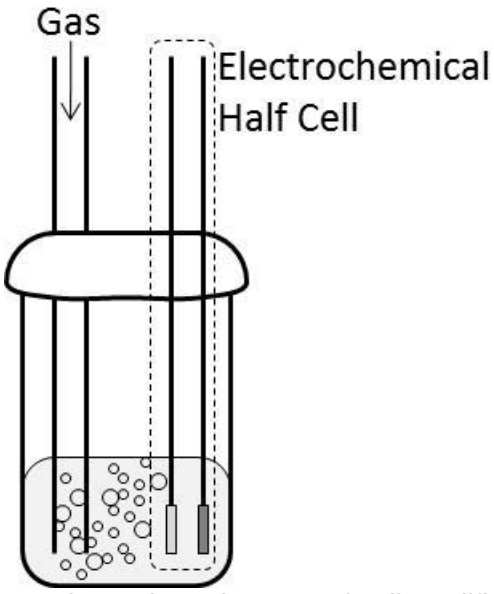

Figure 5.1: Schematic and Image of cell modified for gas bubbling.

The shallow cycling method detailed in chapter 3 was used for these experiments. This method, based on excess lithium, provides the best coulombic efficiency for the lithium redox system. The electrochemical half cell consisted of a stainless steel foil as the substrate and a lithium foil as the counter and reference electrode.

5.3 Results and Discussion

Ionic liquids absorb ambient gas from the surroundings, but can be degassed by placing them under vacuum. The absorbed gas can be observed as bubbles leaving the liquid. In this work, the ionic liquid was saturated with specific gases to determine their effect on SEI formation and the coulombic efficiency of Li-metal cycling. The gases evaluated include argon, oxygen, nitrogen, dry air, and carbon dioxide.

A 1M Li^+ ionic liquid electrolyte was bubbled with nitrogen gas for 15 min, 3 h, and 6 h followed by measurement of the cycling efficiency. After the initial bubbling period, the

gas of interest was maintained in the head space of the cell so that the electrolyte would be blanketed with the proper gas during the experiment. The electrolyte was allowed to settle for 10 min before the cycling experiment began. The coulombic efficiencies calculated from these experiments are shown in Figure 5.2.

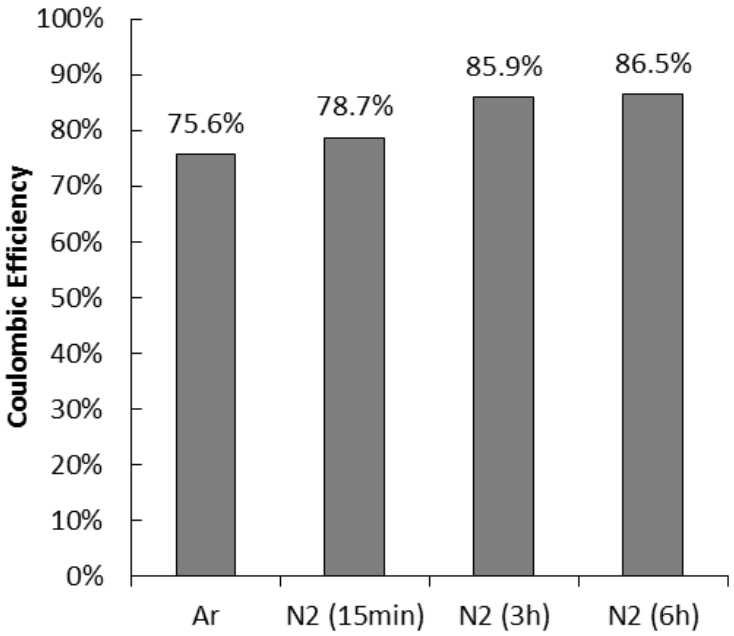

Figure 5.2: Coulombic efficiency plotted for different gas bubbling times.

The coulombic efficiency using argon gas, 75%, was used as a reference. Argon was chosen as a reference because it is not reactive with lithium metal and is commonly used in gloveboxes. After 15 min of nitrogen bubbling, the coulombic efficiency increased slightly compared to the argon reference. A longer nitrogen bubbling time, 3 h, led to higher coulombic efficiency values, however, no further improvements were observed by extending bubbling times beyond 3 h. These results indicate that the time required for the electrolyte to saturate and equilibrate with the ambient is about 3 h.

Each subsequent experiment was started with the cell assembled in the argon glovebox and the same saturation time of 3 h was used for each gas.

Figure 5.3 shows the coulombic efficiency for lithium with different gases bubbled for 3 h prior to the experiment. The vacuum experiment was conducted as a control since little or no gas should be present in the system. The experiments under vacuum and argon yielded similar coulombic efficiencies, which confirms that argon has essentially no effect on the coulombic efficiency. In these cases, the SEI is formed solely from ionic liquid components. An increase in coulombic efficiency was seen when the cell was purged with oxygen or nitrogen. Dry air, being mainly a mixture of nitrogen and oxygen, also showed higher coulombic efficiency over the argon case but did not perform as well as nitrogen and oxygen individually. Dry air also contains a small amount of carbon dioxide. When the cell was purged with carbon dioxide, a pronounced decrease in coulombic efficiency was observed. The potential curves for all cycling experiments were similar, showing an overpotential of 50-60 mV vs. Li/Li^+. This indicates no major changes in conductivity as a result of the gas treatment. SEM observation of deposited samples showed no major differences in the surface structure of the lithium. Samples were characterized by mossy and dendritic growth, as expected from previous work[85,86]. The main difference between the samples here should be the SEI layer formed to passivate the lithium surface. ToF-SIMS was used to sputter into the sample and an elemental depth profile of the SEI and sample was obtained.

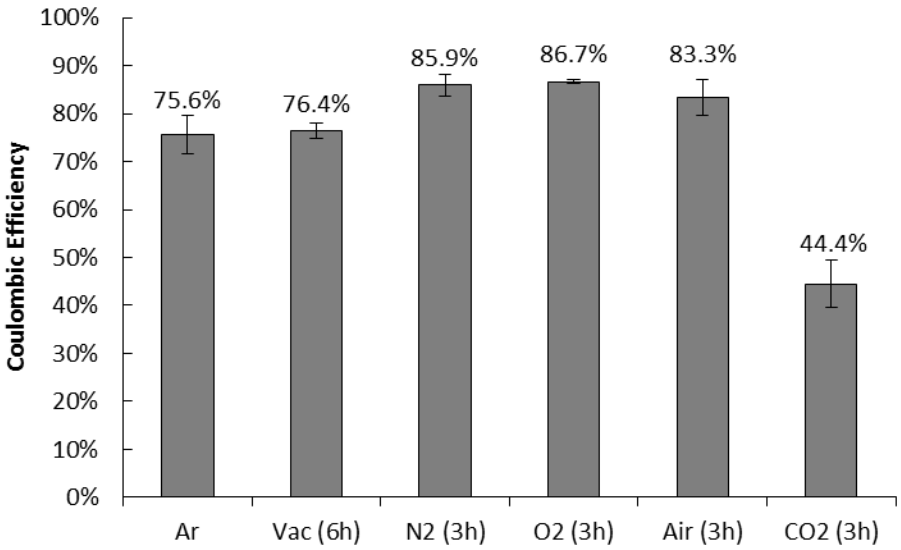

Figure 5.3: Coulombic efficiency for a lithium anode in ionic liquid bubbled with different gases.

Figure 5.4 shows a typical depth profile of a lithium sample deposited under argon. Normalized counts are plotted vs. the sputtering time, which is proportional to sample depth, assuming uniform sputtering rate between the different layers on the lithium surface. The sensitivity factor for each species was not determined so an exact mole fraction of each material could not be calculated. The SEI was clearly observed as a layer of LiF on the surface extending to ~60 s depth, where depth is expressed as a sputtering time. During the course of the experiment, Li^+ and Li_2^+ signals increased indicating bulk lithium was reached. Li_2^+ represents a lithium cluster peak that appears when the bulk Li deposit was reached. This makes it a good indicator for the SEI thickness. The Li_2O^+ peak was not tracked because it overlaps with a prominent surface species distorting the results. Instead, the LiO^+ peak is shown. LiO^+ is a natural byproduct of Li_2O^+ during ion bombardment and shows the expected trends. Peaks for Li_3N^+ and $LiOH^+$ were also tracked and did not appear to be significant. When saturated with argon, the SEI was primarily composed of a LiF layer on the surface.

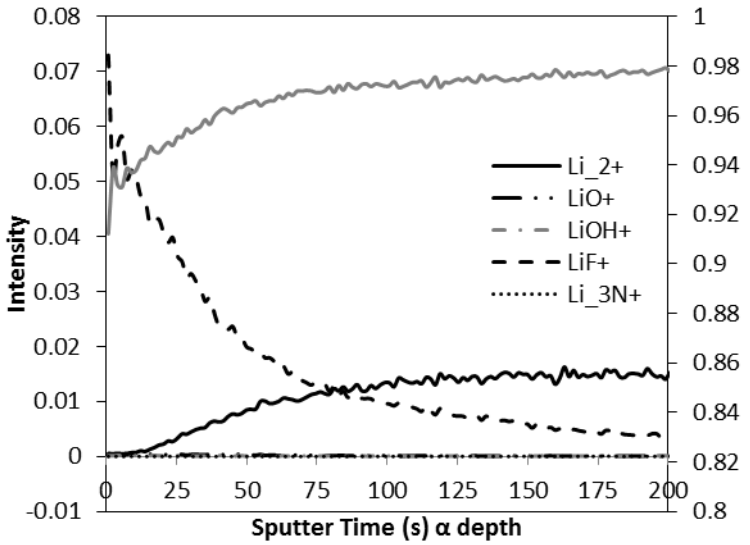

Figure 5.4: SIMS depth profile of sample deposited under argon atmosphere.

Depth profiles of samples when the ionic liquid was saturated with dry air, oxygen and nitrogen are shown in Figure 5.5. Each profile shows a dominate LiF^+ peak at the surface with Li_2^+ increased after a decrease in LiF^+. Surprisingly, Li_3N^+ and LiO^+ were absent from all profiles in Figure 5.5 even though they are possible reaction products produced between lithium and nitrogen or oxygen. That these reaction products are soluble in the electrolyte and simply do not become part of the SEI is not ruled out but chemically, the SEI appears to remain a layer of LiF regardless of absorbed gas. This is a sharp departure from previous results by Momma et al. and Younesi et al., who conducted similar experiments in organic electrolytes[75,78]. Specifically, Momma et al. observed Li_3N in the SEI when conducting experiments in dry air, however, no Li_3N or its fragments were observed in several iterations of our experiments.

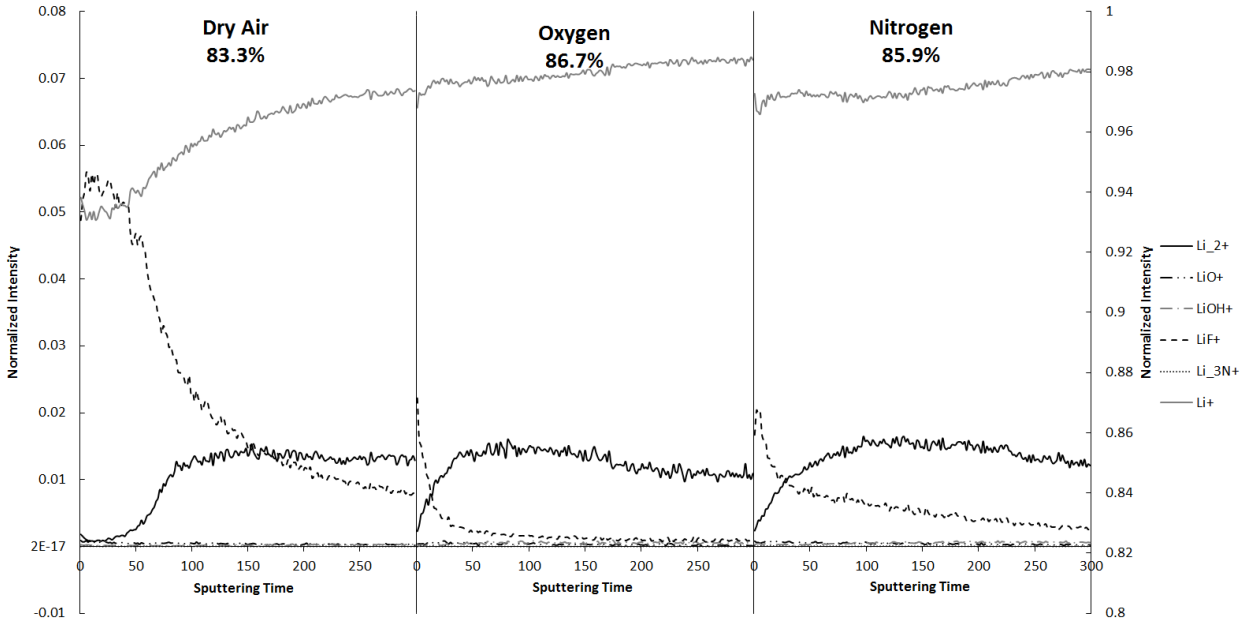

Figure 5.5: SIMS depth profiles for lithium samples deposited under nitrogen, oxygen and dry air.

The lack of reaction with oxygen and nitrogen is consistent with the fact that lithium reacts quickly with humid air but only slowly with dry air. The thermogravimetric analysis (TGA) by Markowitz et al. showed no weight gain under dry gas, thus no reaction was observed with lithium metal[87,88]. In addition to the slow reaction with nitrogen or oxygen under dry conditions, the gases are present in the ionic liquid at relatively small concentrations compared to the concentration of the ionic liquid components. Thus, LiF formation due to reaction between lithium and the ionic liquid is favored.

There appears to be a significant difference is in the thickness of the SEI layer formed depending on the different ambient gases used. Under argon, the thickness of the SEI corresponded to 60 s sputtering time and the coulombic efficiency was 75%. For oxygen and nitrogen, the coulbombic efficiency was 86% and the thickness of the SEI corresponded to 20 s of sputtering time. Finally, under dry air, and coulombic efficiency was 83% and it took 150 s to sputter through the SEI. The coulombic efficiency

correlated with the thickness, except for the dry air case. Dry air has a coulombic efficiency near nitrogen and oxygen, but an SEI thickness close to the argon sample. The apparent inconsistency with dry air may be explained by the presence of carbon dioxide. Carbon dioxide was quite detrimental to the coulombic efficiency. A depth profile of the SEI formed in carbon dioxide ambient, Figure 5.6, has a very thick layer of LiF, requiring 250 s sputtering time to reach the lithium. In addition, there was no rise of Li_2^+ as seen in other profiles. When the experiment was conducted in carbon dioxide ambient, bulk lithium deposition was inhibited and a large amount of LiF was produced.

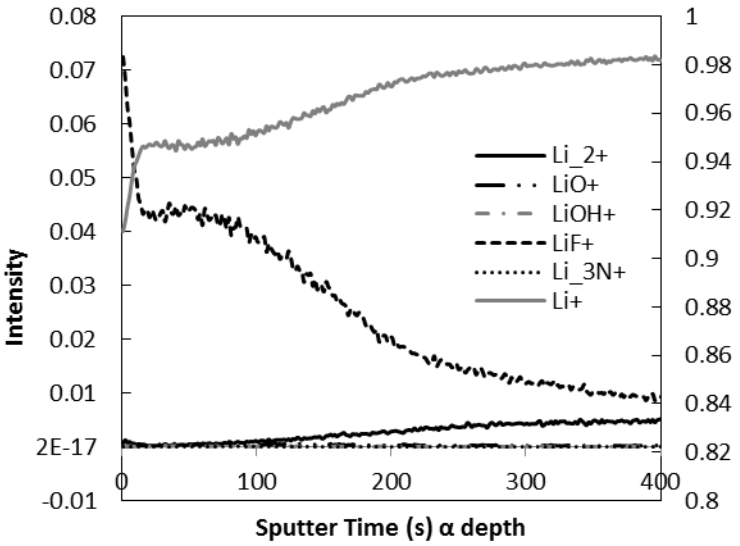

Figure 5.6: SIMS depth profile of sample deposited in carbon dioxide ambient.

Of the gases tested, carbon dioxide formed the thickest SEI. According to Condemarin et al., Henry's constant for carbon dioxide is 60 atm, while oxygen and nitrogen were not detectable[80]. No data was found for argon solubility. TFSI-based ionic liquids have the highest affinity for CO_2 regardless of cation[84,89]. Separation of the anion and cation was observed at high CO_2 pressures, no separation would be observed at

ambient pressures as in this experiment[90]. The association of CO_2 with $TFSI^-$ seems to inhibit lithium ion reduction and allow direct electrolyte reduction and degradation. The salt, Li-TFSI, could also be affected by the presence of carbon dioxide.

In an attempt to quantify the amount of SEI formed on each sample, two methods were used to estimate the SEI thickness. First, the SIMS depth profiles were converted to depth assuming the materials here sputter at the same rate as a standard material. The sputter rate of gold was experimentally measured at the same sputtering conditions used in the lithium experiments and found to be 5.2 nm/s. Gold was chosen because it has a molecular weight-to-density ratio similar to lithium, which is a determining factor in the sputter rate. The time to sputter through the SEI was determined from the SIMS depth profile and converted to thickness. Second, the SEI thickness was calculated assuming that LIF formation is the sole cause of the loss in coulombic efficiency. The theoretical LiF thickness was calculated by assuming that all lost charge in the cycling experiments (i.e. all lost lithium) went to form LiF instead of metallic Li. By assuming a bulk density for LiF, a thickness can be calculated. The results of these two methods are shown in Table 5.1. The SEI thickness correlates very well with the loss of efficiency. A thinner SEI leads to a higher efficiency, lending credibility to the second method for calculating SEI thickness.

Table 5.1: Comparison of SEI thicknesses based on SIMS and efficiency calculations.

	Ar (75%)	N2/O2 (85%)	CO2 (44%)
Thickness based on Au sputter rate	312 nm	104 nm	1300 nm
Thickness calculated from coulombic efficiency	255 nm	152 nm	570 nm

For the argon, nitrogen, and oxygen samples, the two thickness approximations shown in Table 5.1 are in reasonable agreement. Given that lithium deposits are uneven by their nature and the deposit itself not evenly distributed, the calculated and experimental thicknesses are similar. For carbon dioxide however, the second method, loss of coulombic efficiency, gave a smaller value compared to the sputtering rate measurement. This could be due to a difference in density of the LiF formed when carbon dioxide was present, which could change the sputter rate. Encapsulation of the electrolyte could make the SEI thicker than what would be expected from pure electrochemical reactions. Considering the lack of bulk lithium formed, as evidenced by the low Li_2^+ peak, it is likely that higher molecular weight reaction products are present in the SEI layer. Peaks for the fragments of the N_{1114} cation were found throughout the carbon dioxide depth profile suggesting an increased breakdown of the ionic liquid which would also affect the sputtering rate. The presence of residual ionic liquid on the surface complicates analysis of the exact products on the surface. Another possibility is that some of the LiF formed in the carbon dioxide electrolyte was due to direct reaction between lithium and Li-TFSI, rather than electrochemical reduction. The association of $TFSI^-$ with carbon dioxide may destabilize the salt causing additional, non-electrochemical side reactions that would not be captured by the coulombic efficiency measurement.

5.4 Summary

Lithium metal deposition and re-oxidation was studied under different gas atmospheres in an attempt to evaluate the SEI formed. Cycling experiments were conducted to determine the efficiency of a lithium metal anode under these conditions. SIMS depth profiling was performed on samples deposited under the same conditions to

analyze the SEI layer formed. Nitrogen and oxygen atmospheres resulted in higher coulombic efficiency compared to argon. An experiment under vacuum confirmed that argon does not affect the SEI formation. Carbon dioxide had a detrimental effect on cycling efficiency.

The chemical make-up of the SEI was similar regardless of atmosphere, consisting of LiF. This is a departure from similar studies in which composition changed to include more oxygen and/or nitrogen species. That cycling efficiency increases with exposure to nitrogen, oxygen, and to a lesser degree air, makes this electrolyte promising for lithium-air batteries when paired with a water rejecting membrane. A correlation between the thickness of the SEI and cycling efficiency was observed, thus the lower efficiency comes from the active material and charge lost through formation of the SEI. The SEI layer thickness in carbon dioxide ambient does not correlate as well as the other gases. Carbon dioxide does not change the underlying structure of the IL, rather, it occupies the free volume in the IL and solubility is particularly in high in IL's with with fluoroalkyl groups[89,90]. Carbon dioxide associates strongly with the $TFSI^-$ and likely destabilizes the ionic liquid and salt causing other side reactions.

6. Nucleation of Electrodeposited Lithium Metal

6.1 Objective

Lithium electrodeposits are shown to be dendritic in nearly every electrolyte. Images of these impressive structures are usually taken after extended cycling or longer term chronopotentiometry or chronoamperometry experiments. This allows for the observation of several dendrites in one frame, thus easing characterization of length and diameter distributions. These later-term deposits also show the degree of entanglement and any orientation that may be present. In contrast, few studies show images of short-term deposits and no nucleation studies have been performed.

At its early stages, the current recorded for a potential step is very sensitive to the geometry and active area of the deposit. While the macroscopic current may be similar, trends in the real active surface area of the deposit can lead to vastly different local current densities and deposition rates (material flux). These current densities, can in turn affect the SEI formation on the active area. The dendritic and non-dendritic lithium deposits observed from N_{1114}-TFSI ionic liquid present two distinctive morphologies, which result in different active areas given the same volume of material. By calculating the deposition rate based on the active area and plotting this value over time, we can draw conclusions about the effect of the SEI layer on the deposit as a whole.

6.2 Theory

A typical current-time transient resulting from an applied potential is shown in Figure 6.1. When a potential is applied to an electrode to nucleate a foreign surface, an initial

current peak is observed. This peak corresponds to the non-faradaic current of the double layer formation. At slightly longer times, nuclei grow unencumbered in the area labeled i_{free}. In this segment, the current recorded is directly proportional to the active surface area of the deposit, making this the segment of interest where the active area can be determined and the local deposition rate can be calculated. As nuclei continue to grow in size, they start to overlap and no longer grow independently. At this point the active area becomes equal to the superficial area of the substrate. Because the active area associated with dendritic and non-dendritic growth differs significantly, the local current density will also be quite different even if the overall current profiles look similar. Analysis of the initial growth of nuclei can lead the local current density and growth rate that can explain macroscopic trends.

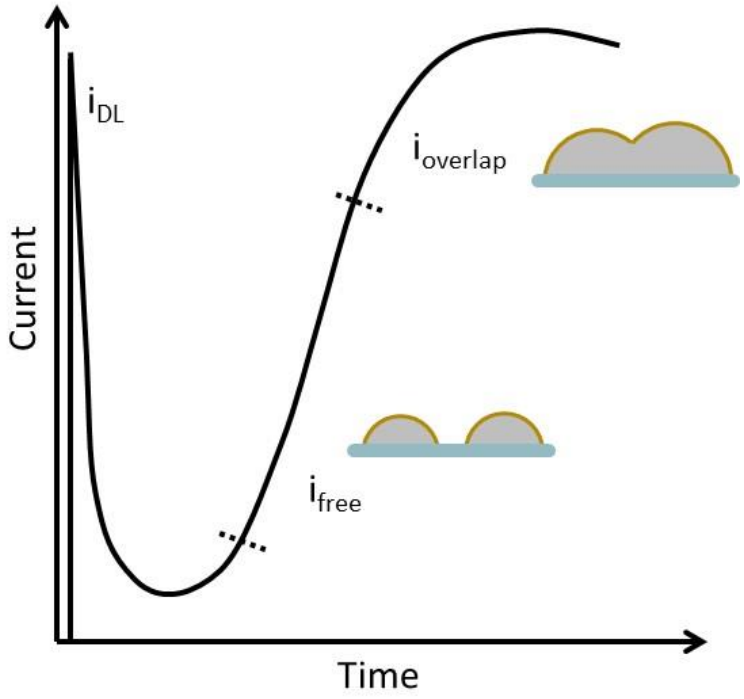

Figure 6.1: Generic current-time trend observed at constant potential for nucleation on a foreign surface (reproduced with permission)[4].

At short times, the observed current is a direct result of the surface area available due to the growing nuclei. This current can be broken down into the total area of all nuclei, *A(t)*, a potential dependent rate, *k(t)* in mol/cm^{2}s, Faraday's constant, *F*, and the equivalents per mole, *n*, as shown in equation 6.1. At a given time, t_g, the total active area, *A(t)*, is a function of the number of nuclei and the average area per nuclei as in Equation 6.2

$$i(t) = A(t) \cdot k(t) \cdot nF \tag{6.1}$$

$$A(t_g) = (\#of\ nuclei, N)\left(\frac{average\ area}{nuclei}\right) \tag{6.2}$$

Because the experiment is conducted under constant potential, the rate at which material adds to the surface, *k(t)*, is ideally a constant in the absence of surface layers or other conditions that might limit the rate. The total active area, *A(t)*, will grow depending on the geometry and number of the nuclei. A single atom adding material equally in all directions will grow into a hemisphere. For the three-dimensional growth of this nuclei, the current will be proportional to the square of the time based on the area of a hemisphere with growing radius (Equation 6.3). A potential dependent constant, *E*, includes the rate, *k*, which is assumed to be a constant for this ideal case. The potential-dependent constant is shown in equation 6.4, where *M* is the molecular weight in g/mol, *ρ* is the density in g/cm^3, *n* is the number of equivalents per mole and *F* is Faraday's constant. Finally, *k* is the potential-dependent deposition rate in mol/(cm^{2}s). The cm^2 area in the denominator refers to the active area (nuclei area), not the superficial

substrate area. This deposition rate, *k*, itself is directly proportional to the local current density by a factor of *nF*.

$$i = E \cdot t^2 \tag{6.3}$$

$$E = 2\pi \left(\frac{M}{\rho}\right)^2 nFk^3 \tag{6.4}$$

The current in equation 6.3 applies to a single growing nuclei but an applied potential will result in many nuclei populating the surface, thus an equation for the nucleation rate is required to compute the total area at any given time. The first order nucleation law based on a maximum number of available sites, N_0, and a nucleation constant, *A*, is given in Equation 6.5. Since the geometric model will focus on short times, *t*, and slow nucleation rates (low overpotential) we can simplify this nucleation rate to give a linear dependence as in Equ. 6.6.

$$N = N_0 \left(1 - exp(-A \cdot t)\right) \tag{6.5}$$

$$N \approx N_0 A \cdot t \tag{6.6}$$

When taken together, Equations 6.3 and 6.6 can be used to calculate the total area of all nuclei. Because nucleation and growth occur simultaneously, integration of the nucleation rate and the current expression for a single nuclei is required. The

expression for the current resulting from simultaneous nucleation and growth for hemispherical nuclei is given in Equation 6.7 where *u* is the time at which an individual nucleus is formed and $f_i(t)$ is the current resulting from an individual nucleus (Equation 6.3). Integrating this expression gives a general equation for $A(t)$ multiplied constants, including the rate *k*. This final expression for the current is given in Equation 6.8. The full integration is shown in Appendix B.

$$i = \int_0^t \left[\frac{\partial N}{\partial t}\right]_{t=u} f_i(t-u)du \tag{6.7}$$

$$i = \frac{AN_0 2\pi M^2 nFk^3}{3\rho^2} t^3 \tag{6.8}$$

Depending on the geometry of the deposit, the time dependence coming from the growth of a single nuclei ($f_i(t)$, Equation 6.3), will change. For one dimensional growth there is no time dependence, while two-dimensional growth will result in a linear growth of area with time for a single nuclei. This varying time dependence based on geometry will allow us to evaluate the current associated with dendritic and non-dendritic growth accurately.

Equation 6.8 gives an ideal current without mass transfer limitations to the surface. In the electrolyte/lithium-metal system however, formation of the SEI can limit lithium ion reduction and distort the growth of nuclei. This would result in a non-constant rate, *k*, because as the SEI changes with time so does the flux through it. Because the rate *k* is time dependent in our system it would also affect the active surface area and have to be

integrated in equation 6.7. However, the general function for k is not known, complicating the analysis.

The basis of the model rests on the idea that at a given time, t_g, the current is a function of the number of nuclei, the average area/nuclei, the potential dependent rate *k*, and Faraday's constant as shown in Equation 6.1 and 6.2. Because the non-constant rate k, results in an unpredictable area-time relationship, we cannot solve the general equation for current with time. However, we can determine the area at any given time experimentally by holding a substrate at a given potential for that time, and then analyzing the resulting deposit in an SEM. By analyzing images of the deposit we can determine the average area/nuclei from the diameter of the particles as well as the density of nuclei on the surface. These two elements can be used to determine the active surface area of the sample at any given time. The current is also known, allowing us to solve for the rate, *k*, using Equations 6.1 and 6.2. A non-constant deposition rate with time suggests an external factor, in our case SEI formation coupled with dendritic growth, which can then be examined based on the deposition rate's trend.

6.3 Experimental

Stainless steel foil was used as the substrate and working electrode for nucleation experiments. The counter and reference electrode was a lithium foil. Data on the nucleation rate was derived from SEM images of samples under applied potential for a specific amount of time. A standard grain counting method was used to determine the number of nuclei/area. To determine the number of nuclei without over-counting the ones at the edge of the area of analysis, a box with "hard" (red) and "soft" (blue) lines was drawn on an SEM image as shown in Figure 6.2. The area density of nuclei can be

determined by counting all nuclei within the box in addition to all nuclei that cross the soft lines. Nuclei that cross the hard lines are omitted. The total number of nuclei is divided by the area of the box (area of analysis). The advantage of this method is that if two areas are analyzed, no nuclei are counted twice. The method is thus not affected by the size variations of the selected area of analysis.

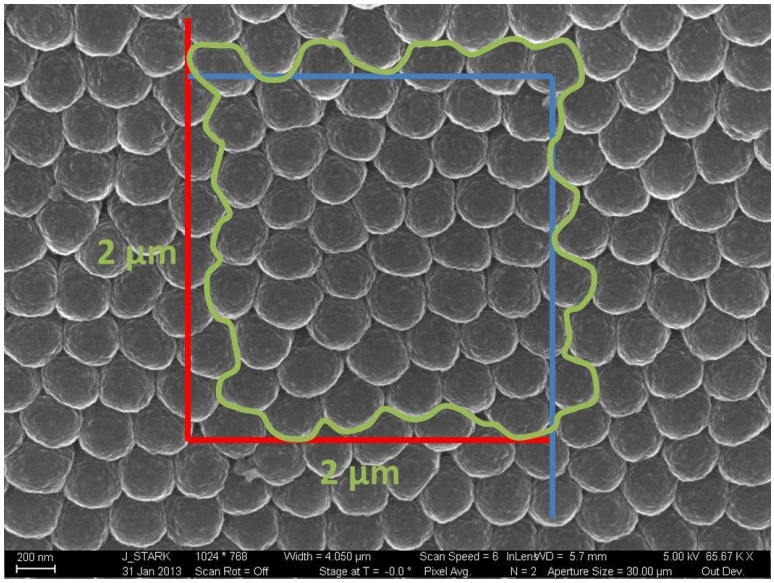

Figure 6.2: Nuclei density determined from SEM images using a common grain counting method. Counted nuclei are outlined in green.

6.4 Results and Discussion

The initial stages of lithium growth form the basis for the build-up of a bulk lithium deposit, as would be used in a lithium metal battery anode. Samples were examined by scanning electron microscopy (SEM) after different deposition times using the organic

electrolyte. A stainless steel foil electrode was polarized to -150 mV vs. Li/Li^+ in a 1 M $LiPF_6$ EC:DMC electrolyte for a specific amount of time. A progression of SEM images is shown in Figure 6.3.

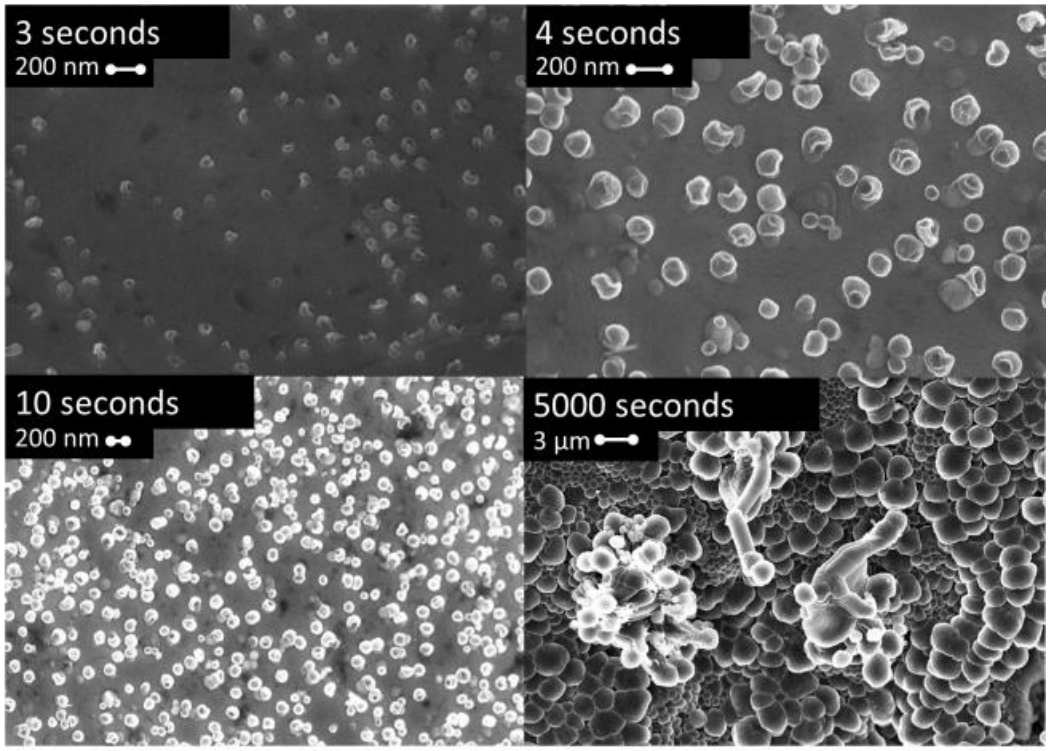

Figure 6.3: Progression of lithium electrodeposition from 1 M $LiPF_6$ EC:DMC. Hemispheric nuclei appear and eventually overlap. At longer times, dendrites appear to extrude from the particle-like layer.

The nuclei density, $N(nuclei/cm^2)$, was determined at each time and plotted in Figure 6.4. In this case, the cm^2 term in the denominator refers to the superficial area over which the nuclei were counted. This results in the calculation of a current density (mA/cm^2) when using the Equation 6.7. The SEM images were also used to determine the average diameter of the nuclei at each point. Using the area for a hemisphere, this will give the average area/nuclei required in Equation 6.7.

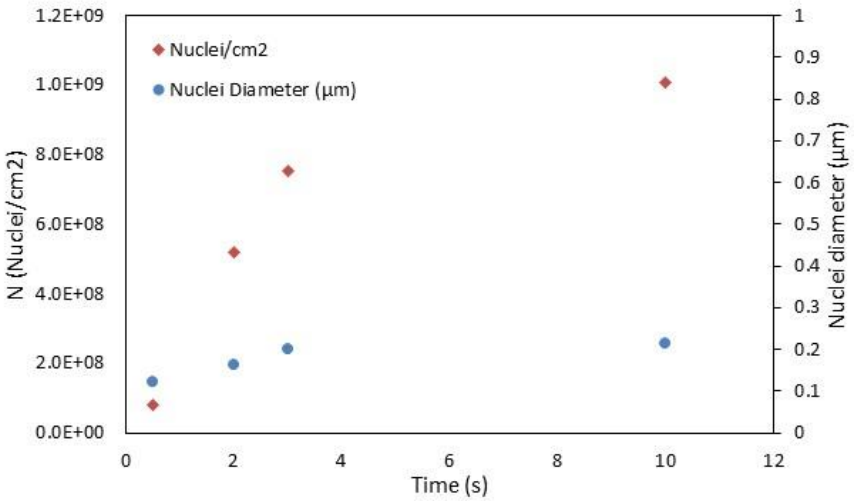

Figure 6.4: Nuclei density and diameter as a function of time in 1 M Li^+ EC:DMC.

The nuclei in Figure 6.3 have a hemispherical shape and a high contact angle with the stainless steel surface. The same contact angle and nuclei shape were observed when the deposition was carried out on a section of freshly cleaved lithium foil indicating that the shape of the deposit was not specific to stainless steel. Deposition on a foreign surface can sometimes lead to different morphologies because of a higher overpotential associated with the surface. In this case, the deposit morphologies are likely similar because SEI formation prevents lattice match when plating lithium on a Li substrate, even when the substrate is freshly cleaved.

The experimental current-time plot shown in the inset in Figure 6.5 shows the current due to double layer formation, followed by the rise in current to a steady value. The general shape corresponds to the theoretical one outlined in Figure 6.1 with several deviations. First, the timescale associated with double-layer formation in Figure 6.5 is longer than expected. The current does not drop after the initial current spike and does not rise almost a full second after the potential is applied. The double layer capacitance in organic electrolytes has been measured at ~25 µF, which should result in double layer

formation in ~30 ms[92]. In our case, the initial current spike also includes lithium intercalation into surface oxides. A small, generally insignificant peak can be seen at 0.5 V vs. Li/Li$^+$ in a cyclic voltammetry scan that contributes to the current at short times. These events delay the nucleation and deposition of lithium and cause the current plateau between double layer formation and the expected current rise. A second observation is that the current at long times in Figure 6.2 levels off due to the onset of overlapping nuclei and their diffusion layers. When nuclei begin to overlap, the true surface area does not grow as rapidly with time, as when nuclei are forming. The leveling off of the current in Figure 6.5 is not due to overlapping nuclei, as shown by sparse distribution of nuclei in Figure 6.3.

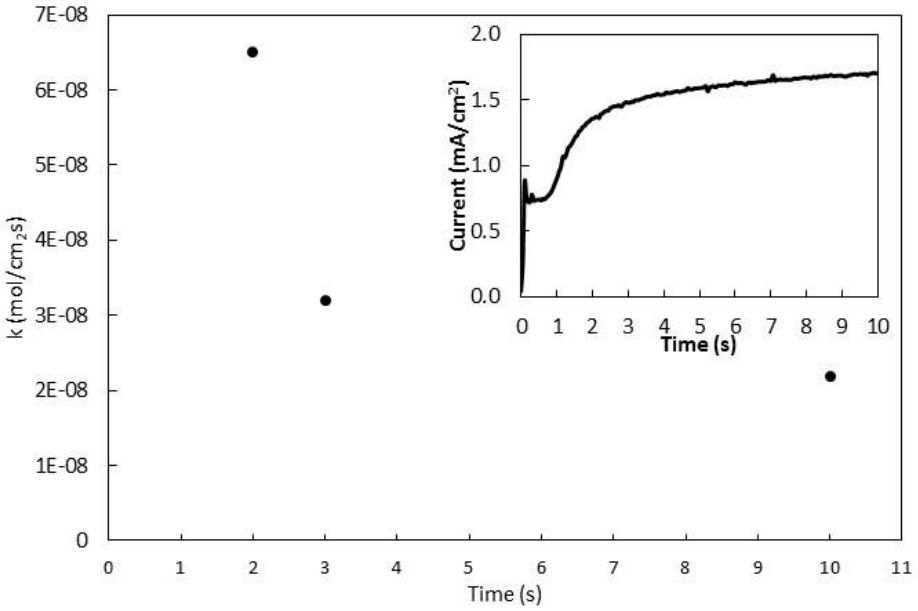

Figure 6.5: Deposition rate, *k*, assuming hemispheric growth. Inset: Current-time transient for polarization to -150 mV in 1M Li$^+$ EC:DMC. The current is measured in mA per superficial area.

The active area deposition rate, *k,* can be solved for at specific times by using the observed nuclei density and diameter (Figure 6.4) and the measured current density (Figure 6.5 inset) in Equation 6.7. The resulting active area specific rate, *k*, indicates that the growth rate decreases with time. This is a departure from the ideal geometry based model because the rate, *k*, should be a constant with time. The decrease in the local deposition rate observed here is consistent with the inhibiting effect of an SEI layer forming on freshly deposited lithium. While the nuclei are able to grow unencumbered at the very beginning, an SEI layer starts to form immediately. As each nuclei continues to grow, the SEI layer must be stretched and/or broken to accommodate the growing surface area. This adds additional resistance to nuclei growth, slowing the rate over time, as shown in Figure 6.6.

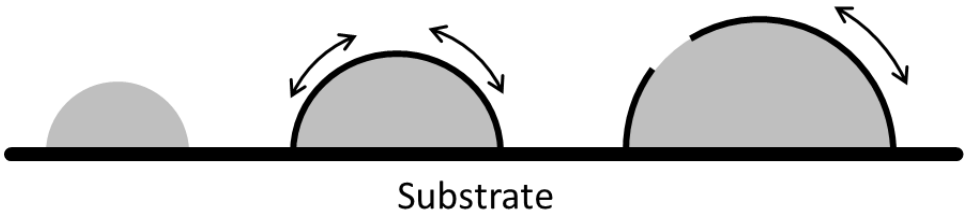

Figure 6.6: The SEI stretches and breaks as the nuclei grow, resulting in a decreasing deposition rate at constant over-potential.

Another observation from this study is that dendrites are not formed at the time of lithium nucleation in the EC:DMC system. The deposit remained mostly dendrite free until ~5000 s when dendrites seemed to extrude from the deposit. Several dendrites had grooves along their length that further suggest extrusion. Dendrites with a bulged head and narrow trunk were also observed. The latter shape corresponds to the model previously proposed by Yamaki et al. The model is based on an interplay between

surface tension and creep strength[34]. When surface tension and creep strength are balanced, a straight-walled whisker is extruded. When surface tension is greater than creep strength, the system is unstable and the dendrites form with a bulbous head, like the ones seen in our experiments. The model predicts that the head would eventually pinch off. Although this was not directly observed, it would be difficult to see this effect since the pinched-off head would have already left the deposit surface.

The same nucleation experiment was conducted in the N_{1114}-TFSI electrolyte and yielded very different results. In the EC:DMC electrolyte, dendrites did not appear at nucleation and formed much later in the bulk growth process. The same -150 mV over-potential in the ionic liquid system created dendrites immediately after nucleation. Figure 6.7 shows SEM images of the lithium deposit from N_{1114}-TFSI at -150 mV. Because of the lower conductivity, deposition in N_{1114}-TFSI is slower than that in EC:DMC, resulting in a longer timescale. Small circular nuclei 100-200 nm in diameter initially appeared on the surface, but instead of growing with an equally expanding radius, the radius stayed almost constant and cylinders form, eventually growing into dendrites. Dendrites do thicken over time, but at a much slower rate than the lengthwise growth.

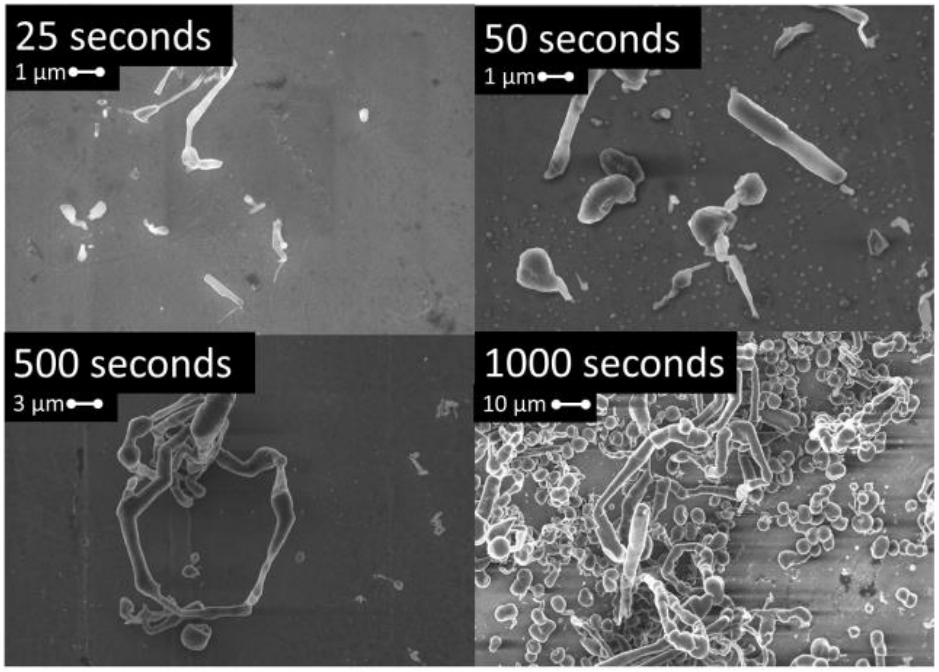

Figure 6.7: SEM images of deposits from 1M Li^+ N_{1114}-TFSI. Nuclei are dendritic immediately upon nucleation. Growth is isolated due to the dendritic shape.

Tracking the size of the individual nuclei with deposition time in the N_{1114}-TFSI electrolyte showed that nuclei growth was not uniform with time. SEM analysis showed that at 50 s, the larger nuclei were micrometers in size, however, a significant number of nanometer sized nuclei were present that did not grow in size. A similar observation was made at 500 s. When only the larger, growing nuclei were counted, a decreasing trend in terms of number of growing nuclei occurred with time, as shown in Figure 6.8. The dashed, upper curve in Figure 6.8 shows the total number of nuclei increasing with time, while the dotted line shows a decreasing population of growing nuclei. Thus the deposition current becomes restricted to fewer nuclei driving up the local current density.

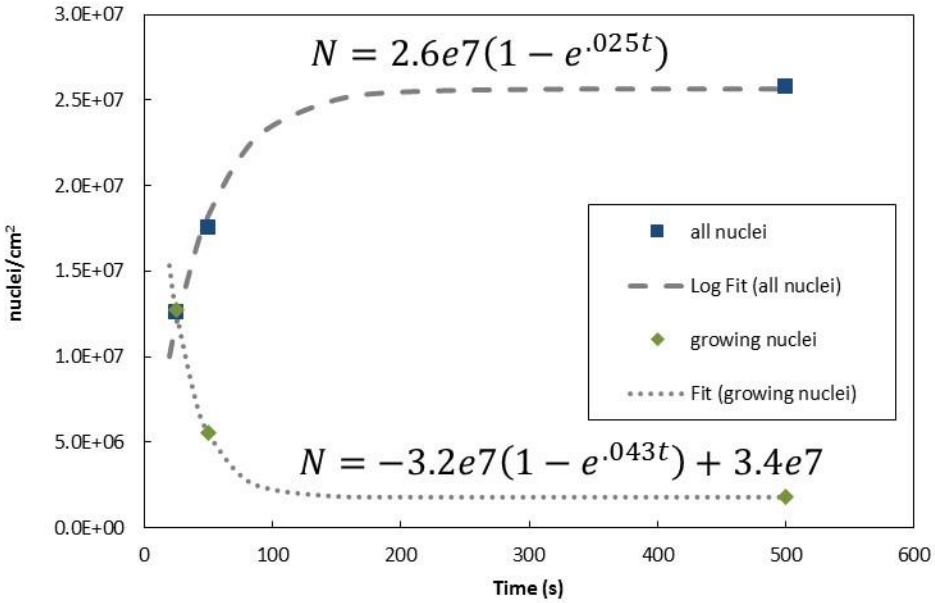

Figure 6.8: Nuclei appearance as a function of time in 1M Li^+ N_{1114}-TFSI. White the total number of nuclei increases, only a decreasing number of them continue to grow and contribute to the measured current.

The hemispheric geometry used for the EC:DMC case is not valid for the dendritic case because the dendrite growth is a one-dimensional process, rather than three dimensional. The nuclei geometry observed in the ionic liquid electrolyte was simplified to that of a cylinder with a constant 0.5 µm diameter reflecting the size of the observed dendrites. The active area for deposition is thus a constant area circle representing the trip of a dendrite. The current going to the creation of smaller non-growing nuclei was negligible, so the equation used for *N*, the number of nuclei over time, was that of the growing nuclei in Figure 6.8. An illustration of this modified equation is shown in Figure 6.9. The resulting rate *k*, is shown in Figure 6.10.

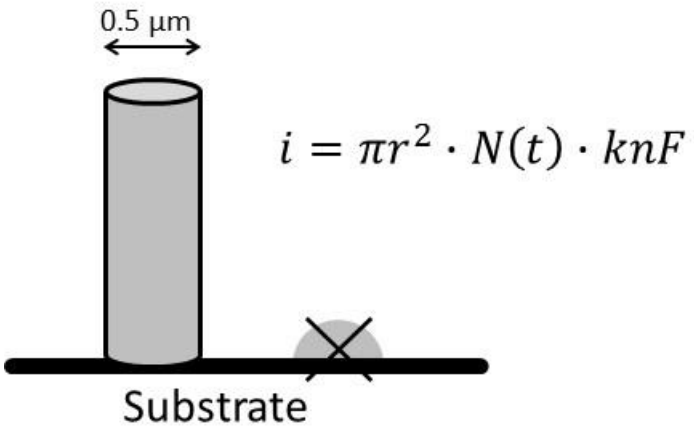

Figure 6.9: Current equation based on tip-only growth of dendrites.

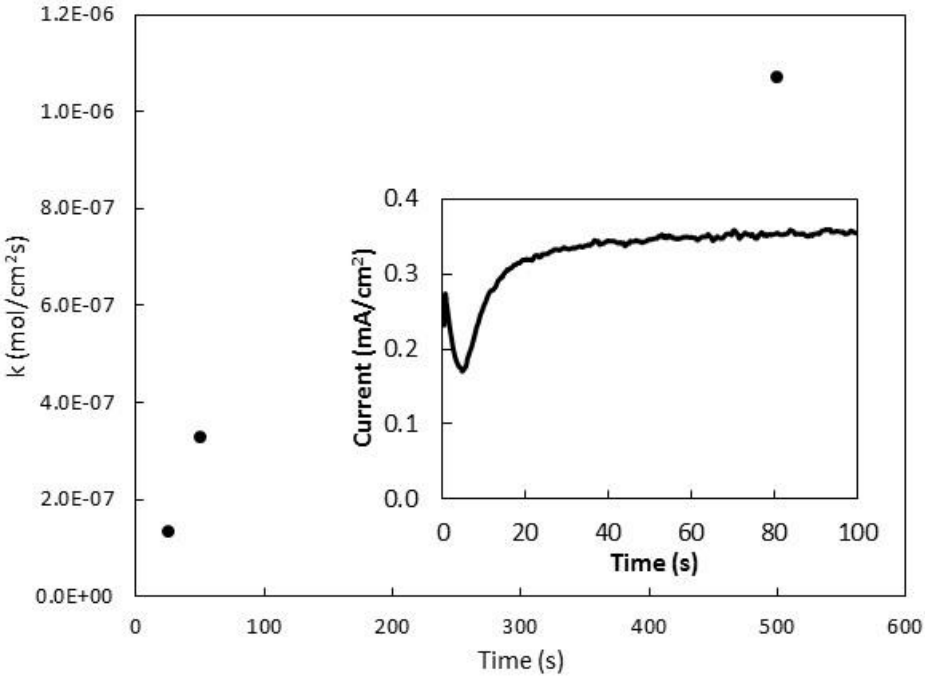

Figure 6.10: Deposition rate, *k*, solved for by assuming a cylindrical geometry where only the tip is electrochemically active. Inset: Current-time transient for polarization to -150 mV in 1M Li^+ N_{1114}-TFSI. The current is measured in mA per substrate area.

If only the decreasing population of nuclei is taken into account from Figure 6.8, the rate of growth of the large nuclei can be solved for based on one-dimensional cylindrical growth. The increasing trend for the rate *k* in Figure 6.10 shows that the inhibition behavior of the SEI seen in the EC:DMC electrolyte is not present in the dendritic growth from the ionic liquid electrolyte. The negligible growth on the dendrite sidewalls observed indicates that for the same volume of material, a smaller electrochemically active area is available. This leads to a high local current density and faster growth rate, *k*, on the active areas.

The rate k, which is proportional to the local current density, increases with time even through the overpotential is constant. This means that the timescale for lithium deposition outstrips that of SEI formation. The high local current density at the dendrite tips outpaces the SEI formation on some dendrites while adjacent locations are inhibited. This leads to an unstable condition where some nuclei grow faster because the SEI on their electrochemically active areas is thin or unformed. Once a dendrite starts developing an SEI at the tip, growth immediately slows relative to its neighbors. Because of the additional resistance, growth stops altogether soon after the SEI develops. Meanwhile, the neighboring dendrites see an increased current density due to the decrease in active surface area resulting in even faster growth. In this way, only a few large dendrites and many smaller stunted ones are observed. Because the deposition rate increases with time, the effect of the SEI is mitigated and the deposition rate rises.

It was previously shown that a lithium/sodium co-deposition can mitigate dendrite growth[91]. To further investigate how this occurs, a nucleation-rate study was conducted in a 1 M Li^+/0.1 M Na^+ N_{1114}-TFSI electrolyte. Figure 6.11 shows SEM images of the stainless steel surface as a function of time. It can be seen that the co-deposition of sodium acts to inhibit dendritic growth from the initial point of deposition, by comparison

of Figure 6.7 (no sodium) to Figure 6.11 (with sodium). Instead of forming cylindrical nuclei (Figure 6.7) as in the lithium-only electrolyte, the lithium/sodium electrolyte showed round and dimpled nuclei (Figure 6.10). The dimples are particularly evident in the 1000 s image of Figure 6.11.

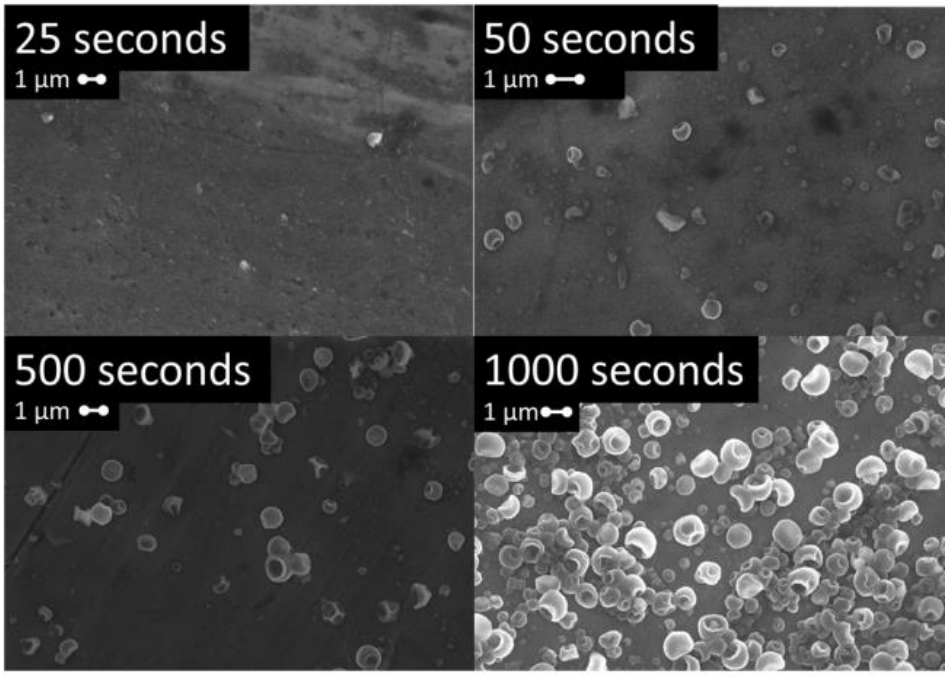

Figure 6.11: Deposit from 1 M Li^+/0.1 M Na^+ N_{1114}-TFSI appears round and dimpled instead of dendritic.

As in the EC:DMC case, the nuclei/substrate area and average diameter of those nuclei were counted as a function of time. The geometry of the deposit falls into the hemispherical category and the deposition rate *k*, can be solved for at each data point in the same manner as the EC:DMC electrolyte. The Figure 6.12 inset shows the current-time transient for 1 M Li^+/0.1 M Na^+ N_{1114}-TFSI and the corresponding rate *k* is shown in the main figure. A decreasing trend in *k*, similar to the EC:DMC electrolyte is observed. Because the area available for deposition is larger in the hemispherical geometry, the

local current density and rate k, are much lower than in the dendritic case. This results in a better formed SEI layer over time, instead of the runaway case for dendritic growth. The rate *k* decreases over time because stretching and breaking the SEI imposes an additional resistance for the deposition process.

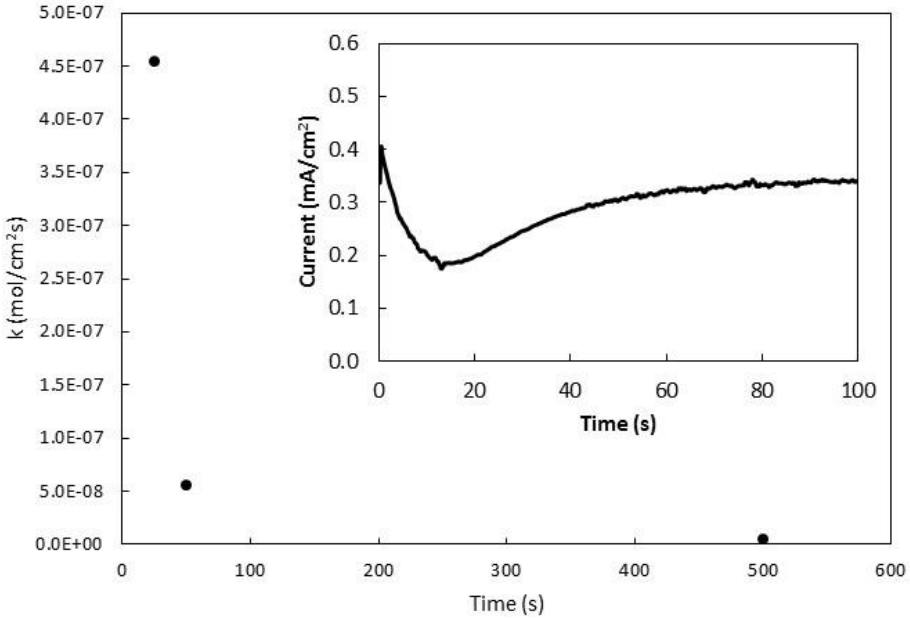

Figure 6.12: Rate *k*, for 1 M Li^+/0.1 M Na^+ N_{1114}-TFSI solved for assuming a hemispheric geometry. Inset: Current-time transient for polarization to -150 mV.

In order for lithium dendrites to grow in the cylindrical manner shown in Figure 6.7, the growth rate at the tip must be much higher than the growth rate of the sidewalls. Simple explanations such as the electrolyte resistance being lower at the tip than the base of the dendrite do not explain formation of dendrites because of the variety of experimental setups that produce the whiskers. Given the TEM data presented by Liu et al. confirming the crystallinity of lithium dendrites[32], the lithium deposition rate is crystal face dependent with some faces being more active for electrodeposition than the other

faces. It is possible that the dimpled morphology observed with the co-deposition of sodium results because sodium also deposits on the active lithium face. Sodium would act to inhibit the lithium growth rate because it is a foreign element and acts to block the progress of the growing dendrite formation. At the same time, lithium continues to deposit in other areas at the normal rate that would otherwise occur because the high current areas are slowed. This would result in a dimpled morphology (Figure 6.13).

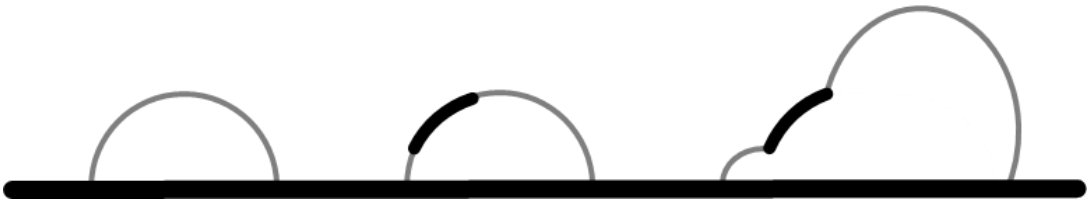

Figure 6.13: Illustration of potential mechanism for dendrite mitigation in the presence of sodium.

ToF-SIMS was used to analyze the location of the deposited sodium metal with respect to the lithium nuclei. An ion image of a deposit from the 1 M Li^+/0.1 M Na^+ N_{1114}-TFSI electrolyte is shown in Figure 6.14. Because of the large amount of Li in the SEI and on the surface, an ion map of Li^+ cannot distinguish clear bulk features. To observe only bulk Li, the Li_2^+ peak was used as a substitute. This peak represents a cluster of Li ions that can be released from the bulk and thus accurately shows bulk lithium only. The same could have been done with Na^+ however, the peak for Na_2^+ was weak and did not give a sharp image, thus the Na^+ peak was used. Individual lithium particles are observed on the substrate of the sample, as well as very localized sodium particles. It is clear that sodium was not deposited uniformly on the substrate but rather in very specific areas. This observation supports the theory that sodium was likely deposited on the active face of lithium, thus blocking dendrite growth.

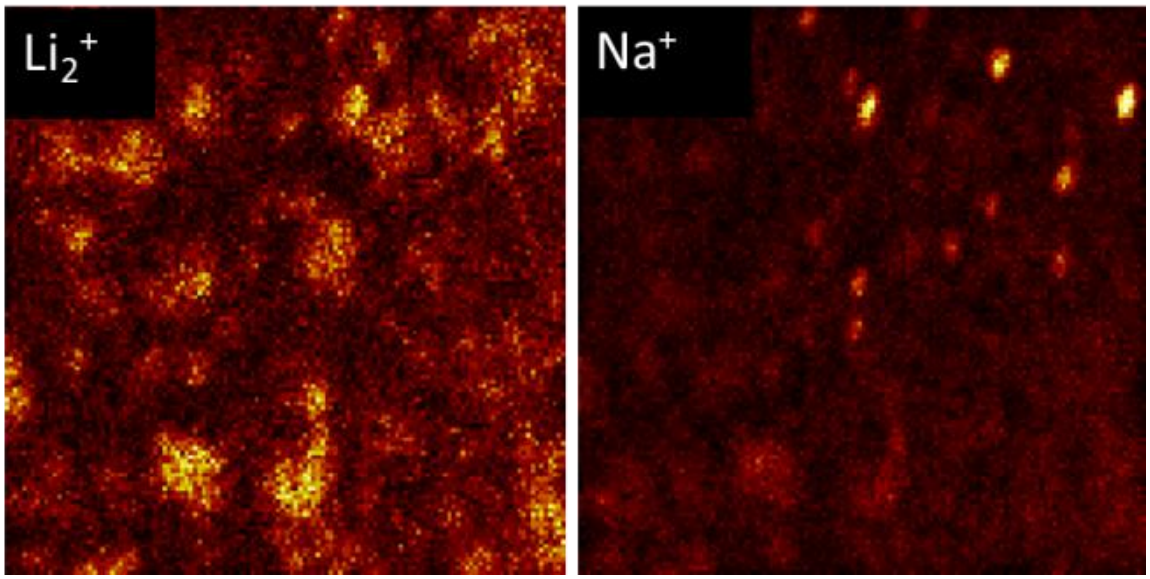

Figure 6.14: Element map from Tof-SIMS for deposit from a 1 M Li^+/0.1 M Na^+ N_{1114}-TFSI electrolyte.

Ex-situ, SEM images point to the existence of both extruded dendrite growth and tip-based dendrite growth. In-situ observations of dendrite growth were performed to better understand the progression of growth. Images of single dendrite growth were recorded as a function of time. A cell sandwiched between two glass slides, as described in the experimental section, was used to observe dendrites in an optical microscope. Dendrites grown from EC:DMC and N_{1114}-TFSI electrolytes were both on the order of micrometers in size and thus too small to observe in a light microscope. Lithium deposited from the imidazolium chloroaluminate electrolyte produced much larger dendrites, tens of μm in diameter, which could be observed with an optical microscope. Video footage was recorded at 5 mA/cm^2 applied current. Figure 6.15 shows frames from two separate dendrites whose growth was observed with time.

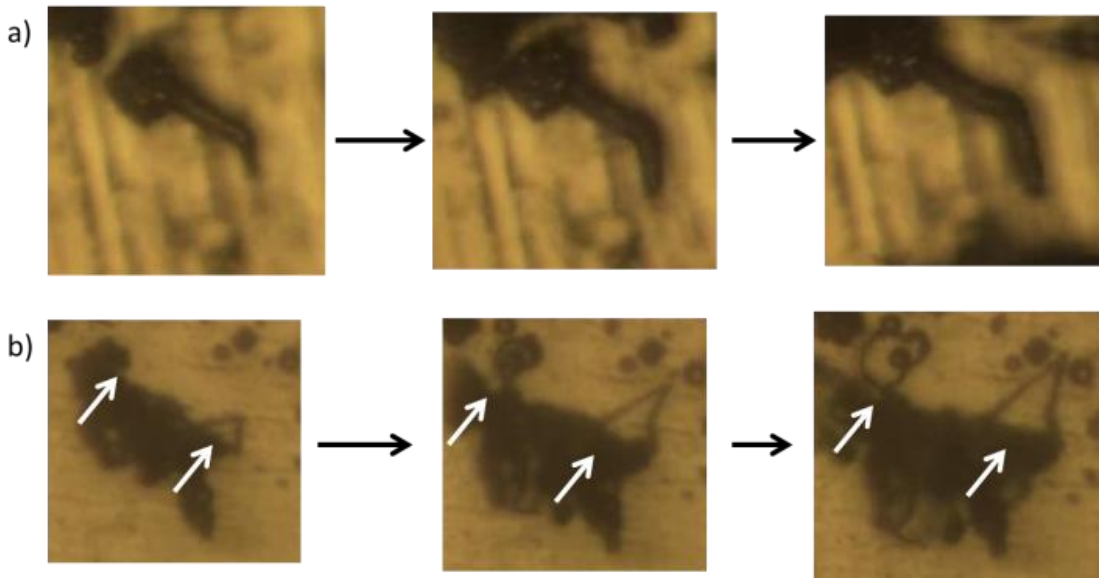

Figure 6.15: Optical microscope observations of individual dendrite growths in imidazolium chloroaluminate ionic liquid. a) Tip growth shown by a kinked dendrite and b) base growth of two loops by extrusion.

Figure 6.15a follows a dendrite that developed a kink. Using the kink as a reference point, we can clearly see dendrite growth progressing via the tip of the dendrite. The growth rate at the tip was far greater than the growth from on the sidewalls, suggesting that the crystal face at the tip was significantly more electrochemically active. This cannot be explained by mass transfer effects alone because once clear of the lithium lump at the base, the sidewalls around the tip are in a similar environment to the tip itself. One might expect a thickening at the tip due clearing the diffusion layer of the base lump, but this does not occur. The fact that the dendrite was straight before and after the kink further supports that the dendrite is crystalline in nature and the kink arose from a defect in the crystal. Figure 6.15b shows a different case where a lithium structure spawned a looped dendrite. In the first frame, two loops can be seen coming out of the main lithium structure. In subsequent frames, the loops become larger but no tip was visible to propagate the growth. The most reasonable explanation is that lithium was extruded out from the main structure.

6.5 Summary

We were able to definitively observe both tip-based and extrusion-based dendrite growth in-situ and ex-situ. Tip-based growth is an electrochemical process where the tip is an electrochemically active face that grows at a significantly faster rate than the sidewalls or base. Extrusion-based growth is not a direct electrochemical event, but rather occurs as a side-effect of pressure build-up as a result of lithium deposition under a strained SEI layer.

Sodium can play a crucial role in suppressing tip-based dendrite growth. When sodium is co-deposited with lithium, the two metals do not form an alloy. Instead, distinct areas of sodium are visible in the ToF-SIMS analysis. Considering the lack of dendrites when these sodium clusters are present, it is believed that lithium dendrites can grow because of increased electrochemical activity on a specific crystal face of lithium. Sodium acts to block the accelerated growth and resulting in a dimpled and dendrite-free morphology. Such a blocking effect could also be the reason why no dendrites are seen in EC:DMC or with certain additives such as HF and VC[25,38,39].

No tip-growth dendrites were observed in this set of experiments from EC:DMC while many were observed in N_{1114}-TFSI. The SEI formed in these electrolytes is chemically very different. The SEI formed in N_{1114}-TFSI consists of mainly LiF[93], while the EC:DMC system forms a layer of EC decomposition products such as alkoxides[76]. The physical properties of these layers will also be different. It is probable that alkoxides and other additives can have a similar blocking affect as the sodium co-deposit observed here or that the SEI is simply robust enough to suppress the tendency for high-rate dendritic growth. Sodium is advantageous over the other electrolyte decomposition materials

because it can double as active material in the cell. Sodium can be oxidized along with the lithium anode and thus the charge stored is not lost. Sodium can then be re-deposited in the next cycle without material waste whereas fresh electrolyte would have to be decomposed on the new active areas in each cycle.

By using the geometry of the nuclei at short times, it was possible to calculate a rate *k*, which is directly proportional to the local current density seen by the nuclei. Since a constant potential was applied, this rate should also be a constant with time, but calculations based on the overall current density as well as number and size of nuclei show that this rate varies in magnitude and trend given the deposit morphology and electrolyte. The cause of this variation is an interplay between the geometry of the deposit and the rate at which the SEI layer forms. Depending on the rate *k*, deposition can either outstrip SEI formation (dendritic growth) or be hampered by it (granular growth). Thus, the trends seen in the calculated rate allow us to draw several conclusions about the effect of the SEI on the local current density. When a granular, hemispheric, geometry is observed at constant potential (EC:DMC and Li/Na N_{1114}-TFSI), the rate dropped from an initially high value because the SEI imposed additional resistance as it fully formed. In the dendritic case, lithium deposition occurred over a limited active area. The high local current density, and rate *k*, resulted in lithium deposition that outstripped the SEI formation, so an initial increasing rate was observed.

If the SEI is formed by a reaction of freshly deposited lithium metal with the electrolyte, the thickness of the SEI will be inversely related to the rate, *k*. A thicker SEI will provide increased resistance to lithium-ions depositing at the surface because ions must diffuse through the SEI. The decreasing deposition rate calculated from these experiments could be further used to determine a thickness of the SEI on lithium with time. Under the assumption that the both hemispheric cases become limited by the

diffusion of lithium ions through the SEI layer, the diffusivity through the SEI, along with the rate *k* (also the flux, mol/cm^{2}s) can be used to determine the thickness of the SEI with time.

While this work looked at early deposits only, there are consequences for the thicker deposits that might be used in the lithium metal battery. The deposition of contiguous films of metal with excellent coulombic efficiency upon cycling are highly desired but the SEI plays a large role in preventing nuclei from growing together in long-time experiments. Despite non-dendritic results with sodium co-deposition, the SEI film formed on lithium still presents a major hurdle for the lithium-metal anode.

7. Effect of Alkali and Alkaline Earth Metal Salts on Lithium Metal Anodes

7.1 Objective

In ionic liquid systems, the suppression of dendritic growth of lithium has been studied by co-depositing a second metal with lithium from bis(trifluoromethanesulfonyl)imide (TFSI) and chloroaluminate ionic liquid electrolytes[30,91]. A non-dendritic, sphere-like lithium morphology was achieved through the co-deposition sodium with lithium. The remaining alkali TFSI salts have been synthesized and their reduction potentials characterized, opening the door for their study in conjunction with lithium. Potassium, rubidium, and cesium can be reversibly deposited at potentials negative of lithium deposition in TFSI-based electrolytes, making co-deposition feasible[94].

The group 2 alkaline earth metals, of which magnesium has been considered for battery applications, are of interest. Magnesium is more difficult to deposit than lithium because the surface films formed on magnesium are more insulating and are not as ion conducting as their lithium counterparts[11]. In addition, reduction of a doubly charged cation generally involves a more complex series of reactions. Magnesium deposition has been demonstrated from Grignard based solutions and some ionic liquids electrolytes[95–99]. The remaining alkaline earth metals, calcium, strontium and barium, have not been studied alone or as additives in lithium deposition. Calcium, strontium, and barium are used in phosphate and carbonate coatings for biocompatibility, but these coatings are formed by electrochemically assisted deposition, not a direct reduction of the metal. Nitrates are electrochemically reduced lowering the pH at the substrate, which causes

phosphates and carbonates of these metals to precipitate[100–103]. While the clear goal for the alkali metals is a co-deposit, the effect of alkaline earth metal is less clear.

7.2 Results and Discussion

The added cation can have one of several affects including co-depositing, changing the electrolyte conductivity, and changing the electrode double layer. When the Li-TFSI dissolves in N_{1114}-TFSI, a clear, viscous electrolyte is formed. A constant potential deposition yields a deposit, shown in Figure 7.1, where the surface is dominated by dendrites.

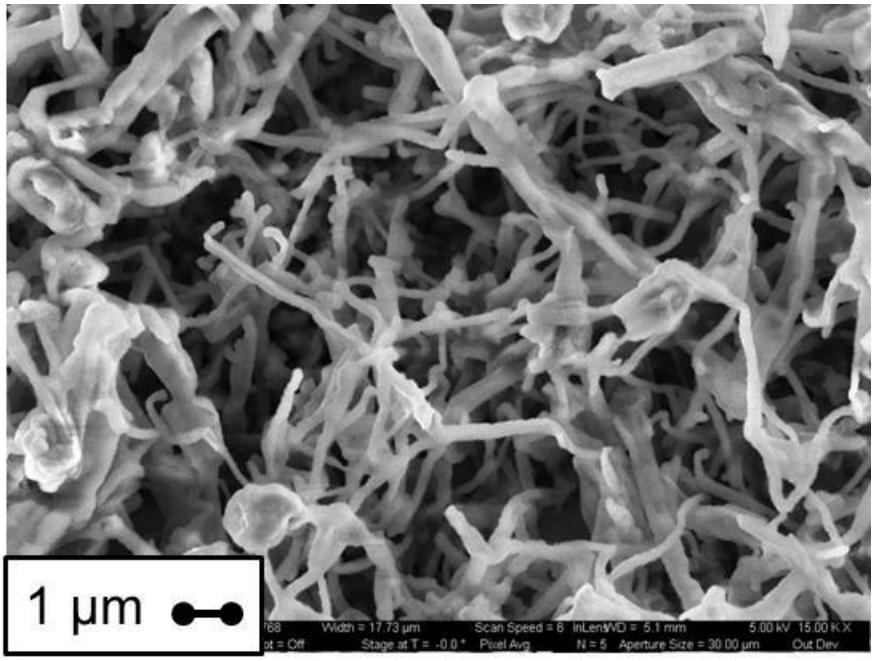

Figure 7.1: Lithium deposited from a 1 M Li^+ electrolyte at -0.3 V for 500 s.

The group 1 alkali metals ions investigated were sodium, potassium, rubidium and cesium. Previously, sodium ions were shown to be co-deposited with lithium forming a non-dendritic, sphere-like deposit as shown in chapters 3 and 4[30,91]. The reduction potential of the remaining metal ions were experimentally measured in pyrrollidinium TFSI ionic liquid by Wibowo et al.[94]. The pyrrollidinium TFSI ionic liquid is similar to the quaternary ammonium ionic liquid used in this work so it is reasonable to assume that the potentials will follow the same trend. While sodium reduces 0.184 V positive of lithium, the remaining alkali metals reduce at potential negative of lithium, even though their standard potentials are positive of lithium. Potassium reduces at -0.109 V vs. Li/Li^+, rubidium at -0.117 V, and cesium at -0.122 V based on work by Wibowo et al. in pyrrolidinium-TFSI. To observe a co-deposit of lithium with these three metals, potentials more negative than these values, corrected for concentration by the Nernst equation, are necessary assuming underpotential deposition does not occur. Each alkali metal was first tested in a 0.1 M solution in N_{1114}-TFSI without lithium ions being present. The voltammetry with 0.1 M Na^+ is shown in Figure 7.2 while voltammetry with 0.1 M K^+, Rb^+, and Cs^+ is shown in Figure 7.3. With the exception of lithium, sodium exhibited the most defined redox behavior with a distinct reduction peak starting at 0.09 V vs. Li/Li^+. On the reverse scan, Na oxidation began at 0.16 V, which is consistent with the results from Wibowo et al.[94]. The overpotential observed is likely due to the nucleation effect of plating a metal on a foreign surface and has been observed previously [62,66,94].

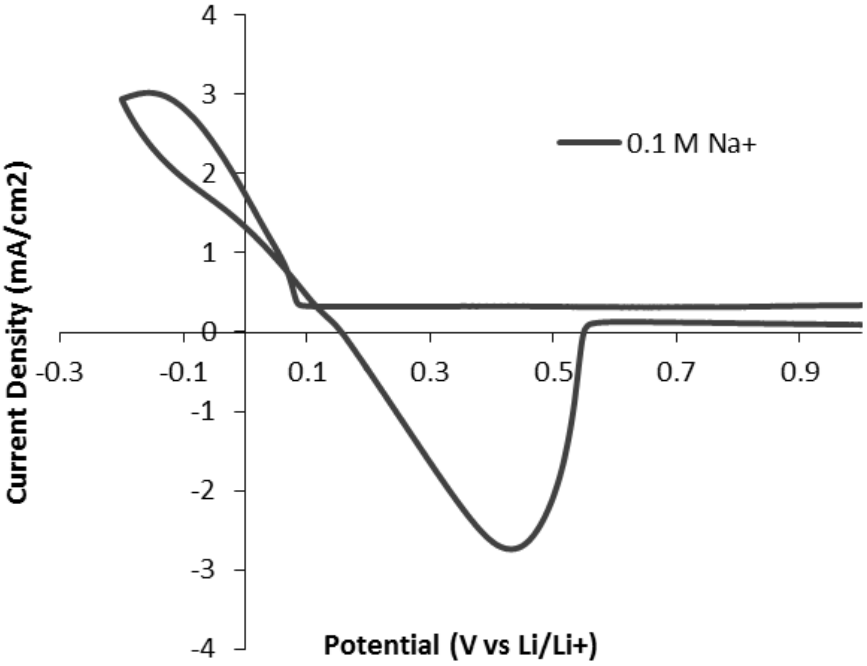

Figure 7.2: CV of 0.1 M Na^+ electrolyte shows reduction starting at 0.09 V vs. Li/Li^+.

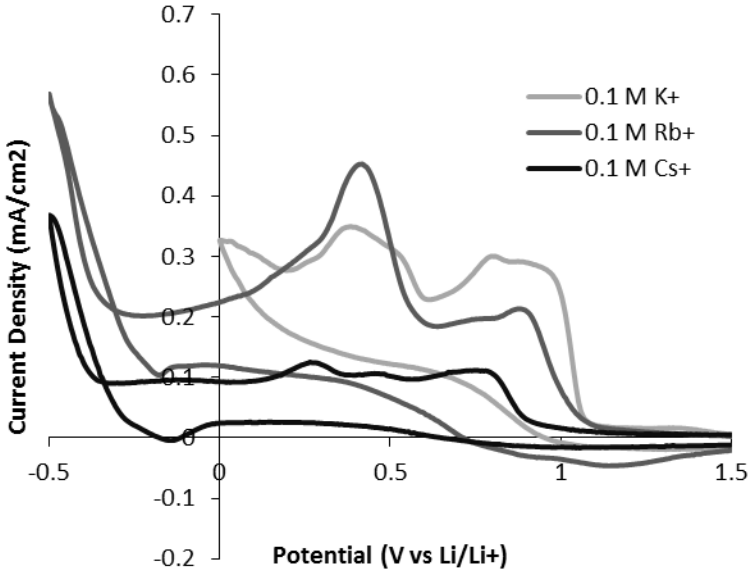

Figure 7.3: CV of 0.1 M potassium, cesium, and rubidium electrolytes.

In contrast, no reduction of potassium was observed on the stainless steel electrodes, as seen in Figure 7.3. Two peaks at 0.9 V and 0.4 V were observed on the first cycle but not observed on subsequent cycles, suggesting a one-time surface modification to the stainless steel, rather than an irreversible deposit. While reduction and oxidation of potassium from TFSI-based ionic liquids has been observed on nickel and tungsten electrodes [63,94], another attempt from chloroaluminate ionic liquid failed on tungsten but succeeded on mercury[59]. Based on the different results for potassium deposition, it appears that potassium is more surface dependent than the other metal ions.

Wibowo et al. reported that rubidium and cesium were reduced near the potential limit of the ionic liquid used here, which is ca. -0.35 V vs. Li/Li^{+}[94]. The 0.1 M Cs^{+} electrolyte displayed several small reduction peaks between 0.2 V and 1.0 V. When a sample was held at 0.5 V, well within the range of these peaks, SEM and EDX showed sparse nanometer-sized cesium-rich particles on the surface but the CV shows no electrochemical evidence that this material can be stripped from the substrate. Subsequent CV cycles show that these peaks decreased in height, but did not disappear altogether. This indicates that they are likely caused by reactions with the pristine surface, rather than bulk processes. A small oxidation peak was observed at and -0.29 V for cesium. To isolate this peak, a sample was held at -0.4 V for 500 s. A porous deposit with high cesium content was observed. This indicates that the small oxidation peak at -0.29 V is metallic cesium. The peak is small because the potential at which cesium is deposited also causes electrolyte decomposition as a competing reaction. In addition, some cesium could have been lost to reaction with the electrolyte after the metal is formed.

The CV of 0.1 M Rb^+ shows a similar oxidation peak to cesium at -0.25 V. A sample held at -0.4 V for 500 s showed a roughly textured rubidium-rich deposit indicating that this anodic peak is due to the oxidation of metallic rubidium. The reduction of Rb^+ is likely also too close to the decomposition potential for the electrolyte to observe a deposit with high coulombic efficiency for reduction and re-oxidation. The peaks at 1 V and 0 V could not be specifically identified, but decreased in height with each CV cycle. This indicates that they are due to one-time surface reactions, rather than bulk processes.

The electrolytes containing 0.1 M concentration of K^+, Cs^+, Rb^+ described above were made 1.0 M Li^+, in addition to the 0.1 M alkali metal. Figure 7.4 shows the cyclic voltammograms recorded for these new electrolytes, which now contain 1 M Li^+ and 0.1 M alkali metal ions. Each electrolyte showed peaks for lithium deposition and stripping. The overpotential for the Li redox process remained -0.075 V regardless of which metal was added indicating a minimal effect of the foreign metal ions on the Li/Li^+ couple. Rather, the addition of the second metal ion affected the peaks between 0 V and 1 V, which are associated with surface, rather than bulk, processes. On stainless steel, lithium showed two peaks at 1.3 V and 0.4 V on the forward scan, prior to the reduction of lithium ions to metallic lithium. The first peak at 1.3 V is an irreversible surface process that only appears on the first cycle. It is likely an initial surface film that forms on the substrate involving Li^+ ions, as the peak does not appear for the neat ionic liquid. By reversing the scan direction at 0 V, prior to Li^+ reduction, the second peak at 0.4 V can be paired with the peak at 1.3 V on the reverse scan. This set of peaks remained constant over multiple cycles and is likely the intercalation/de-intercalation of lithium into the surface oxide present on stainless steel. Allowing the potential scan to go negative of 0 V vs. Li/Li^+ shows that lithium reduction begins at -0.075 V and the re-oxidation peak

appears on the reverse scan starting at 0 V. The coulombic efficiency associated with lithium ion reduction and re-oxidation is 65%, which is lower than what can be achieved in an actual battery because deposition on a foreign surface, here stainless steel, affects the charge passed on each cycle. In a commercial cell, a shallow cycling method could be used to avoid this problem [93,104]. In addition, the background current associated with the surface oxide intercalation lowers the calculated efficiency.

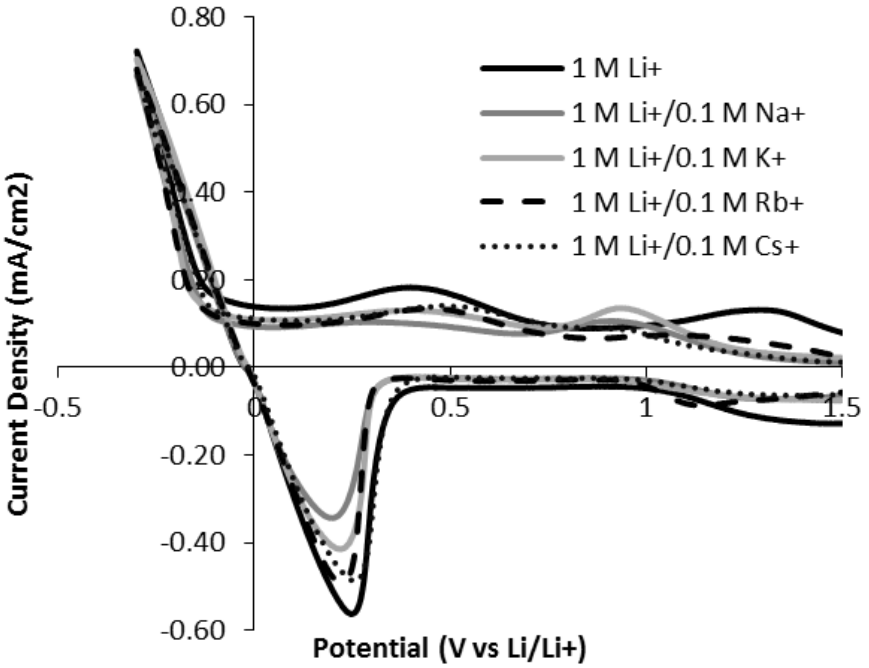

Figure 7.4: Cyclic voltammograms of lithium electrolytes with 0.1 M alkali metal ions.

The addition of sodium ions to the lithium ion containing electrolyte shifted the first irreversible peak at 1.3 V to 0.9 V. As described above, this peak did not appear on the second cycle pointing to a one-time surface modification. From previous work, it has been shown that lithium and sodium can be co-deposited to form a non-dendritic deposit [30,91]. The lithium/sodium co-deposit consisted of many spheres with at least one

indentation on the surface. This morphology is shown in Figure 7.5a and was studied in detail in previous chapters. The coulombic efficiency for the deposition and re-oxidation of the lithium/sodium system was calculated to be 44%. While it is possible for the absence of dendrites to lead to an increase in the coulombic efficiency, the coulombic efficiency of sodium from the CV results was only 41%. This relatively poor redox efficiency for sodium appears to be the cause of the lower coulombic efficiency for the lithium/sodium system.

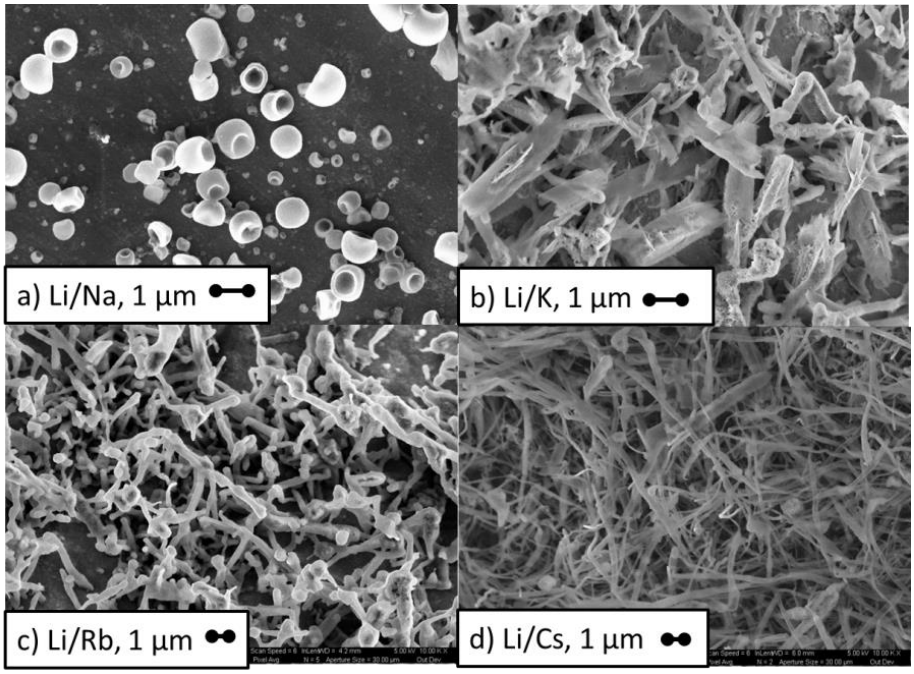

Figure 7.5: SEM images of lithium deposits from 1 M Li^+ electrolyte with 0.1 M alkali metal ions. Substrate was held at a) -0.15 V, b) -0.3 V, c) -0.4 V, and d) -0.4 V for 500 s. Potentials were chosen based on the different overpotentials for each electrolyte and the ability to deposit the alkali metal ion at that potential.

No metal was electrodeposited from the potassium-only electrolyte, thus no co-deposit of lithium and potassium was expected. A CV of the 1.0 M Li^+/0.1 M K^+

electrolyte showed two reduction peaks prior to lithium ion reduction, followed by lithium re-oxidation on the reverse scan. The surface related peak that appears at 1.3 V in the lithium-only electrolyte has again been shifted to 0.9 V, as in the lithium/sodium electrolyte. This peak appeared only on the first cycle, indicating an initial surface reaction, rather than a bulk process. The peaks related to lithium intercalation into the surface oxide, at 0.4 V on the forward scan and 1.3 V on the reverse scan, were not affected by the addition of potassium. The coulombic efficiency for lithium reduction and re-oxidation was 51%. The lithium/potassium deposit exhibited a flake-like morphology, as shown in Figure 7.5b, different from the long, thin dendrites observed for a lithium-only electrolyte (Figure 7.1). The flakes were 1 μm wide and 2-3 μm long. The edges of the larger flakes and smaller platelets give the deposit a crystalline appearance. Individual flakes look detached from the substrate as well as each other and exhibited the same high surface area that is detrimental to cycling efficiency.

The potential scans changed little when either Rb^+ or Cs^+ (0.1 M) were included to the 1.0 M Li^+ electrolyte. The coulombic efficiency for the Rb^+ and Cs^+ containing electrolytes was 57% and 61%, respectively. The characteristic peaks seen in lithium-only electrolytes remained unchanged. Cesium and rubidium are electrodeposited at potentials negative of lithium, as shown in Figure 7.3. The dendritic lithium deposit morphology in the presence of Rb^+ or Cs^+ was unchanged even when material was deposited at -0.4 V, a potential where the metal ions are reduced from their individual electrolytes. Figure 7.5c and 7.5d show that dendrites from the lithium/rubidium and lithium/cesium electrolytes have a diameter of 0.2 to 0.5 μm, similar to the dendrites of a lithium-only deposit shown in Figure 7.1. The dendrites were entangled, constant-diameter needles that had a high surface area and poor adhesion to the stainless steel

substrate. The EDX results showed no cesium or rubidium present in the electrodeposit, thus only the Li^+ and IL reduction occurred.

The results from the addition of 0.1 M alkali metal to the 1 M Li^+ electrolyte suggest that in order to prevent dendritic growth, the alkali metal ion must be co-deposited. In this IL, co-deposition was only possible with sodium because the reduction potentials for cesium and rubidium were negative of the decomposition potential of the IL.

The group 2 alkaline earth metal ions, Mg^{2+}, Ca^{2+}, Sr^{2+} and Ba^{2+}, were added to the 1 M Li^+ electrolyte to examine their effect on the form of the lithium electrodeposit. The higher charge density of the divalent ions increased the viscosity of the IL. Electrolytes containing 0.1 M Mg^{2+}, Ca^{2+}, Sr^{2+}, or Ba^{2+} yielded milky-white solutions compared to the clear solutions formed with the alkali metal salts. CVs for each of these electrolytes are shown in Figure 7.6.

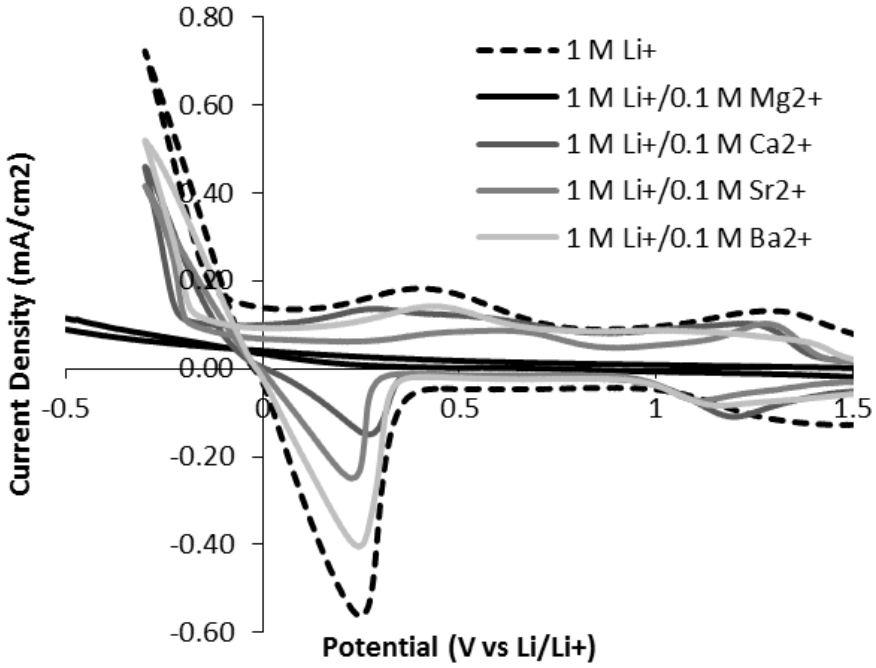

Figure 7.6: Cyclic voltammograms of lithium electrolytes with 0.1 M alkaline earth metal ions.

Because of the interest in a magnesium metal battery, a 0.1 M Mg^{2+} electrolyte was tested for Mg deposition, however, no CV peaks or deposit were observed. Although magnesium metal does not deposit from the Mg-only electrolyte, Mg^{2+} had a dramatic influence on the form of the lithium deposit. The magnesium salt also appeared to increase the voltage stability window of the IL. As shown in Figure 7.6, a CV of a 1 M Li^{+}/0.1 M Mg^{2+} electrolyte showed no sharp current rise at -0.35 V, where the ionic liquid is usually reduced. Instead, a gradual rise in current was observed with a much reduced slope was observed. The CV for the 1 M Li^{+}/0.1 M Mg^{2+} electrolyte (Figure 7.6) showed no peaks until the gradual rise at -0.4 V, which was due to electrolyte reduction. None of the above-mentioned peaks associated with lithium appeared in the scan. Lithium ion reduction was observed at a lower 0.05 M Mg^{2+} followed by re-oxidation, however, the overpotential for lithium ion reduction was -0.4 V, which also led to electrolyte reduction. The coulombic efficiency, based on the reduction and oxidation peaks, was only 17%

because of the extreme value of the potential required to reduce lithium ions. The electrodeposit had the appearance of spheres covered by a web-like material, as shown in Figure 7.7. The webbing was shown to be carbonaceous by EDX analysis, and most likely due to products from reduction of the electrolyte. The spheres mostly disappeared after re-oxidation of the lithium at 1 V, showing that they were indeed lithium metal.

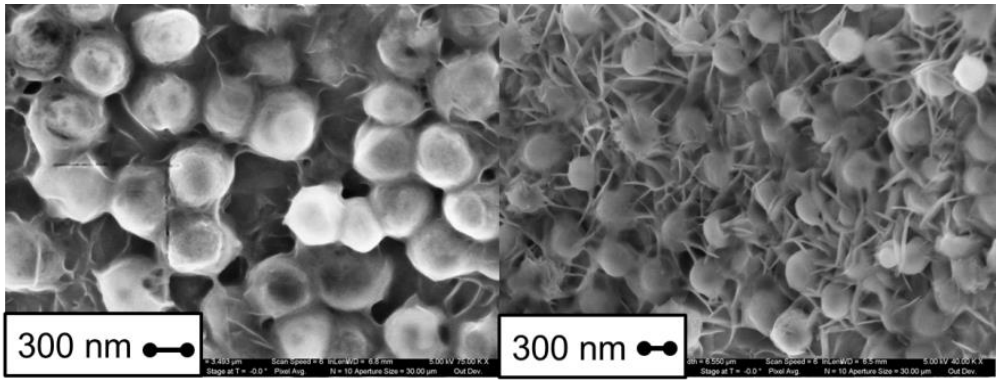

Figure 7.7: Lithium deposit from a 1 M Li^+/0.05 M Mg^{2+} electrolyte at -0.5 V for 500 s.

The addition of Ca-$TFSI_2$ to a 1 M Li^+ electrolyte did not suppress lithium reduction and re-oxidation currents to the same extent as magnesium salt. The current density observed with 1 M Li^+/0.1 M Ca^{2+} in the electrolyte was lower than for the lithium-only electrolyte. The CV shown in Figure 7.6 shows a clear lithium reduction and re-oxidation current in the Ca^{2+} containing electrolyte, although the overpotential for Li^+ reduction increased to 0.2 V (the reduction current started at -0.2 V vs. Li/Li^+) compared with the lithium-only electrolyte, where the overpotential was 0.08 V vs. Li/Li^+. The lithium metal oxidation peak was smaller than the reduction peak, yielding a coulombic efficiency 31% for the 1 M Li^+/0.1 M Ca^{2+} electrolyte. The sloping onset of the oxidation peak also indicates an overpotential associated with the oxidation. Lithium was deposited from

electrolytes with a Ca^{2+} concentrations of 0.05 M and 0.1 M. The lithium concentration was held constant at 1 M Li^{+} (Figure 7.8) in both cases. Deposits from the 0.05 M Ca^{2+}/1 M Li^{+} electrolyte had a tendency to deposit dendritically, however, a majority of the particles were dimpled spheres, similar to the sodium case. The deposit was fully non-dendritic when the electrolyte was changed to 1 M Li^{+}/0.1 M Ca^{2+}. Despite the similar appearance to the lithium/sodium deposit, this deposit, originating from the lithium/calcium electrolyte, contained no calcium within the detection limits of EDX. Thus, the dendrite blocking mechanism appears to occur via an adsorption mechanism, rather than by co-deposition. Close inspection of the deposit shows a roughened substrate with fibrous material between the dimpled spheres. This could be decomposed electrolyte, which results in the lower efficiency.

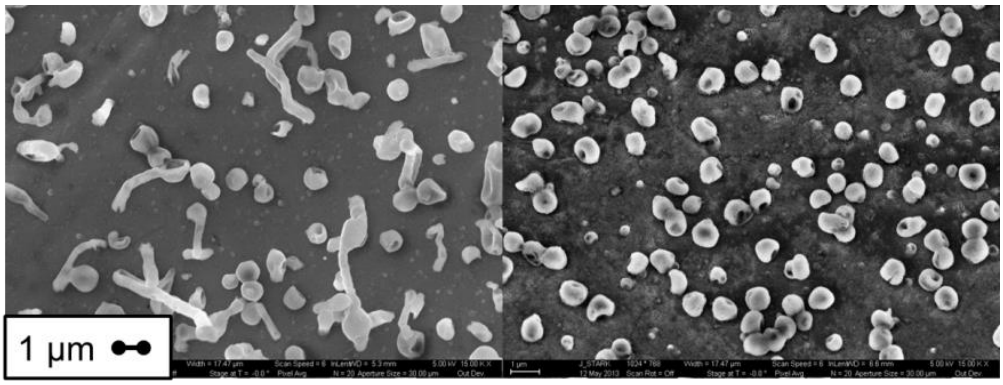

Figure 7.8: Lithium deposited at -0.3 V for 500 s from a (left) 1 M Li^{+}/0.05 M Ca^{2+} electrolyte and (right) 1 M Li^{+}/0.1 M Ca^{2+} electrolyte.

The addition of 0.1 M Sr^{2+} or Ba^{2+} to the IL electrolyte showed similar behavior to that of Ca^{2+}. Based on the CV in Figure 7.6, the coulombic efficiency was 43% for the strontium and 65% for the barium containing electrolyte. Current densities were lower for these two electrolytes compared to the lithium-only electrolyte. The deposits produced

from the lithium/strontium and lithium/barium electrolytes (i.e. 0.05 M and 0.1 M concentrations of Sr^{2+} or Ba^{2+} in addition to 1 M Li^{+}) were examined. The images, Figure 7.9, show the deposit morphology for the four cases. At 0.05 M, a significant change in the deposit morphology was observed compared to the lithium-only deposit in Figure 7.1 for both foreign ions. The effect of Ba^{2+} and Sr^{2+} on the deposit was similar to the effect of Ca^{2+} ions. Most of the deposit was composed of dimpled spheres with some dendrites. When the concentration was increased to 0.1 M, nearly all deposited material was in the form of dimpled spheres. Only an occasional dendrite was observed. The same fibrous material was observed on the deposit from the lithium/calcium electrolyte was observed on the deposit from the lithium/strontium or lithium/barium electrolytes, although to a lesser degree. EDX analysis did not show any trace of strontium or barium in the sample, suggesting that like the calcium and magnesium cases, dendrite suppression occurred at the electrode/electrolyte interface rather than by significant co-deposition.

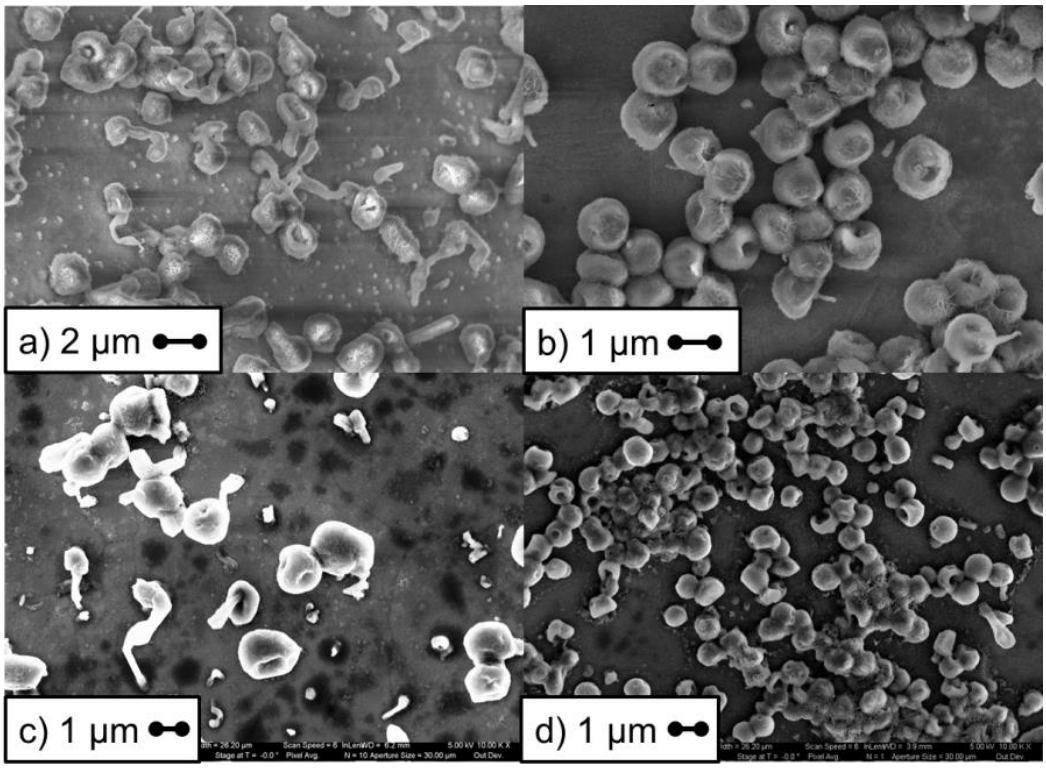

Figure 7.9: Deposits from electrolytes held at -0.3 V for 500 s. a) 1 M Li^+/0.05 M Sr^{2+}, b) 1 M Li^+/0.1 M Sr^{2+}, c) 1 M Li^+/0.05 M Ba^{2+}, d) 1 M Li^+/0.05 M Ba^{2+}.

The doubly charged alkaline earth ions behaved differently from the singly charged alkali ions. It is noted that the electrical double layer (EDL) in an ionic liquid differs from that of an organic electrolyte because the charge density is significantly higher, resulting in a multilayered structure. In conventional solutions, salts are dissolved through the formation of a neutral solvent shell around the ions. Compact and diffuse layers form in the presence of a charged surface to balance that charge. Models for the double layer in aqueous systems are based around dilute solutions but ionic liquids do not follow these assumptions[105,106]. Molecular dynamic simulations have shown that distinct anion and cation layers form at the electrical interface of an IL and a charged surface[107]. The first layer consists of the large N_{1114}^+, Li^+, and double charged alkaline earth cations. Next distinct layer will consist of $TFSI^-$, the only anion in the system. Ionic liquid double layers

consist of multiple alternating ion layers, making the charge distribution near the surface more complex [108]. Because the doubly charged alkaline earth cations are each associated with two $TFSI^-$ anions, this layer will be bulkier than in an electrolyte without the additional anions. This could hinder lithium transport to the surface during plating, essentially negating the preferential growth on possible dendritic sites.

7.3 Summary

The addition of Group 1 alkali metals to a lithium electrolyte produced a variety of results depending on the metal ion added to the electrolyte. Sodium ions showed the most promising behavior for the reduction/oxidization from the N_{1114}-TFSI ionic liquid. Adding Na-TFSI to the electrolyte in small concentrations resulted in a dimpled-sphere shaped deposit due to the co-deposition of sodium and lithium metal. Potassium ions were not reduced on stainless steel and their addition to the lithium ion containing electrolyte yielded a flake-like deposit, however dendrites still occurred. Rubidium and cesium ions were reduced starting at -0.11 V and -0.22 V vs. Li/Li^+, respectively. Ding et. al proposed a mechanism whereby a foreign ion that would deposit 0.05-0.1 V negative of lithium prevents dendrites, as they showed with cesium ions. The same effects were not observed in this ionic liquid electrolyte, regardless of potential applied or concentration used. A co-deposit similar to the lithium/sodium electrolyte was not achieved due to electrolyte decomposition. A non-dendritic co-deposit may still possible with cesium or rubidium if a more stable ionic liquid were found and the concentration of cesium or rubidium ions was increased.

The addition of small amounts of Group 2 alkaline earth ions had a dramatic effect on the lithium metal deposit morphology. All alkaline earth metals prevented dendritic

growth; however, they also lowered the current density associated with lithium deposition and re-oxidation. Magnesium ions suppressed the reduction of lithium ions even at low concentrations. The current density for the lithium redox reactions and the coulombic efficiency associated with them increased with higher molecular weight. The addition of Ba^{2+} was most successful in giving the highest current density and reversibility while maintaining a non-dendritic deposit. A concentration-dependent dendrite suppression effect was observed with calcium, strontium, and barium that gave a similar dimpled-sphere morphology to the lithium/sodium electrolyte. However, no second-metal appears to have been deposited, nor did these metals deposit from the electrolyte in the absence of lithium ions. Instead, the dendrite suppression appears to have occurred as a result of surface effects (i.e. blockage) and lithium ion transport inhibition. It is possible that alkaline earth metal ions adsorb on the surface limiting the rate at which lithium can be deposited (supported by lower current density) and thus limiting the fast growth that would lead to dendrites in lithium-only systems.

8. Implications and Future Work

8.1 Mechanism of Dendrite Suppression using Alkaline Earth Metal Ions

The addition of sodium ions to a lithium electrolyte resulted in the non-dendritic co-deposition of the two metals. A SIMS ion image revealed that the sodium was localized rather than dispersed evenly, indicating a physical blocking of dendritic sites. When alkaline earth metals ions are added to a lithium electrolyte the resulting sphere-like deposit is similar to the lithium/sodium deposit in appearance but no alkaline earth metals were found in the deposit. The mechanism for dendrite suppression with alkaline earth metal ions is thus different from sodium's physical blocking.

A possible explanation for the change in morphology without co-deposition is an adsorption of the alkaline earth metal ions. This could be investigated by electrochemical impedance spectroscopy (EIS). EIS can be used to characterize the double layer at the electrode/electrolyte interface of a symmetric cell with the desired electrolyte. The simplest equivalent circuit for such a cell is Randles equivalent circuit shown in Figure 8.1[68]. The circuit includes the electrolyte resistance (R_Ω), the charge transfer resistance (R_{ct}), double layer capacitance (C_d), and Warburg impedance (Z_w). If an adsorption is present, the double layer capacitance will be affected. This capacitance can be calculated from the imaginary component of the impedance, as shown in Equation 8.1. The capacitance of the double layer can then be further broken down into the dielectric constant e, area A, and thickness d.

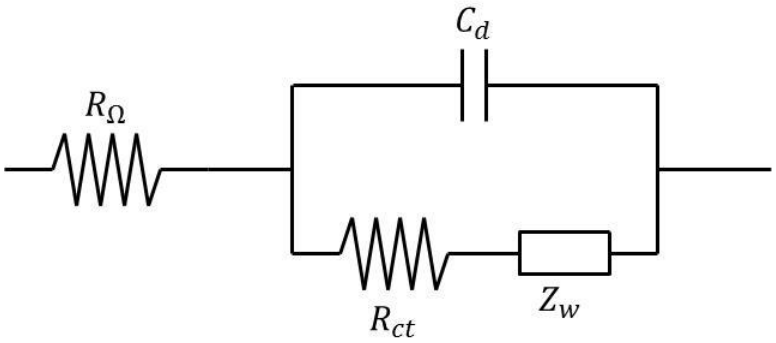

Figure 8.1: Randles equivalent circuit could be used as a basis for analyzing the electrode electrolyte interface. R_Ω is the electrolyte resistance, R_{ct} is the charge transfer resistance, C_d is the double layer capacitance, and Z_w is the Warburg impedance.

$$C_d = {}^{\varepsilon A}/_{d} \tag{8.1}$$

Based on the changes in C_d, conclusions can be drawn about the effect of the alkaline earth metal ions on the electrical double layer at the anode. A lower C_d indicates a thicker double layer that could be caused by the increased charge density of the ions. The charge transfer resistance, R_{ct}, may also be affected by the alkaline earth metal ions. This parameter characterizes the kinetics of lithium reduction at the surface. The addition of foreign metal ions could sufficiently slow the lithium reduction and negate the accelerated plating at dendrite tips. A more detailed analysis can be conducted by testing the insertion of an adsorbed layer capacitance in parallel with the charge transfer resistance and Warburg impedance in equivalent circuit[68].

8.2 Overcharge Protection for Insertion Anodes

Graphite and silicon anodes both operate just positive of the lithium reduction potential. The potential of these anodes must thus be very closely controlled to prevent lithium deposition from occurring on the surface. Lithium dendrite formation has been observed in situ when these anodes are overcharged[32,33]. In operation, such abuse leads to a short circuit and thermal runaway that present a safety concern. The results obtained in this thesis could mitigate the formation of destructive lithium dendrite growth in the case of overcharge. A small amount of Na^+, Ca^{2+}, Sr^{2+}, or Ba^{2+} could be added to the existing lithium electrolyte in a graphite battery. Upon overcharge, lithium would deposit as a harmless granular deposit rather than dendrites. These granules could even be re-oxidized preserving some of the active material.

The N_{1114}-TFSI ionic liquid does not allow for stable cycling with graphite anodes. Without any additives, a capacity of ~20 mAh/g can be achieved, far from the theoretical capacity[54]. The exact reason for this is unclear, but intercalation of the quaternary ammonium cation has been suggested as a possible cause. Adding an SEI former, such as EC, prevents this intercalation and is shown to give good cycling capacity[54]. A similar pyrrolidinium TFSI ionic liquid showed good compatibility with graphite at elevated temperatures without such additives and would also be a candidate for further study with the proposed overcharge mechanism. The higher temperature required does make this potential battery less practical[109]. Finally, ionic liquids with the FSI^- anion, rather than $TFSI^-$, have shown stable graphite cycling without additives[57,58]. These ionic liquids have a lower viscosity due to the smaller anion, but are paired with many of the same cations. This is thought to be due to a different arrangement in the double layer and better SEI formation. Since these methods of achieving stable graphite cycling preserve the nature of the IL that is the basis for our experiments, it is possible that one of these approaches

would maintain the ability to deposit non-dendritic lithium. The lithium deposit morphology would have to be evaluated from the altered electrolytes to confirm that the foreign metal ions have a similar effect in these ionic liquids as in our test case.

A second option to utilize this finding in a graphite battery is to perform similar experiments in an organic electrolyte, such as EC/DMC. Sodium salts (Na-TFSI and $NaPF_6$) and potassium salts (K-TFSI and KPF_6) were already tested with lithium in EC/DMC and did not yield a non-dendritic deposit. Sodium does not electrodeposit from organic electrolytes, so the co-deposition mechanism seen in ionic liquids is not possible in organic electrolyte. No work has been done however on the alkaline earth metals in conjunction with lithium. The doubly charged alkaline earth ions will behave quite differently than singly charged ions, making this a worthy topic to explore.

8.3 The Future of Lithium Metal Batteries

Morphology is the foremost concern in lithium metal batteries because dendrites can cause the catastrophic failure of the battery. Additionally, dendrites are thought to sometimes break off or oxidize at the base before the tip, isolating the lithium active material. The high surface area of dendritic growth leads to large amounts of SEI formation leading to lost charge and inefficiencies in the battery. The elimination of these dendrites should thus lead to higher efficiencies. The morphology of lithium metal has been addressed in this work by the addition of selected foreign metal ions, but even though non-dendritic deposits were achieved by several methods, these did not lead to higher coulombic efficiencies. In the chloroaluminate case, lithium alone had a coulombic efficiency of 90% while the non-dendritic lithium/sodium co-deposit only showed 87%. For N_{1114}-TFSI, the coulombic efficiency was 70% for the lithium-only

case, and the same for the non-dendritic lithium/sodium co-deposit (chapter 3). When testing alkaline earth metals, non-dendritic deposits from lithium/calcium and lithium/strontium electrolytes had lower efficiencies than lithium-only. The non-dendritic lithium/barium electrolyte maintained the same coulombic efficiency as lithium-only electrolyte, but did not exceed it.

The lack of increase in coulombic efficiency shows that dendrites themselves are not the main cause of inefficiency. Loss of contact and oxidation at the base do not seem to occur readily, even in beaker cells where no additional force (such as a separator in a coin cell) serves to keep lithium on the substrate. The main driver for coulombic efficiency is the electrolyte and additives used. The common battery solvents, such as EC/DMC, also cannot achieve the coulombic efficiency required for a battery. Thus, the next step in developing the lithium metal anode is to look at a broader range of solvents that could be used as a basis of the electrolyte. Ethereal solvents could be successful considering some work has already been done using tetrahydrofuran (THF) and dioxolane. These have shown good stability with lithium metal, though have so far failed at high charging rates. Aromatic compounds such as toluene have also shown good stability with lithium metal [5,40,110,111].

In ionic liquids, it is the organic cation that is generally reduced at the negative potentials required for lithium reduction. By eliminating this organic component, the stability of the electrolyte could be increased. One way to do this is to use a mixture of the salt only that has a moderate melting point. While pure $TFSI^-$ salts melt at 450-500 K (178-228°C), mixtures of Cs-, K-, Na-, and Li-TFSI salts can melt at 388 K (116 °C)[112,113]. If $TFSI^-$ is replaced with FSI^-, salt mixtures can melt around 330 K (48 °C)[114]. Eutectics of alkali-TFSI and alkali-FSI salts look unlikely to be liquid at room temperature but alkaline earth salts have not been investigated. In this work we showed that these salts have a

positive effect on the lithium morphology. In addition, the bulkier differently charged M^{2+}-$TFSI_2$ salts could disrupt the structure of the final mixture enough to lower the melting point to below room temperature. Alternate anions such as triflate ($CF_3SO_3^-$) or methanesulfonate ($CH_3SO_3^-$) as the anion could also be explored. The lithium triflate salt has been used in previous lithium electrolytes and seems stable, though extensive cycling has not been completed[115,116]. Triflate has not been used as the anion of an ionic liquid electrolyte in lithium batteries. In existing ionic liquids, asymmetric character in the cation leads to lower melting points and viscosity, thus new asymmetric anions might also lower the melting points of these salt mixtures.

8.4 Fundamental Study of Lithium Dendrite Growth

Why does lithium deposit dendritically and other alkali metals do not? This question was no answered directly by this work though parallels to other dendritic systems lead to some conclusions about the role of crystallinity and varying growth rates in dendrites. While many empirical studies have observed lithium electrodeposits and the result of additives or configuration changes, fundamental studies of the processes at work are still lacking.

An ex situ on the crystallinity of dendritic lithium was attempted, but results were not conclusive. Dendrites were grown from electrolytes, collected, washed, and scanned using X-ray diffraction (XRD) in an attempt to determine crystallinity, however weak signals and insufficient material precluded conclusive results. Dendrites were also prepared for transmission electron microscopy (TEM) both by drop casting and growing directly on the grid, but both methods failed to produce results, in part because transfer to the instrument could not be done under an inert atmosphere and the material oxidized

before observation. Lithium has a low melting point at 180°C and the metal is soft at room temperature. This resulted in melting under the TEM beam further complicating analysis. In addition lithium almost certainly undergoes plastic deformation and recrystallization when prepared by ex situ methods.

It is hypothesized that lithium dendrites are single crystals and form because of preferred growth on a specific crystal face. In situ studies of micro batteries by Liu et. al and Ghassemi et al. have shown that lithium dendrites are single crystal. Liu et al. charged tin oxide and silicon nanowires in situ and observed lithium dendrites growing from the tips of the wires[32]. The dendrites were determined to be single crystal body-centered cubic with an amorphous layer of LiF. Ghassemi et al. also used silicon nanowires to observe the nucleation of lithium islands and subsequent growth of dendrite[33]s. Darker areas were observed at kinks in the fibers, potentially indicating a crystal mismatch. While these two studies agree on the crystallinity of dendrites, the effect of this crystallinity on dendrite growth was not identified.

Further in situ study of lithium dendrite crystallinity could lead to an explanation for dendrite growth. Such in situ TEM experiments should seek to identify the crystallographic growth direction of dendrites and compare this among multiple fibers. The previous two in situ experiments were conducted by overcharging insertion anodes, but conducting experiments on a simple substrate is preferable for observing nucleation behavior. A cryogenic stage may be necessary to prevent the melting of lithium as a high resolution TEM study will likely melt the lithium being studied.

8.5 Recommendations for Future Work

Recommendations for future work are outlined below.

1. Electrochemical impedance spectroscopy (EIS) study of lithium/alkaline earth electrolytes to determine specific adsorption behavior and effect of these additives of the conductivity and transport behavior of lithium ions.
2. Compatibility study between ionic liquid electrolytes and traditional insertion anodes (graphite) and cathodes (cobalt oxide, manganese oxide, iron phosphate), including organic SEI forming additives and alternative anions and cations for the ionic liquid.
3. A survey of alternative ionic liquid electrolytes that eliminate the organic cation, and instead are comprised of a low melting mixture of alkali and alkaline earth salts.
4. An in situ TEM study to observe the formation of lithium dendrites to look for a pattern in growth direction with regard to crystal orientation.

APPENDIX A: Calculation of the Specific Capacity

The specific capacity is a number used to compare the storage capacity of individual anode and cathode materials. In the case of lithium batteries, the number is calculated based on the molar ratio between the anode and lithium when the anode is charged, ex. LiC_6 and $SiLi_{4.4}$. A higher capacity indicates that more lithium can be stored in a given amount of material, thus higher capacity desired to enable lighter batteries. The commonly cited values are 372 mAh/g for graphite, 4200 mAh/g for silicon, and 3861 mAh/g for lithium. Notice that the capacity for lithium appears lower than that of silicon, meaning silicon would be the better anode; however, the lithium anode eliminates all supporting structures, thus it should achieve the best capacity. To examine this, the specific capacity calculations are shown below in detail.

Carbon

$$1g\ Carbon \cdot \frac{1\ mol\ C}{12.011\ g\ C} \cdot \frac{1\ mol\ Li}{6\ mol\ C} \cdot \frac{1\ mol\ e-}{1\ mol\ Li} \cdot \frac{96485\ A{\cdot}s}{1\ mol\ e-} \cdot \frac{1000\ mA}{1\ A} \cdot \frac{1\ h}{3600\ s} = 372\ mAh/g$$

Silicon

$$1g\ Silicon \cdot \frac{1\ mol\ Si}{28.086\ g\ Si} \cdot \frac{4.4\ mol\ Li}{1\ mol\ Si} \cdot \frac{1\ mol\ e-}{1\ mol\ Li} \cdot \frac{96485\ A{\cdot}s}{1\ mol\ e-} \cdot \frac{1000\ mA}{1\ A} \cdot \frac{1\ h}{3600\ s} = 4199\ mAh/g$$

Lithium

$$1g\ Lithium \cdot \frac{1\ mol\ Li}{6.941\ g\ Li} \cdot \frac{1\ mol\ Li}{1\ mol\ Li} \cdot \frac{1\ mol\ e-}{1\ mol\ Li} \cdot \frac{96485\ A{\cdot}s}{1\ mol\ e-} \cdot \frac{1000\ mA}{1\ A} \cdot \frac{1\ h}{3600\ s} = 3861\ mAh/g$$

The conflict arises because the capacities for carbon and silicon are based on the weight of the discharged anode, but the same calculation for lithium is based on the charged anode (pure Li), thus the cited capacity for lithium cannot be compared with the other two. Considering that lithium can theoretically be plated infinitely thick on a given

substrate, the comparable capacity calculation based on the discharged anode would result in ∞ mAh/g. This is not very useful when numerically comparing specific capacities.

Alternatively, one can calculate the capacity per g of the charged anode, which is the basis used for the capacity of the lithium metal anode.

Carbon

1g lithiated carbon contains 1 mol Li for every 6 mol C, effectively 81.476 g/mol

$$1g\ C_6Li \cdot \frac{1\ mol\ C_6Li}{81.476\ g\ C_6Li} \cdot \frac{1\ mol\ Li}{1\ mol\ C_6Li} \cdot \frac{1\ mol\ e-}{1\ mol\ Li} \cdot \frac{96485\ A{\cdot}s}{1\ mol\ e-} \cdot \frac{1000\ mA}{1\ A} \cdot \frac{1\ h}{3600\ s} = 329\ mAh/g$$

Silicon

1g lithiated silicon contains 4.4 mol Li for every 1 mol Si, effectively 58.626 g/mol

$$1g\ SiLi_{4.4} \cdot \frac{1\ mol\ SiLi_{4.4}}{58.626\ g\ SiLi_{4.4}} \cdot \frac{4.4\ mol\ Li}{1\ mol\ SiLi_{4.4}} \cdot \frac{1\ mol\ e-}{1\ mol\ Li} \cdot \frac{96485\ A{\cdot}s}{1\ mol\ e-} \cdot \frac{1000\ mA}{1\ A} \cdot \frac{1\ h}{3600\ s} = 2011\ mAh/g$$

These capacities are directly comparable to the commonly cited capacity of lithium, 3861 mAh/g.

APPENDIX B: Derivation of Geometry based Current-time Model

Depending on the growth geometry, which determines the active area for deposition, a different current-time relationship can be derived. The possible growth geometries are shown in Figure B.1. In the case of one-dimensional growth (Figure B.1a), the active are does not change with time, so the current resulting from the growth of a single nucleus is a potential-dependent constant. In the case of two-dimensional growth (Figure B.1b), a single nuclei growing outward over the substrate, the radius grows linearly with time. Lastly, the case of three-dimensional growth (Figure B.1c), a single atom growing outward in all directions, results in a quadratic relationship between area and time. These relationships are shown as Equations B.1a, B.1b, and B.1c respectively.

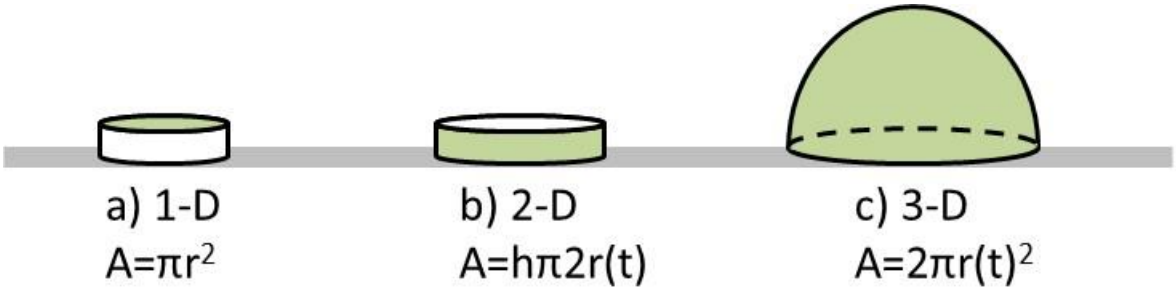

Figure B.1: Illustration of possible growth geometries with the active area for deposition highlighted in green. Note that the radius, *r*, is a constant in the 1-D case but a variable with respect to time in the other two cases.

$$i = E_1 \qquad i = E_2 t \qquad i = E_3 t^2 \qquad \text{(B.1a,b,c)}$$

In this work 1-D and 3-D growth were observed. A potential dependent rate, *k*, was defined in mol/(cm^{2}s) and the constants E_1 and E_3 are defined in Equ. B.2 where *M* is

the molecular weight in g/mol, ρ is the density in g/cm^3, F is Faraday's constant, and n is the number of mole equivalents.

$$E_1 = \pi r^2 knF \qquad E_3 = 2\pi \left(\frac{M}{\rho}\right)^2 nFk^3 \tag{B.2}$$

Given a linear nucleation rate as introduced in chapter 6 (Equation 6.4) the following integral (Equation B.3) must be solved to obtain the current for simultaneous nucleation and growth where u is the time at which an individual nucleus is formed. The derivation for 3-D nuclei is shown below. The result is that the i α t^3.

$$i = \int_0^t \left[\frac{\partial N}{\partial t}\right]_{t=u} f_i(t-u)du \tag{B.3}$$

$$\left[\frac{\partial N}{\partial t}\right]_{t=u} = N_0 A$$

$$i = N_0 A E_3 \int_0^t (t-u)^2 du$$

$$i = N_0 A E_3 \cdot \frac{-(t-u)^3}{3}\Bigg|_0^t$$

$$i = N_0 A E_3 \cdot -\frac{(t-t)^3 - (t-0)^3}{3}$$

$$i = N_0 A E_3 \cdot \frac{t^3}{3}$$

$$i = \frac{N_0 A 2\pi M^2 nFk^3}{3\rho^2} t^3$$

The same method can be used to determine the current based on the one-dimensional case, which corresponds to dendritic growth. The result is shown in Equation B.4, where i α t.

$$i = \int_0^t \left[\frac{\partial N}{\partial t}\right]_{t=u} f_i(t-u)du \tag{B.4}$$

$$\left[\frac{\partial N}{\partial t}\right]_{t=u} = N_0 A$$

$$i = N_0 A E_1 \int_0^t du$$

$$i = N_0 A E_1 t$$

$$i = N_0 A \pi r^2 k n F t$$

REFERENCES

1. Howard, H. P., Cheng, J., Vianco, P. T. & Li, J. C. M. Interface flow mechanism for tin whisker growth. *Acta Mater.* **59,** 1957–1963 (2011).

2. Lau, Y. K. A., Chernak, D. J., Bierman, M. J. & Jin, S. Formation of PbS Nanowire Pine Trees Driven by Screw Dislocations. 16461–16471 (2009).

3. Bierman, M. J., Lau, Y. K. A., Kvit, A. V, Schmitt, A. L. & Jin, S. Dislocation-driven nanowire growth and Eshelby twist. *Science* **320,** 1060–3 (2008).

4. Bort, H., Juttner, K., Lorenz, W. J., Staikov, G. & Budevski, E. Underpotential-Overpotential Transition Phenomena in Metal Deposition Processes. *Electrochim. Acta* **28,** 985–991 (1983).

5. Tarascon, J.-M. & Armand, M. Issues and challenges facing rechargeable lithium batteries. *Nature* **414,** 359–367 (2001).

6. Whittingham, M. S. Lithium batteries and cathode materials. *Chem. Rev.* **104,** 4271–301 (2004).

7. Marom, R., Amalraj, S. F., Leifer, N., Jacob, D. & Aurbach, D. A review of advanced and practical lithium battery materials. *J. Mater. Chem.* **21,** 9938 (2011).

8. Zhang, W.-J. A review of the electrochemical performance of alloy anodes for lithium-ion batteries. *J. Power Sources* **196,** 13–24 (2011).

9. Marom, R., Amalraj, S. F., Leifer, N., Jacob, D. & Aurbach, D. A review of advanced and practical lithium battery materials. *J. Mater. Chem.* **21,** 9938 (2011).

10. Scrosati, B. & Garche, J. Lithium batteries: Status, prospects and future. *J. Power Sources* **195,** 2419–2430 (2010).

11. Aurbach, D. *et al.* A short review on the comparison between Li battery systems and rechargeable magnesium battery technology. *J. Power Sources* **97-98,** 28–32 (2001).

12. Aurbach, D., Markovsky, B., Shechter, A. & Gan, R. A Comparative Study of Synthetic Graphite and Li Electrodes in Electrolyte Solutions Based on Ethylene Carbonate-Dimethyl Carbonate Mixtures. *J. Electrochem. Soc.* **143,** 3809–3820 (1996).

13. Choi, S. H., Son, J.-W., Yoon, Y. S. & Kim, J. Particle size effects on temperature-dependent performance of LiCoO2 in lithium batteries. *J. Power Sources* **158,** 1419–1424 (2006).

14. Ammundsen, B. & Paulsen, J. Novel Lithium-Ion Cathode Materials Based on Layered Manganese Oxides. *Adv. Mater.* **13,** 943–956 (2001).

15. Aurbach, D., Markovsky, B., Weissman, I., Levi, E. & Ein-Eli, Y. On the correlation between surface chemistry and performance of graphite negative electrodes for Li ion batteries. *Electrochim. Acta* **45,** 67–86 (1999).

16. Kanamura, K., Tamura, H., Shiraishi, S. & Takehara, Z. XPS Analysis of Lithium Surfaces Following Immersion in Various Solvents Containing LiBF4. **142,** 340–347 (1995).

17. Aurbach, D. Identification of Surface Films Formed on Lithium Surfaces in γ-Butyrolactone Solutions-II. Contaminated Solutions. *J. Electrochem. Soc.* **136,** 1611 (1989).

18. Zhuang, G. V, Xu, K., Yang, H., Jow, T. R. & Ross, P. N. Lithium ethylene dicarbonate identified as the primary product of chemical and electrochemical reduction of EC in 1.2 M LiPF6/EC:EMC electrolyte. *J. Phys. Chem. B* **109,** 17567–73 (2005).

19. Wang, X. J., Lee, H. S., Li, H., Yang, X. Q. & Huang, X. J. The effects of substituting groups in cyclic carbonates for stable SEI formation on graphite anode of lithium batteries. *Electrochem. commun.* **12,** 386–389 (2010).

20. Aurbach, D. *et al.* Recent studies on the correlation between surface chemistry, morphology, three-dimensional structures and performance of Li and Li-C intercalation anodes in several important electrolyte systems. *J. Power Sources* **68,** 91–98 (1997).

21. Aurbach, D., Zinigrad, E., Cohen, Y. & Teller, H. A short review of failure mechanisms of lithium metal and lithiated graphite anodes in liquid electrolyte solutions. *Solid State Ionics* **148,** 405–416 (2002).

22. Leung, K. Two-electron reduction of ethylene carbonate: a quantum chemistry re-examination of mechanisms. *Arxiv* 1–25 (2013).

23. Ota, H., Sakata, Y., Inoue, A. & Yamaguchi, S. Analysis of Vinylene Carbonate Derived SEI Layers on Graphite Anode. *J. Electrochem. Soc.* **151,** A1659 (2004).

24. Aurbach, D. *et al.* On the use of vinylene carbonate (VC) as an additive to electrolyte solutions for Li-ion batteries. *Electrochim. Acta* **47,** 1423–1439 (2002).

25. Ota, H. *et al.* Structural and Functional Analysis of Surface Film on Li Anode in Vinylene Carbonate-Containing Electrolyte. *J. Electrochem. Soc.* **151,** A1778–A1788 (2004).

26. Brissot, C., Rosso, M., Chazalviel, J.-N. & Lascaud, S. Dendrite growth mechanism in lithiu/polymer cells. *J. Power Sources* **81,** 925–929 (1999).

27. Nishikawa, K. *et al.* In Situ Observation of Dendrite Growth of Electrodeposited Li Metal. *J. Electrochem. Soc.* **157,** A1212–A1217 (2010).

28. Sagane, F., Shimokawa, R., Sano, H., Sakaebe, H. & Iriyama, Y. In-situ scanning electron microscopy observations of Li plating and stripping reactions at the lithium phosphorus oxynitride glass electrolyte/Cu interface. *J. Power Sources* **225,** 245–250 (2013).

29. Brissot, C., Rosso, M., Chazalviel, J.-N., Baudry, P. & Lascaud, S. In situ study of dendritic growth inlithium/PEO-salt/lithium cells. *Electrochim. Acta* **43,** 1569–1574 (1998).

30. Stark, J. K., Ding, Y. & Kohl, P. A. Nucleation of Electrodeposited Lithium Metal: Dendritic Growth and the Effect of Co-deposited Sodium. *J. Electrochem. Soc.* **160,** D337–D342 (2013).

31. Nishikawa, K., Mori, T., Nishida, T., Fukunaka, Y. & Rosso, M. Li dendrite growth and Li+ ionic mass transfer phenomenon. *J. Electroanal. Chem.* **661,** 84–89 (2011).

32. Liu, X. H. *et al.* Lithium fiber growth on the anode in a nanowire lithium ion battery during charging. *Appl. Phys. Lett.* **98,** 183107 (2011).

33. Ghassemi, H., Au, M., Chen, N., Heiden, P. a. & Yassar, R. S. Real-time observation of lithium fibers growth inside a nanoscale lithium-ion battery. *Appl. Phys. Lett.* **99,** 123113 (2011).

34. Yamaki, J., Tobishima, S., Hayashi, K., Nemoto, Y. & Arakawa, M. A consideration of the morphology of electrochemically deposited lithium in an organic electrolyte. *J. Power Sources* **74,** 219–227 (1998).

35. Crowther, O. & West, A. C. Effect of Electrolyte Composition on Lithium Dendrite Growth. *J. Electrochem. Soc.* **155,** A806–A811 (2008).

36. Hirai, T., Yoshimatsu, I. & Yamaki, J. Influence of Electrolyte on Lithium Cycling Efficiency with Pressurized Electrode Stack. *J. Electrochem. Soc.* **141,** 611–614 (1994).

37. Ota, H., Wang, X. & Yasukawa, E. Characterization of Lithium Electrode in Lithium Imides/Ethylene Carbonate, and Cyclic Ether Electrolytes. *J. Electrochem. Soc.* **151,** A427–A436 (2004).

38. Kanamura, K., Shiraishi, S. & Takehara, Z. Electrochemical Deposition of Very Smooth Lithium Using Nonaqueous Electrolytes Containing HF. *J. Electrochem. Soc.* **143,** 2187–2197 (1996).

39. Shiraishi, S., Kanamura, K. & Takehara, Z. Influence of initial surface condition of lithium metal anodes on surface modification with HF. *J. Appl. Electrochem.* **29,** 869–881 (1999).

40. Aurbach, D. *et al.* Attempts to Improve the Behavior of Li Electrodes in Rechargeable Lithium Batteries. *J. Electrochem. Soc.* **149,** A1267 (2002).

41. Gofer, Y., Ben-Zion, M. & Aurbach, D. Solutions of LiAsF6 in 1,3-dioxolane for secondary lithium batteries. *J. Power Sources* **39,** 163–178 (1992).

42. Ding, F. *et al.* Dendrite-Free Lithium Deposition via Self-Healing Electrostatic Shield Mechanism. *J. Am. Chem. Soc.* (2013).

43. Oliveira, G. M. & Carlos, I. a. Silver–copper electrodeposition from ammonium hydroxide solution: influence of EDTA and HEDTA. *J. Appl. Electrochem.* **39,** 1217–1227 (2009).

44. Dittmar, W. & Kohler, A. Das dickenwachstum von kalium-whisker im gebiet der kritischen Uebersattigung. *J. Cryst. Growth* **2,** 271–278 (1968).

45. Dittmar, W. & Neuman, K. Wachstums- und Verdampfungsgeschwindigkeit von nadelfoermigen Kaliumkristalle. *Zeitschrift fuer Electrochem.* **64,** 297–305 (1960).

46. Dittmar, W. & Mennicke, S. Bestimmung des mittleren Diffusionsweges adsorbierter Kaliumatome. *Zeitschrift fuer Phys. Chemie* **71,** 255–263 (1970).

47. Dittmar, W. & Neuman, K. Ueber die Gestalt und das Wachstum nadelfoermiger Kaliumkristalle. *Zeitschrift fuer Electrochem.* **61,** 70–73 (1957).

48. Del Sesto, R. E. *et al.* Limited thermal stability of imidazolium and pyrrolidinium ionic liquids. *Thermochim. Acta* **491,** 118–120 (2009).

49. Lewandowski, A. & Świderska-Mocek, A. Ionic liquids as electrolytes for Li-ion batteries—An overview of electrochemical studies. *J. Power Sources* **194,** 601–609 (2009).

50. Nakagawa, H. *et al.* Application of nonflammable electrolyte with room temperature ionic liquids (RTILs) for lithium-ion cells. *J. Power Sources* **174,** 1021–1026 (2007).

51. Kim, K., Lang, C. M. & Kohl, P. a. Properties of Asymmetric Benzyl-Substituted Ammonium Ionic Liquids and Their Electrochemical Properties. *J. Electrochem. Soc.* **152,** E56 (2005).

52. Fung, Y. S. & Zhou, R. Q. Room temperature molten salt as medium for lithium battery. *J. Power Sources* **81-82,** 891–895 (1999).

53. Howlett, P. C., MacFarlane, D. R. & Hollenkamp, A. F. A sealed optical cell for the study of lithium-electrode|electrolyte interfaces. *J. Power Sources* **114,** 277–284 (2003).

54. Zheng, H., Jiang, K., Abe, T. & Ogumi, Z. Electrochemical intercalation of lithium into a natural graphite anode in quaternary ammonium-based ionic liquid electrolytes. *Carbon N. Y.* **44,** 203–210 (2006).

55. Nakagawa, H. *et al.* Application of nonflammable electrolyte with room temperature ionic liquids (RTILs) for lithium-ion cells. *J. Power Sources* **174,** 1021–1026 (2007).

56. Kim, H., Ding, Y. & Kohl, P. a. LiSICON – ionic liquid electrolyte for lithium ion battery. *J. Power Sources* **198,** 281–286 (2012).

57. Sugimoto, T. *et al.* Ionic liquid electrolyte systems based on bis(fluorosulfonyl)imide for lithium-ion batteries. *J. Power Sources* **189,** 802–805 (2009).

58. Yamagata, M. *et al.* Charge–discharge behavior of graphite negative electrodes in bis(fluorosulfonyl)imide-based ionic liquid and structural aspects of their electrode/electrolyte interfaces. *Electrochim. Acta* (2013).

59. Scordilis-kelley, C., Fuller, J. & Carlin, R. T. Alkali Metal Reduction Potentials Measured in Chloroaluminate Ambient-Temperature Molten Salts. *J. Electrochem. Soc.* **139,** 694–699 (1992).

60. Gray, G. E., Winnick, J. & Kohl, P. A. Plating and Stripping of Sodium from a Room Temperature 1-Methyl-3-propylimidazolium Chloride Melt. *J. Electrochem. Soc.* **143,** 3820–3824 (1996).

61. Fuller, J., Osteryoung, R. A., Carolina, N. & Carlin, R. T. Rechargeable Lithium and Sodium Anodes in Chloroaluminate Molten Salts Containing Thionyl Chloride. **142,** 3632–3636 (1995).

62. Wibowo, R., Aldous, L., Rogers, E. I., Jones, S. E. W. & Compton, R. G. A Study of the Na / Na + Redox Couple in Some Room Temperature Ionic Liquids. *J. Phys. Chem. C* **114,** 3618–3626 (2010).

63. Vega, J. a., Zhou, J. & Kohl, P. a. Electrochemical Comparison and Deposition of Lithium and Potassium from Phosphonium- and Ammonium-TFSI Ionic Liquids. *J. Electrochem. Soc.* **156,** A253–A259 (2009).

64. Balducci, A. *et al.* Ionic Liquid as Electrolyte in Lithium Batteries: In Situ FTIRS Studies on the Use of Electrolyte Additives. *ECS Trans.* **11,** 109–114 (2008).

65. Lang, C. M., Kim, K. & Kohl, P. a. Catalytic additives for the reversible reduction of sodium in chloroaluminate ionic liquids. *Electrochim. Acta* **51,** 3884–3889 (2006).

66. Scordilis-kelley, C. & Carlin, R. T. Lithium and Sodium Standard Reduction Potentials in Ambient-Temperature Chloroaluminate Molten Salts. *J. Electrochem. Soc.* **140,** 1606–1611 (1993).

67. Wibowo, R., Jones, S. E. W. & Compton, R. G. Investigating the Electrode Kinetics of the Li/Li + Couple in a Wide Range of Room Temperature Ionic Liquids at 298 K. *J. Chem. Eng. Data* **55,** 1374–1376 (2010).

68. Bard, A. J. & Faulkner, L. R. *Electrochemical Methods*. (John Wiley & Sons, Inc., 2001).

69. Egashira, M., Todo, H., Yoshimoto, N., Morita, M. & Yamaki, J.-I. Functionalized imidazolium ionic liquids as electrolyte components of lithium batteries. *J. Power Sources* **174,** 560–564 (2007).

70. Scordilis-kelley, C. & Carlin, R. T. Stability and Electrochemistry of Lithium in Room Temperature Chloroaluminate Molten Salts. *J. Electrochem. Soc.* **141,** 873–875 (1994).

71. Gray, G. E., Kohl, P. A. & Winnick, J. Stability of Sodium Electrodeposited from a Room Temperature Chloroaluminate Molten Salt. *J. Electrochem. Soc.* **142,** 3636–3642 (1995).

72. Kadokawa, J., Iwasaki, Y. & Tagaya, H. Ring-Opening Polymerization of Ethylene Carbonate Catalyzed with Ionic Liquids: Imidazolium Chloroaluminate and Chlorostannate Melts. *Macromol. Rapid Commun.* **23,** 757–760 (2002).

73. Stark, J. K., Ding, Y. & Kohl, P. A. Dendrite-Free Electrodeposition and Reoxidation of Lithium-Sodium Alloy for Metal-Anode Battery. *J. Electrochem. Soc.* **158,** A1100–A1105 (2011).

74. Morigaki, K. Analysis of the interface between lithium and organic electrolyte solution. *J. Power Sources* **104,** 13–23 (2002).

75. Momma, T., Nara, H., Yamagami, S., Tatsumi, C. & Osaka, T. Effect of the atmosphere on chemical composition and electrochemical properties of solid electrolyte interface on electrodeposited Li metal. *J. Power Sources* **196,** 6483–6487 (2011).

76. Xu, K. *et al.* Syntheses and characterization of lithium alkyl mono- and dicarbonates as components of surface films in Li-ion batteries. *J. Phys. Chem. B* **110,** 7708–7719 (2006).

77. Kim, G.-T. *et al.* Development of ionic liquid-based lithium battery prototypes. *J. Power Sources* **199,** 239–246 (2012).

78. Younesi, R., Hahlin, M., Roberts, M. & Edström, K. The SEI layer formed on lithium metal in the presence of oxygen: A seldom considered component in the development of the Li–O2 battery. *J. Power Sources* **225,** 40–45 (2013).

79. Aurbach, D., Youngman, O. & Dan, P. The Electrochemical Behavior of 1,3-Dioxolane-LiClO4 Solutions-II. Contaminated Solutions. *Electrochim. Acta* **35,** 639–655 (1990).

80. Condemarin, R. & Scovazzo, P. Gas permeabilities, solubilities, diffusivities, and diffusivity correlations for ammonium-based room temperature ionic liquids with comparison to imidazolium and phosphonium RTIL data. *Chem. Eng. J.* **147,** 51–57 (2009).

81. Ramdin, M., Loos, T. W. De & Vlugt, T. J. H. State-of-the-Art of CO 2 Capture with Ionic Liquids. *Ind. Eng. Chem. Res.* **51,** 8149–8177 (2012).

82. Blath, J., Christ, M., Deubler, N., Hirth, T. & Schiestel, T. Gas solubilities in room temperature ionic liquids – Correlation between RTiL-molar mass and Henry's law constant. *Chem. Eng. J.* **172,** 167–176 (2011).

83. Anthony, J. L., Maginn, E. J. & Brennecke, J. F. Solubilities and Thermodynamic Properties of Gases in the Ionic Liquid 1-n-Butyl-3-methylimidazolium Hexafluorophosphate. *J. Phys. Chem. B* **106,** 7315–7320 (2002).

84. Anthony, J. L., Anderson, J. L., Maginn, E. J. & Brennecke, J. F. Anion effects on gas solubility in ionic liquids. *J. Phys. Chem. B* **109,** 6366–7634 (2005).

85. Gireaud, L., Grugeon, S., Laruelle, S., Yrieix, B. & Tarascon, J.-M. Lithium metal stripping/plating mechanisms studies: A metallurgical approach. *Electrochem. commun.* **8,** 1639–1649 (2006).

86. López, C. M., Vaughey, J. T. & Dees, D. W. Morphological Transitions on Lithium Metal Anodes. *J. Electrochem. Soc.* **156,** A726–A729 (2009).

87. Markowitz, M. & Boryta, D. Lithium Metal-Gas Reactions. *J. Chem. Egineering Data* **7,** 586–591 (1962).

88. Rhein, R. A. *Lithium Combustion : A Review*. 1–60 (1990).

89. Sharma, P. *et al.* Effects of anions on absorption capacity of carbon dioxide in acid functionalized ionic liquids. *Fuel Process. Technol.* **100,** 55–62 (2012).

90. Shi, W. & Maginn, E. J. Atomistic simulation of the absorption of carbon dioxide and water in the ionic liquid 1-n-Hexyl-3-methylimidazolium Bis(trifluoromethylsulfonyl)imide ([hmim][Tf2N]. *J. Phys. Chem. B* **112,** 2045–2055 (2008).

91. Stark, J. K., Ding, Y. & Kohl, P. A. Dendrite-Free Electrodeposition and Reoxidation of Lithium-Sodium Alloy for Metal-Anode Battery. *J. Electrochem. Soc.* **158,** A1100–A1105 (2011).

92. Kim, I.-T., Egashira, M., Yoshimoto, N. & Morita, M. On the electric double-layer structure at carbon electrode/organic electrolyte solution interface analyzed by ac

impedance and electrochemical quartz-crystal microbalance responses. *Electrochim. Acta* **56,** 7319–7326 (2011).

93. Stark, J. K., Ding, Y. & Kohl, P. A. Role of Dissolved Gas in Ionic Liquid Electrolytes for Secondary Lithium Metal Batteries. *J. Phys. Chem. C* **117,** 4980–4985 (2013).

94. Wibowo, R., Aldous, L., Jones, S. E. W. & Compton, R. G. The electrode potentials of the Group I alkali metals in the ionic liquid N-butyl-N-methylpyrrolidinium bis(trifluoromethylsulfonyl)imide. *Chem. Phys. Lett.* **492,** 276–280 (2010).

95. Feng, Z., NuLi, Y., Wang, J. & Yang, J. Study of Key Factors Influencing Electrochemical Reversibility of Magnesium Deposition and Dissolution. *J. Electrochem. Soc.* **153,** C689 (2006).

96. Aurbach, D. *et al.* Electrolyte Solutions for Rechargeable Magnesium Batteries Based on Organomagnesium Chloroaluminate Complexes. *J. Electrochem. Soc.* **149,** A115 (2002).

97. Muldoon, J. *et al.* Electrolyte roadblocks to a magnesium rechargeable battery. *Energy Environ. Sci.* **5,** 5941 (2012).

98. NuLi, Y., Yang, J. & Wu, R. Reversible deposition and dissolution of magnesium from BMIMBF4 ionic liquid. *Electrochem. commun.* **7,** 1105–1110 (2005).

99. Shimamura, O., Yoshimoto, N., Matsumoto, M., Egashia, M. & Morita, M. Electrochemical co-deposition of magnesium with lithium from quaternary ammonium-based ionic liquid. *J. Power Sources* **196,** 1586–1588 (2011).

100. Joseph, S. & Kamath, P. V. Electrodeposition of Oriented SrCO[sub 3] Coatings on Stainless Steel Substrates. *J. Electrochem. Soc.* **153,** D99–D103 (2006).

101. Prasad, B. E. & Kamath, P. V. Electrodeposition of dicalcium phosphate dihydrate coatings on stainless steel substrates. *Bull. Mater. Sci.* **36,** 475–481 (2013).

102. Joseph, S., Upadhya, S. & Kamath, P. V. Electrodeposition of BaCO 3 coatings on stainless steel substrates : Oriented growth in the presence of complexing agents †. **121,** 685–691 (2009).

103. Katić, J., Metikoš-Huković, M. & Babić, R. Synthesis and characterization of calcium phosphate coatings on Nitinol. *J. Appl. Electrochem.* **In press,** (2013).

104. *Handbook of Battery Materials*. (Wiley-VCH, 1999).

105. Kornyshev, A. A. Double-layer in ionic liquids: paradigm change? *J. Phys. Chem. B* **111,** 5545–5557 (2007).

106. Fedorov, M. V. & Kornyshev, A. a. Towards understanding the structure and capacitance of electrical double layer in ionic liquids. *Electrochim. Acta* **53,** 6835–6840 (2008).

107. Kirchner, K., Kirchner, T., Ivaništšev, V. & Fedorov, M. V. Electrical double layer in ionic liquids: Structural transitions from multilayer to monolayer structure at the interface. *Electrochim. Acta* (2013). at <http://linkinghub.elsevier.com/retrieve/pii/S0013468613009547>

108. Bazant, M. Z., Storey, B. D. & Kornyshev, A. a. Double Layer in Ionic Liquids: Overscreening versus Crowding. *Phys. Rev. Lett.* **106,** 046102 (2011).

109. Nádherná, M., Reiter, J., Moškon, J. & Dominko, R. Lithium bis(fluorosulfonyl)imide–PYR14TFSI ionic liquid electrolyte compatible with graphite. *J. Power Sources* **196,** 7700–7706 (2011).

110. Aurbach, D., Zaban, A., Gofer, Y., Abramson, O. & Ben-Zion, M. Studies of Li Anodes in the Electrolyte System 2Me-THF / THF / Me-Furan / LiAsF6. *J. Am. Chem. Soc.* **142,** 687–696 (1995).

111. Krystian, M. & Pichl, W. Metallography of alkali metal single crystals. *Mater. Charact.* **46,** 1–9 (2001).

112. Kubota, K., Nohira, T., Goto, T. & Hagiwara, R. Ternary Phase Diagrams of Alkali Bis(trifluoromethylsulfonyl)amides. *J. Chem. Eng. Data* **53,** 2144–2147 (2008).

113. Watarai, A. *et al.* A rechargeable lithium metal battery operating at intermediate temperatures using molten alkali bis(trifluoromethylsulfonyl)amide mixture as an electrolyte. *J. Power Sources* **183,** 724–729 (2008).

114. Fukunaga, A. *et al.* Intermediate-temperature ionic liquid NaFSA-KFSA and its application to sodium secondary batteries. *J. Power Sources* **209,** 52–56 (2012).

115. Fahys, B., Akturk, N. & Herlem, M. Conductivity and stability towards lithium metal of lithium triflate (LiSO3CF3) and lithium bistrifluorosulfonylimide (Li(SO3CF3)2N) in amines and their mixtures with ammonia. *J. Power Sources* **43,** 349–353 (1993).

116. Fahys, B. & Herlem, M. Lithium nitrate and lithium trifluoromethanesulfonate ammoniates for electrolytes in lithium batteries. *J. Power Sources* **34,** 183–188 (1991).